
Beam shaping of Bessel beams with high power laser systems

DISSERTATION

zur Erlangung des akademischen Grades
doctor rerum naturalium (Dr. rer. nat.)

vorgelegt an der Physikalisch-Astronomischen Fakultät der
Friedrich-Schiller-Universität Jena

von M. Sc. Sebastian Merx
geboren am 4. Oktober 1992 in Erfurt

Erster Gutachter: Prof. Dr. Herbert Gross, Friedrich-Schiller-Universität Jena

Zweiter Gutachter: Prof. Dr. Marco Ornigotti, Tampere University

Dritter Gutachter: Prof. Dr. Alexander Szameit, Universität Rostock

Tag der Disputation: 13. Oktober 2021

Strahlformung von Bessel-Strahlen mit Hochleistungslasersystemen

Die stetige Entwicklung moderner optischer Technologien ermöglicht den Fortschritt in vielen Anwendungsbereichen. Hochleistungslasersysteme spielen dabei eine wichtige Rolle, wobei fortschreitend bessere Strahlqualitäten und höhere Lichtleistungen erzielt und neue Anwendungsfelder erschlossen werden. Hierbei nehmen Bessel-Strahlen durch ihre speziellen Eigenschaften eine besondere Rolle ein, da mit ihnen insbesondere eine Entkopplung von axialer und lateraler Auflösung möglich ist. Durch die erhöhten Anforderungen und die steigende Lichtleistungen ergeben sich neue Herausforderungen in der Konzeption, Simulation und Bewertung der geformten Laserstrahlung, sowie auch der Lasersysteme selbst. Ziel dieser Arbeit ist die Bearbeitung verschiedener Teilbereiche dieser komplexen Themengebiete. Natürlich kann im Rahmen dieser Dissertation nur eine Auswahl der vielfältigen Aspekte bearbeitet werden. Diese umfassen die Rekonstruktion und Bewertung von realen Laserstrahlen, die effiziente Berechnung von Bessel-Gauss Strahlen, die durch Wellenfrontfehler gestört werden und die konzeptionelle passive Athermalisierung von refraktiven Hochleistungslasersystemen.

In der Bewertung und Simulation von Laserstrahlen werden häufig Näherungen hinsichtlich Amplitude, Phase, Kohärenz und Polarisation gemacht. Die Qualität wird typischerweise mit dem M^2 -Wert spezifiziert, wobei dieser vergleichend zu einem idealen Gauss-Strahl definiert ist. Leider nimmt die Aussagekraft dieses Kriteriums aber bei Strahlen ab, die sich von der Gauss-Lösung stark unterscheiden. Die Ursache hierfür ist nicht mit dem M^2 -Wert identifizierbar. Besonders bei Strahlformung ist die Betrachtung des Eingangsfeldes wichtig, da hier fehlerbehaftete Eingangsfelder starken Einfluss auf die berechneten Zielfelder haben. Durch eine laserspezifische Lösung der "*transport of intensity equation*" konnten beide Problemstellungen gelöst und das Feld realer Laserstrahlen rekonstruiert werden. Dies ermöglicht die Separierung von Amplituden- und Phasenfehlern. Gleichzeitig kann das rekonstruierte Feld für Simulationen als reale Laserlichtquelle genutzt werden, um die Prognosesicherheit zu erhöhen.

Die effiziente Berechnung und Bewertung von Bessel-Gauss Strahlen ist ein aktuelles Thema in Wissenschaft und Industrie. Die Berechnung solcher Strahlen wird durch die konische Wellenfront und der daraus enorm vergrößerten Abstraten aufwändig.

Müssen nicht-rotationssymmetrische Wellenfrontfehler berücksichtigt werden, so wird der numerische Aufwand weiter gesteigert. Im Rahmen dieser Arbeit wird eine analytische Lösung für das axiale Feld eines Bessel-Gauss Strahls berechnet, der mittels sphärischen Aberrationen, Astigmatismus und Koma gestört werden kann. Dadurch kann die axiale Intensität effizient berechnet werden, sodass Störungen dieser bereits in der Design- und Toleranzierungsphase berücksichtigt werden können. Außerdem wurde das klassische Strehl-Verhältnis von einem Fokuspunkt auf eine Fokuslinie erweitert, um die besonderen Eigenschaften von Bessel-Strahlen wirksam abbilden zu können.

Im Zuge stetig steigender Laserleistungen muss die Leistungsabhängigkeit der optischen Güte von Strahlführungs- und Strahlformungssystemen immer stärker in den Fokus bei der Konzeption gelegt werden. Das heißt, dass die Systeme so ausgelegt werden müssen, dass sie über einen großen Leistungs- bzw. Temperaturbereich stabil arbeiten, also athermalisiert sind. Für Hochleistungslasersysteme ist dies besonders kritisch, da die Laserstrahlung selbst Wärme in die optischen Bauteile einbringt und diese folglich inhomogen erhitzt. Dies führt wiederum paraxial zu einer sich mit der Leistung bzw. Temperatur ändernden Brechkraft der Elemente. Das Hauptaugenmerk in diesem Teilbereich liegt darin, diese Effekte zu beschreiben, sodass ein Konzept zur passiven Athermalisierung von Hochleistungslasersystemen durch geeignete Parameterwahl erstellt werden kann. Weiterhin wird dieses Konzept beispielhaft an typischen optischen Systemen evaluiert und durch Simulation gestützt.

Insgesamt ist es im Rahmen dieser Dissertation gelungen, wesentliche Fortschritte in Teilbereichen bei der Simulation von Strahlformungen von Bessel-Strahlen mit Hochleistungslasersystemen zu erreichen. Hierbei konnten reale Laserstrahlen rekonstruiert und bewertet werden. Außerdem konnten die erarbeitete Methoden zur effizienten Berechnung und Bewertung von Bessel-Gauss Strahlen an einem Beispielsystem demonstriert werden. Die passive Athermalisierung von refraktiven Systemen mit hoher Laserleistung wurde konzeptionell vorgestellt und evaluiert. Die Wirksamkeit dieses Konzeptes wurde durch Simulationen bestätigt. Somit konnten im Rahmen dieser Arbeit sowohl die Bewertungs- und Simulationsmöglichkeiten von Lasersystemen deutlich verbessert werden, als auch die Nutzbarkeit von höheren Laserleistungen durch neue Konzeptionierungen ausgeweitet werden.

Contents

1. Introduction	5
2. Fundamentals	11
2.1. Wave equation	11
2.1.1. Plane waves	12
2.1.2. Spherical waves	14
2.1.3. Bessel beams	14
2.2. Paraxial wave equation	16
2.2.1. Gaussian beams	17
2.2.2. Transport of intensity equation	18
2.3. Light as rays	19
3. Modelling of beam profiling systems	21
3.1. Hybrid approach for optical systems	21
3.2. Performance metrics	24
3.2.1. Zernike-polynomials	25
3.2.2. Strehl-ratio	26
3.2.3. The beam propagation factor M^2	28
3.3. Profiling of quasi Bessel beams	31
3.3.1. Bessel-Gauss beam	32
3.3.2. Method of stationary phase	33
3.3.3. Profiling of the on-axis intensity	35
3.4. Homogeneous thermal load in optical systems	37
3.4.1. Heated thin lens singlet	38
3.4.2. Heated thin lens doublet	39

4. Coherent laser beam reconstruction and characterization by non-iterative phase retrieval solving the TIE	41
4.1. Solution of the TIE	43
4.1.1. Classical solution	43
4.1.2. Specific solution for laser beams	44
4.1.3. Critical parameters	46
4.2. Results and discussion	48
4.2.1. Estimated accuracy of the retrieved phase	48
4.2.2. Verification with experimental data	50
4.2.3. Discussion	56
5. Effective performance evaluation of perturbed Bessel-Gauss beams based on the analytical expression of the line focus	61
5.1. Full diffraction calculation of perturbed Bessel-Gauss beams	63
5.2. Analytical expression for the on-axis field of perturbed Bessel-Gauss beams	66
5.2.1. Derivation	66
5.2.2. Results and discussion	69
5.3. Sensitivity analysis of an example system by an extended Strehl-ratio definition	73
6. Passive athermalization of refractive optical systems for high power laser applications	77
6.1. Temperature inside a thin lens	79
6.2. Focal power of a heated lens	80
6.3. Material parameter ξ	85
6.4. Application	87
6.4.1. Athermalization of a doublet	88
6.4.2. Athermalization with two separated lenses	88
6.4.3. Athermalization with three separated lenses	90
6.5. Simulation of athermalized systems	92
6.5.1. Comparison of a singlet and an athermalized doublet	93
6.5.2. Comparison of athermalized two-lens telescopes	94
7. Conclusion and outlook	99
Bibliography	101

A. Appendix	111
A.1. Explicit formulation of Zernike-polynomials	111
A.2. Thermal properties of glasses	112
A.3. Thermal properties of mounting materials	116
B. Ehrenwörtliche Erklärung	117
C. Liste der wissenschaftlichen Veröffentlichungen und Vorträge	119
D. Danksagung	121

1. Introduction

The steady development of optical technologies enables the progress of modern technology in many ways. An example for this is lithography with its highest demands for accuracy to supply the world with computer chips. Another example is telecommunication with the corresponding fiber-optic networks to connect the world with the driving force of more miniaturization in order to transfer information at increased data rates. A further example is laser material processing, where laser light and short pulses are used as a tool. Here, the laser light is shaped specifically to the applicational demands while simultaneously the laser power can be increased with state-of-the-art laser systems.

High power laser systems are applied in a broad spectrum of fields such as the removal of space debris or for military intentions to defence missiles and drones [1, 2]. For space telecommunication, high power laser systems are developed to substitute conventional radio communication with the ever-present aim of increased data rates [3]. Furthermore, high power laser sources are necessary for the investigation of highly non-linear light-matter interactions and can even be used as a potential substitute of classical large-scale particle accelerators for medical cancer therapy [4–6]. For additive manufacturing technologies such as selective laser melting or selective laser sintering, high power laser sources are essential [7, 8]. Another application field is material processing, where holes can be drilled extremely accurate with proper shaped laser radiation, materials can be attached together by laser welding and surface properties can be modified by laser hardening [9–13].

While the application of such high power laser systems enables new possibilities and new markets, the capability to take this as an advantage is directly linked to the effective simulation, fabrication and assessment of those systems. Effective simulation involves appropriate physical modelling depth from the light source through the optical system to the target with the intended field distribution.

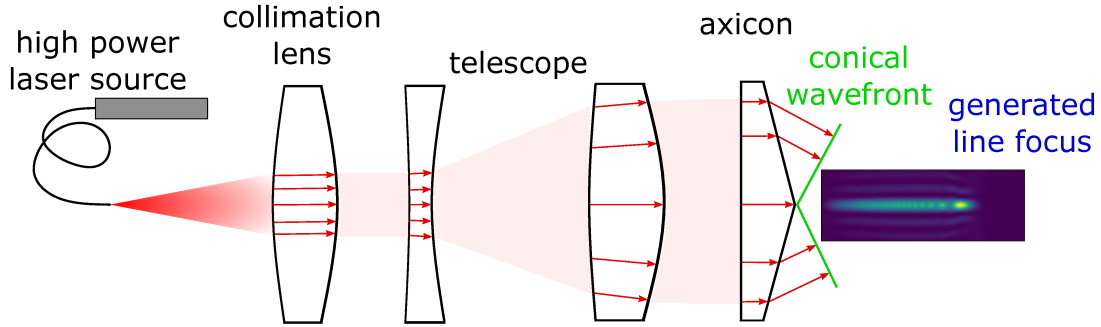


Figure 1.1.: Optical setup for generating a line focus consisting of a high power laser source, a collimator lens, a telescope to adapt the beam width and a subsequent axicon to generate the necessary conical wavefront.

In the context of this work, three crucial topics for the simulation of laser systems operating at high power to generate Bessel beams are addressed. To make the connection of these topics more vivid, an example system is shown in Fig. 1.1. Here, laser light from a high power source is collimated and the beam width is adapted by a subsequent telescope. The ideally plane wavefront of this beam is then transformed into conical shape by an axicon and a Bessel beam with the corresponding line focus is generated. Within this configuration, the key elements are the description of the laser light and how it is influenced by the lens components in terms of amplitude and phase. Furthermore, the performance of the generated Bessel beam must be assessed efficiently, so that it can be easily included in the modelling and design of such a system. Since the system is intended to operate at high power, it must be optically stabilized for induced temperature changes due to absorption effects in the lens materials. Thus, all three topics have to be linked for a design and a successful performance prediction of such system types.

The modelling of typical laser light sources typically comprises certain approximations regarding amplitude, phase, coherence and polarization. In common, real laser light sources are specified by the M^2 -value, which serves as a similarity metric of the laser beam under test to an ideal fundamental Gaussian beam [10, 14]. For nearly Gaussian like beams, this performance criterion delivers meaningful results, which are useful for the prediction of the properties of the laser radiation. Unfortunately, the M^2 -value becomes more and more meaningless for amplitude and phase aberrations, as well as for a multimode laser beam in a way, that the reasons for the performance degradation cannot be distinguished by a single number. Especially in the field of beam shaping, the initial field distribution in terms of amplitude and

phase must be identified, since the shaping optics are highly intolerant to field distributions that deviate from the considered input field [15]. Therefore, the current methods can be highly improved by extending the laser beam characterization by differentiating between amplitude, phase and coherence. In addition, the simulation depth and accuracy of laser systems can be greatly enhanced by incorporating the real field distribution in the simulation towards a more holistic simulation, paving the way to a virtual rapid-prototyping of such systems.

One aim of this thesis is to introduce a new method for the characterization of coherent laser beams. This is done by reconstructing the amplitude and phase of the laser beams in order to gather a more comprehensive insight into the properties than the established M^2 -value. In this way, the influence of phase and amplitude perturbations can be distinguished and analyzed. Such perturbations are typically generated by the beam guiding optics due to non-perfect elements, tilted mirrors or misalignment. Simultaneously, it is intended to include the gathered information of the reconstructed amplitude and phase as the real field of the laser beam into the simulation of such systems. Thus, the physical modelling depth can be significantly improved and effects that are purely evoked by non-idealized laser beams can be simply included based on the measured data.

A relatively new field in the realm of laser beam shaping and characterization are Bessel beams or their realizable pendants with finite energy, called quasi Bessel beams [16–18]. They possess fundamentally different properties in comparison to classical beams with a spherical or parabolic wavefront. In particular the decoupling of their lateral from the axial extend make them a promising candidate for applications, where a strong lateral confinement of the light is required over a long axial distance [4, 19, 20]. The efficient handling of quasi Bessel beams in wave optical simulations is a challenging task due to their conical reference wavefront, which must be sampled sufficiently dense in the numerical evaluation of the corresponding diffraction calculations. Especially, if the quasi Bessel beams are perturbed by non-rotational wavefront aberrations, this becomes an even more complicated topic. The fast evaluation of such quasi Bessel beams is currently an open issue, which makes it an elaborated task to consider perturbed beams already in the design phase considering optimization and tolerancing.

The second aim of this thesis is to deliver an efficient tool for computing the on-axis field of most often used Bessel-Gauss beams that suffer from rotational and non-

rotational symmetric wavefront aberrations. Ideal Bessel-Gauss beams are characterized by a Gaussian amplitude and a conical reference wavefront. Typically, wavefront aberrations, such as spherical aberration, astigmatism and coma are caused by previous beam shaping optics, e.g., collimators and telescopes. The derived calculus enables the efficient analytic treatment of such perturbed Bessel-Gauss beams by evaluating the corresponding diffraction integrals by certain approximations like the method of stationary phase. With this fast calculation scheme, a diffraction based performance prediction of such systems can be already done in the design and tolerancing stage. For this purpose, the definition of the Strehl-ratio is extended along z -axis to account for the line focus of the generated perturbed Bessel-Gauss beams and to introduce a suitable and accessible performance criterion.

For increasing laser powers and demands on the optical performance, the importance of the optical system is growing [14, 21, 22]. An increasing laser power leads to an enhanced heat deposition in the material of the optical system, which changes the properties of the system itself. This is of particular interest for applications like laser cutting and drilling, where the axial position of the focus must be maintained independent of the applied laser powers. Thus, the optical systems must be designed to be insensitive to thermal changes, which is referred to as athermalization [23–25]. The challenge of laser systems is the inhomogeneous heat deposition which leads to gradient-index (GRIN) effects and the often uncertain boundary conditions of the mounted optical elements, that complicates the design and simulation of these systems. Thus, the complete modelling of such heat induced effects is complicated and typically involves finite-element methods and interdisciplinary considerations between mechanical, thermal as well as optical aspects [26, 27]. The finding of initial systems with appropriate material combinations, though is a challenge on its own, since it forms the basis of the performance in later design steps.

The third aim of this thesis therefore is to develop a concept for the passive athermalization of refractive optical beam shaping optics which can be used in high power laser applications. To this end, the steady-state temperature distribution of a thin lens, that is illumination by a high power fundamental Gaussian beam, is derived. Based on the thermal response of the material and the resulting GRIN effects, the additional heat induced focal power is deduced analytically and further analyzed. This is used to athermalize basic optical setups like a doublet, which consists of two lenses in close contact and two- and three-lens telescopes, based on the combina-

tion of different materials. With these considerations, a strategy for the paraxial athermalization of high power laser systems should be delivered, which enables to increase the laser power while maintaining the systems performance.

This thesis is structured in the following way. After the introduction, necessary fundamentals are introduced in chapter 2. Starting from Maxwell's equations, the wave equation and fundamental solutions like plane, spherical and Bessel beams are discussed. Furthermore, the paraxial wave equation is derived and Gaussian beams as a prominent solution are introduced. In addition, the transport of intensity equation is deduced, which forms the basis for the beam characterization approach in chapter 4. In the last section of this chapter, the geometrical optics region is presented by further approximating the wave equation, which results in the ray representation of light based on the eikonal equation. In chapter 3, necessary concepts to model optical systems are explained. To this end, the hybrid-approach is introduced to link various physical models with different modelling depths to each other. Additionally, several methods to evaluate the performance of optical systems and laser beams are described. This includes the definition of Zernike-polynomials for the specification and classification of wavefront aberrations, the Strehl-ratio as a metric of the system performance and the M^2 -value as a metric, that specifies the similarity of a laser beam to a fundamental Gaussian beam. Furthermore, techniques to profile quasi Bessel beams are presented, including the fundamental class of Bessel-Gauss beams, the introduction of the stationary phase approach for approximate solutions of typical diffraction integrals and a technique to effectively shape the on-axis intensity of quasi Bessel beams. In the last section of this chapter, basic ideas for the athermalization of singlets and doublets in case of a homogeneous temperature load are presented. A new method to reconstruct and characterize coherent laser beams is described in chapter 4. This is done by solving the transport of intensity equation under the specific consideration of the paraxial properties of ideal Gaussian beams and furthermore describing the wavefront aberrations by a set of laterally shifted Gaussian functions. This allows to solve the inverse phase retrieval problem by a least-square fit. The method is experimentally verified with the reconstruction and assessment of two real laser beams and the achieved accuracy is estimated based on the comparison with synthetic data. The amplitude and phase distributions are analyzed and used for comparative calculations of the M^2 -value. The reconstructed field is propagated and can be used as a real light source in further simulations. Chapter 5 provides a novel approach to calculate the on-axis field of a Bessel-Gauss

beam which is influenced by spherical aberration, astigmatism and coma. Additionally, the introduced Gaussian apodization function offers the possibility to describe a ring-shaped illumination. Based on the decomposition of the wavefront errors and the stationary phase approximation, an analytic formula for the field of the axial focus is derived. The introduced approximations are assessed and the results are evaluated against rigorous computations. Furthermore, the derived equation is used to analyze the tilt sensitivity of an exemplary optical system that collimates light emitted by a fiber and transforms the laser beam to a Bessel-Gauss beam by an axicon. For this purpose, an extended definition of the Strehl-ratio along the optical axis is implemented to account for the line focus of a Bessel-Gauss beam and to evaluate the performance effectively. In chapter 6, the conceptual possibilities for the passive athermalization of refractive high power laser systems are investigated. This is done by solving a modified heat equation inside a thin lens for a fundamental Gaussian laser beam illumination that heats up the lens due to bulk absorption. The resulting analytic temperature distribution is further used to compute the corresponding inhomogeneous change of the refractive index, which results in an additional focal power of the heated lens dependent on the used material, the applied laser parameters and the geometry of the lens. This additional heat induced focal power is analyzed and the specific material dependence is emphasized. The dominant terms of the focal power are used to athermalize basic optical systems like a doublet and telescopes consisting of two and three lenses in first order for non-homogeneous heating. With the help of these results, such systems are simulated and the real performance is compared to non-athermalized solutions. This thesis concludes with a summary and an outlook of potential future research based on this work.

2. Fundamentals

In this chapter the necessary fundamentals for this thesis are introduced. Starting from Maxwell's equations, basic concepts for the description of light as an electromagnetic wave are discussed. To this end, the wave equation is derived and basic solutions, such as plane, spherical and Bessel waves, are given. Furthermore, often required approximations of the wave equation are discussed to introduce Gaussian beams and the transport of intensity equations. In addition, the geometrical optic region is described to model light with rays by further approximating the wave equation.

2.1. Wave equation

Light, described as a vectorial electro-magnetic field, is governed by Maxwell's equations. Following the literature in [28–30], they are given in the spectral domain for a linear, nondispersive, isotropic and homogeneous medium as

$$\nabla \times \vec{E}(\vec{r}, \omega) = -i\omega\mu\vec{H}(\vec{r}, \omega), \quad (2.1)$$

$$\nabla \times \vec{H}(\vec{r}, \omega) = i\omega\epsilon\vec{E}(\vec{r}, \omega), \quad (2.2)$$

$$\nabla \cdot \vec{E}(\vec{r}, \omega) = 0, \quad (2.3)$$

$$\nabla \cdot \vec{H}(\vec{r}, \omega) = 0. \quad (2.4)$$

Here, ∇ is the nabla-operator, $\vec{E}(\vec{r}, \omega)$ is the electric field, $\vec{H}(\vec{r}, \omega)$ is the magnetic field, dependent on the position $\vec{r} = (x, y, z)^\top$ and spectral frequency ω . The electric permittivity and magnetic permeability are denoted as μ and ϵ , respectively. By relating both to their respective constants in vacuum μ_0 and ϵ_0 , an expression for the refractive index of the medium as an ratio of the speed of light inside the medium

c to the speed of light in vacuum c_0 is found

$$n = \frac{c}{c_0} = \sqrt{\frac{\mu\epsilon}{\mu_0\epsilon_0}}. \quad (2.5)$$

The wave equation can be derived by applying the curl operation on both sides of Eq. 2.1 and 2.2 and making use of the relation $\nabla \times (\nabla \times \vec{U}) = \nabla(\nabla \cdot \vec{U}) - \nabla^2 \vec{U}$

$$\nabla^2 \vec{E}(\vec{r}, \omega) + k^2 \vec{E}(\vec{r}, \omega) = 0, \quad (2.6)$$

$$\nabla^2 \vec{H}(\vec{r}, \omega) + k^2 \vec{H}(\vec{r}, \omega) = 0, \quad (2.7)$$

with the wavenumber k , expressed as $k = \frac{\omega}{c} = \frac{2\pi}{\lambda}$ and the wavelength λ . Since both equations have the same structure, it is sufficient to solve only for $\vec{E}(\vec{r}, \omega)$ or $\vec{H}(\vec{r}, \omega)$ and use Eq. 2.1 or 2.2 to calculate the other quantity. Therefore, in the further considerations of this thesis, only the electric field is used. Eq. 2.6 is separable into scalar equations for each vector component independent of the polarization and angle of propagation. In a homogeneous medium this is formulated as

$$\nabla^2 E(\vec{r}, \omega) + n^2 k_0^2 E(\vec{r}, \omega) = 0. \quad (2.8)$$

This is the scalar wave equation in a homogeneous medium, where $k_0 = k/n$ is the wavenumber in vacuum.

2.1.1. Plane waves

An elementary solution of Eq. 2.6 in homogeneous, non-conducting, isotropic media are monochromatic harmonic plane waves that are governed by their propagation direction described by the wave vector $\vec{k} = (k_x, k_y, k_z)^\top$. They can be formulated by [28–30]

$$\vec{E}(\vec{r}) = \vec{E} e^{i\vec{k} \cdot \vec{r}}. \quad (2.9)$$

The surfaces of constant phase, also called wavefronts, are perpendicular to the propagation direction. Thus, they are given by

$$\vec{k} \cdot \vec{r} = \text{const.} \quad (2.10)$$

Consecutive wavefronts are separated by their wavelength $\lambda = \frac{2\pi}{k}$. Since a plane wave has a constant amplitude everywhere, it contains an infinite amount of energy, clearly showing the idealization character of this theoretical model [28]. Monochromatic plane waves are used in particular for propagating fields between parallel planes in a homogeneous medium. Here, the field in the initial plane is first Fourier transformed to the domain of the angular spectrum

$$E(k_x, k_y, 0) = \mathcal{F}\{E(x, y, 0)\} = \frac{1}{\sqrt{2\pi}} \iint_{-\infty}^{+\infty} E(x, y, 0) e^{-i(k_x x + k_y y)} dx dy. \quad (2.11)$$

Then, the angular spectrum of the field is multiplied by a phase term, describing the propagation of plane waves to the position z

$$E(k_x, k_y, z) = E(k_x, k_y, 0) e^{ik_z z}, \quad (2.12)$$

$$k_z = \sqrt{k^2 - k_x^2 - k_y^2}. \quad (2.13)$$

By taking the inverse Fourier transform of Eq. 2.12, the propagated field is obtained in spatial coordinates

$$E(x, y, z) = \mathcal{F}^{-1}\{E(k_x, k_y, 0) e^{ik_z z}\}. \quad (2.14)$$

Therefore, this concept decomposes an arbitrary field into set of plane waves in terms of simple complex-exponential functions by a Fourier transform in order to propagate them by Eq. 2.12 and superpose them in the destination plane. Here, they are transformed back into spatial coordinates by an inverse Fourier transform [28–32].

The field is usually not accessible in experiments, since it is rapidly oscillating. But the intensity of a field can be measured with a camera, for example. Thus, the intensity of a field is an important quantity, which can be calculated for a monochromatic field as

$$I(x, y, z) = \frac{1}{2} c \epsilon_0 |E(x, y, z)|^2. \quad (2.15)$$

For the paraxial region (see section 2.2), the spherical shaped integral kernel of Eq. 2.13 can be approximated by the first terms of a power series expansion. Taking only the first order term corresponds to an approximation of the spherical shaped kernel function by a plane, which is called the Fraunhofer approximation. By in-

cluding the quadratic terms additionally, the spherical kernel is approximated by a parabola that is valid for the paraxial region (see section 2.2), the so-called Fresnel approximation. Both approximations are fundamental for understanding basic principles in the context of physical optics where diffraction must be considered. Thus, they enable extensive theoretical insights in terms of analytical results for many problems [28–33].

2.1.2. Spherical waves

Another solution of the Helmholtz equation are spherical waves. They can be formulated as

$$E(\vec{r}) = E_0 \frac{e^{i\vec{k}\cdot\vec{r}}}{r}. \quad (2.16)$$

The concept of spherical waves is of great significance, because they form the basis of the well-known Huygen’s principle. It states that every point on a wavefront is regarded as the source of a spherical wave, the so-called secondary wave. The sum of all secondary spherical waves can be regarded as the wavefront and the field at a distinct position is described as the interference of all secondary waves at this position. This is mathematically formulated for example in the sense of the first Rayleigh-Sommerfeld integral [28, 31, 32]

$$E(\vec{r}) = \iint_A E(\vec{r}_0) \frac{1}{2\pi} \left(ik - \frac{1}{|\vec{r} - \vec{r}_0|} \right) \frac{e^{ik|\vec{r} - \vec{r}_0|}}{|\vec{r} - \vec{r}_0|} \frac{z}{|\vec{r} - \vec{r}_0|} dA'. \quad (2.17)$$

2.1.3. Bessel beams

In contrast to the previous fundamental solutions of the wave equation, Bessel beams are relatively new. They were theoretically described and experimentally investigated in 1987 [16, 17]. The Bessel beam solution can be found by the following rotational-symmetric ansatz-function for a monochromatic field with the unknown amplitude $A(\rho)$ in polar coordinates $\rho^2 = x^2 + y^2$

$$E(\vec{r}) = A(\rho)e^{ik_z z}. \quad (2.18)$$

Inserting this into the Helmholtz equation in polar coordinates leads to

$$\rho^2 \frac{\partial^2}{\partial \rho^2} A(\rho) + \rho \frac{\partial}{\partial \rho} A(\rho) + k_\rho^2 \rho^2 A(\rho) = 0, \quad (2.19)$$

$$k^2 = k_x^2 + k_y^2 + k_z^2 = k_\rho^2 + k_z^2. \quad (2.20)$$

Eq. 2.19 is known as Bessel's differential equation [18,33]. The most simple solution for this differential equation excluding singular values at $\rho = 0$ can be formulated as

$$A(\rho) = A_0 J_0(k_\rho \rho), \quad (2.21)$$

with the constant A_0 and the zero-order Bessel function of the first kind J_0 . Thus, the Bessel beam provides a solution of the wave equation where the field amplitude is invariant during propagation along z . The more general solution of Eq. 2.19 can be formulated by Bessel functions of the first kind of order n and an additional helical phase term, forming ring shaped intensity distribution with a zero on-axis [18,29,33]. In this thesis, those higher order Bessel beams play no particular role. Therefore, only zero order Bessel beams are regarded in the following. They are characterized by a cone-shaped wavefront. To better understand this property consider the following representation of J_0 as an integral [18]:

$$J_0(k_\rho \rho) = \frac{1}{2\pi} \int_0^{2\pi} e^{ik_\rho(x \cos(\phi) + y \sin(\phi))} d\phi. \quad (2.22)$$

The full x, y, z dependence is obtained by

$$E(\vec{r}) = \frac{A_0}{2\pi} \int_0^{2\pi} e^{ik_\rho(x \cos(\phi) + y \sin(\phi)) + ik_z z} d\phi \quad (2.23)$$

$$= \frac{A_0}{2\pi} \int_0^{2\pi} e^{i\vec{q} \cdot \vec{r}} d\phi. \quad (2.24)$$

This integral with the wave vector $\vec{q} = (k_\rho \cos(\phi), k_\rho \sin(\phi), k_z)^\top$ can be interpreted physically. It states that a fundamental Bessel mode consists of all possible plane waves with a length defined by Eq. 2.20 and a polar inclination of $\tan(\alpha) = \frac{k_\rho}{k_z}$. In addition, the azimuthal angle ϕ is completely unrestricted. Thus, those waves are located on the surface of a cone which is defined by the opening angle α . Similar to a plane wave, a Bessel beam contains an infinite amount of energy due to the slow convergence of the Bessel function. The major difference between both solutions is

the energy density. It is constant for a plane wave, but it is maximum at $\rho = 0$ in case of a fundamental Bessel beam described by Eq. 2.21. Furthermore, the size of the central spot radius in terms of the first root of the Bessel function can be extremely narrow, on the order of one wavelength, making it attractive for applications where a narrow and long focus is required. Further discussion regarding the properties and realizable versions of Bessel-kind beams are given in section 3.3 and chapter 5.

2.2. Paraxial wave equation

A wave is denoted to be paraxial for small propagation angles α with respect to the propagation direction along z . Thus, the paraxial wave propagates nearly parallel to the z -axis, which can be formulated as $k_z = k \cos(\alpha) \approx k$. The fast variation of the field along z can then be separated by the factorization [9, 28, 29]

$$E(\vec{r}) = A(\vec{r})e^{i\vec{k}\cdot\vec{r}} = V(\vec{r})e^{ik_z z}. \quad (2.25)$$

Inserting this into the Helmholtz equation (Eq. 2.8) results in

$$0 = \nabla^2 E + k^2 E = e^{ik_z z} \left(\nabla^2 V - k_z^2 V + 2ik_z \frac{\partial V}{\partial z} + k^2 V \right). \quad (2.26)$$

Within the paraxial approximation and by assuming only a weak change of the amplitude V along z

$$\left| \frac{\partial^2 V}{\partial z^2} \right| \ll k \left| \frac{\partial V}{\partial z} \right|, \quad (2.27)$$

the paraxial wave equation with the transverse Laplace operator $\nabla_{\perp}^2 = \frac{\partial^2}{\partial x^2} + \frac{\partial^2}{\partial y^2}$ can be deduced

$$0 = \nabla_{\perp}^2 V + 2ik \frac{\partial V}{\partial z}. \quad (2.28)$$

This is also known as slowly varying envelope approximation of the Helmholtz equation or paraxial Helmholtz equation [9, 28, 29, 31, 33].

2.2.1. Gaussian beams

A simple solution of the paraxial wave equation are paraboloidal waves which can be written in rotational symmetry as [28, 29]

$$A(\vec{r}) = \frac{A_1}{z} e^{ik \frac{\rho^2}{2z}}, \quad (2.29)$$

with the constant A_1 . They can be interpreted as the paraxial approximation of a spherical wave, where the spherical wavefront is approximated by a parabola making them closely related to the Fresnel approximation [9, 28, 29, 31, 33]. By introducing a shift $q(z) = z - z_s$, their origin is transformed from $z = 0$ to $z = z_s$. This is also valid for a complex-valued z_s and q can be expressed as $q(z) = z + iz_R$. The complex envelope of the Gaussian beam can be formulated as

$$A(\vec{r}) = \frac{A_1}{q(z)} e^{ik \frac{\rho^2}{2q(z)}}. \quad (2.30)$$

Separating the inverse of $q(z)$ into real and imaginary parts and introducing $R(z)$ and $w(z)$, such that

$$\frac{1}{q(z)} = \frac{1}{R(z)} - i \frac{\lambda}{\pi w^2(z)}, \quad (2.31)$$

allows to separate between amplitude and phase of the complex envelope by inserting Eq. 2.31 into Eq. 2.30 leading to the famous expression for a Gaussian beam

$$A(\vec{r}) = \frac{A_1}{iz_R} \frac{w_0}{w(z)} e^{-\frac{\rho^2}{w^2(z)}} e^{i \left(kz + \frac{k\rho^2}{2R(z)} + g(z) \right)}. \quad (2.32)$$

The beam parameters in Eq. 2.32 are the beam width at $1/e$ of the amplitude $w(z)$, the corresponding minimum beam width w_0 at the focus and the radius of curvature of the parabolic wavefront $R(z)$. z_R is the so-called Rayleigh length, defined as the length along z , where the beam widens from the focus position to $w(z) = \sqrt{2}w_0$ and the intensity is reduced to half of that peak intensity I_0 . The peak intensity is closely related to the total power of the beam P . $g(z)$ refers to the Gouy-phase, that is a retardation of the phase in relation to a plane wave or spherical wave. The relations of the beam parameters are:

$$w_0 = \sqrt{\frac{\lambda z_R}{\pi}}, \quad (2.33)$$

$$w(z) = w_0 \sqrt{1 + \left(\frac{z}{z_R}\right)^2}, \quad (2.34)$$

$$\theta = \frac{w_0}{z_R}, \quad (2.35)$$

$$R(z) = z \left(1 + \left(\frac{z_R}{z}\right)^2\right), \quad (2.36)$$

$$g(z) = \tan^{-1} \left(\frac{z}{z_R}\right), \quad (2.37)$$

$$I_0 = \left|\frac{A_1}{z_R}\right|^2, \quad (2.38)$$

$$P = \frac{\pi}{2} I_0 w_0^2. \quad (2.39)$$

For $z \gg z_R$ the beam waist can be approximated by $w(z) \approx \frac{w_0}{z_R} z = \theta z$, where θ is called the far field divergence angle [9, 28, 29, 31, 33].

2.2.2. Transport of intensity equation

The transport of intensity equation (TIE) can be derived based on the paraxial wave equation (Eq. 2.28) and the following ansatz-function [28, 32, 34–37]

$$V(\vec{r}) = A(\vec{r})e^{ik\Phi(\vec{r})} = \sqrt{I(\vec{r})}e^{ik\Phi(\vec{r})}. \quad (2.40)$$

Here, I is proportional to the intensity defined in Eq. 2.15. The complex field is separated into amplitude A and phase Φ , respectively. Inserting Eq. 2.40 into Eq. 2.28, yields to

$$0 = \nabla_{\perp}^2 A + 2i\nabla_{\perp} A \cdot \nabla_{\perp} \Phi - A(\nabla_{\perp} \Phi)^2 + iA\nabla_{\perp}^2 \Phi + 2ik\frac{\partial A}{\partial z} - 2kA\frac{\partial \Phi}{\partial z}. \quad (2.41)$$

Thus, the real and the imaginary parts of Eq. 2.41 must equal zero, forming two separate equations. The equation of the real parts can be called transport of phase equation. The TIE is found from the imaginary part of Eq. 2.41 and replacing the amplitude terms by their respective intensity terms with $\frac{\partial A}{\partial x} = \frac{\partial}{\partial x} \sqrt{I} = \frac{\frac{\partial I}{\partial x}}{2\sqrt{I}}$

$$-k\frac{\partial I}{\partial z} = \nabla_{\perp} I \cdot \nabla_{\perp} \Phi + I\nabla_{\perp}^2 \Phi = \nabla_{\perp} \cdot (I\nabla_{\perp} \Phi). \quad (2.42)$$

Consequently, the TIE connects the intensity variation along z with the lateral gradient of the intensity and phase as well as with the curvature of the phase. It offers the possibility to retrieve the phase of a field by measuring pure intensities at different positions along z with, e.g., a movable camera. This idea is used in chapter 4 to reconstruct and characterize the field of real coherent laser sources.

2.3. Light as rays

In literature, the geometrical optical regime is referred to where the vacuum wavelength is vanishing small in comparison to surrounding structures. For a monochromatic wave inside a medium with slowly varying refractive index n , the complex amplitude can be written as [29, 32, 38]

$$E(\vec{r}) = A(\vec{r})e^{ik_0S(\vec{r})}, \quad (2.43)$$

with the amplitude A and the phase $k_0S(\vec{r})$. Inserting this into the scalar wave equation yields

$$0 = k_0^2[n^2(\vec{r}) - |\nabla S|^2]A + \nabla^2 A + ik_0[2\nabla S \cdot \nabla A + A\nabla^2 S]. \quad (2.44)$$

Similar to the paraxial wave equation, the real and the imaginary parts must equal zero. For the real part, we find

$$0 = k_0^2[n^2(\vec{r}) - |\nabla S|^2]A + \nabla^2 A. \quad (2.45)$$

Assuming a slowly varying amplitude and $k_0 \rightarrow \infty$ leads to the Eikonal equation that is forming the fundamental basis of geometrical optics

$$|\nabla S|^2 = n^2. \quad (2.46)$$

The scalar function S is proportional to the phase in wave optics and is called the eikonal. It can be interpreted as the wavefront with $S(\vec{r}) = \text{constant}$. The wavevector is oriented perpendicular to the wavefront pointing in the direction of ∇S . Thus, the field can be locally regarded as a plane wave with a given amplitude traveling into the direction of $\vec{k} \parallel \nabla S$. This analogy allows to describe the evolution of a field by a set of local plane waves in terms of simple rays.

3. Modelling of beam profiling systems

In this chapter, different state-of-the-art methods to model beam profiling systems are discussed. For this purpose, the hybrid approach which connects different appropriate models of light within an optical system is introduced. In addition, fundamental opportunities to quantify and characterize the performance of profiled beams are given in terms of the wavefront decomposition into Zernike-polynomials [28, 39, 40] and the influence of wavefront aberrations onto the diffraction pattern in the focus by calculating the Strehl-ratio [28, 41–45]. Furthermore, the beam propagation factor M^2 is introduced allowing to compare arbitrary beams with the fundamental Gaussian mode [10, 14, 28, 46, 47]. Then, quasi Bessel beams are presented and used to shape the on-axis intensity within the created Bessel-zone [16–18, 47, 48]. In the last section, the impact of a homogeneous temperature change on the system performance is discussed by deriving the resulting defocus effect of a heated thin lens singlet and doublet. This is used to exploit the potential for the athermalization of optical systems [21–23, 38, 49].

3.1. Hybrid approach for optical systems

In the geometrical realm, a classical optical system can be described by several distinguished surfaces. In principle, those are the object surface, the functional surfaces, e.g., lens surfaces, and the image surface. Another possibility for the description of a classical optical system is to define the pupil planes, which are based on the physical aperture stop of the system. The entrance and exit pupils are the conjugate planes of the aperture stop in the object and image space, respectively. The rays transmitted by the optical system can be sampled in the entrance pupil

[38, 49]. When they reach the exit pupil, the rays have been influenced by all the components of the system. Hence, the rays in the exit pupil carry several information of the optical system, allowing to describe certain properties of the optical system by the rays in the exit pupil. To analyze an optical system, the optical path length L can be computed and evaluated in the exit pupil by the following definition

$$L = \int_{\vec{r}_0}^{\vec{r}_1} n(\vec{r}) ds. \quad (3.1)$$

The optical path length can be understood as an effective path length of the individual rays traveling from \vec{r}_0 to \vec{r}_1 along the path element ds satisfying Eq. 2.46 [38, 49]. A single object point creates a spherical wave. Therefore, the optical path lengths of the rays emerging from a single object point correspond to a spherical wave in the entrance pupil. Since, the entrance and exit pupil are conjugated, L is also spherical in the exit pupil for an ideal imaging system. Thus, all rays intersect at a single point in the image plane. This ideal spherical surface in the exit pupil is denoted as reference sphere. For an infinite imaging condition, the spherical shape obviously degenerates to a plane surface where all rays are parallel.

General imaging can be considered as non-ideal and aberrations must be included, therefore. They can be interpreted as an undesired change of direction in the ray picture. The description of such aberrations can be done in two different reference systems. The transverse ray aberrations are identified in the image plane and measured as the transverse difference between the real and the ideal intersection point. The longitudinal ray aberrations are identified as the difference in intersection lengths between the real and ideal ray along the optical axis of the system. Both concepts are extensively discussed in literature [30, 33, 49]. Another concept for describing the aberrations occurring in optical systems are based on wave aberrations. With the Eikonal equation, the direction of a ray is connected to the phase in the wave optical description by the interpretation of a single ray as a local plane wave. In contrast to the transverse and longitudinal ray aberrations, the wave aberrations are typically described in the exit pupil of the system. Both concepts are equivalent and can be transferred into each other [28]. To calculate the wave aberrations, the optical path length as a function of the exit pupil coordinates $L(x_p, y_p)$ is identified. This can be done by evaluating Eq. 3.1 on a grid that is transferred from the entrance to the exit pupil. Typically the optical path length is referenced to the chief

ray resulting in the optical path difference

$$\Delta L(x_p, y_p) = L(x_p, y_p) - L(0, 0). \quad (3.2)$$

Thus, the emerging ray aberrations can be included in the complex field of the exit pupil as a phase term

$$E(x_p, y_p) = A(x_p, y_p)e^{ik\Delta L(x_p, y_p)}. \quad (3.3)$$

It is often beneficial to scale the phase aberrations with the wavelength, which might be expressed as

$$E(x_p, y_p) = A(x_p, y_p)e^{i2\pi W(x_p, y_p)}, \quad (3.4)$$

where $W(x_p, y_p)$ is then designated as wavefront aberration [28]. The hybrid approach for the simulation of optical systems typically utilizes a ray based description of light from the object plane or entrance pupil to the exit pupil of the system. In the exit pupil the rays are converted to a phase function by Eq. 3.2 and the field is modeled by Eq. 3.3 or 3.4. This allows to calculate wave optical phenomena like diffraction by propagating the field from the exit pupil to the image plane, utilizing an appropriate propagator (e.g., Eq. 2.14). Thus, within the hybrid approach different levels of the model complexity for the description and interaction of light are used. Inside the system the wavelength is usually vanishing small in comparison to the dimensions of the components justifying the geometrical model. Additionally, ΔL can become quite large inside the system, which would require a high sampling of the phase term. Even more computationally expensive is the evaluation of the field on curved surfaces [50,51], indicating the challenges of a full wave optical description of optical systems. In contrast to the situation inside the system, the dimension in the focal region can be on the order of λ . Thus, the wave optical nature of light in terms of diffraction becomes a significant portion and cannot be neglected. Consequently, the model is adapted in the transition from the exit pupil to the focal region by switching from rays to waves. A sketch of an exemplary system is shown in Fig. 3.1. The purpose of this system is the adaptation of the numerical aperture and refocusing. It consists of a fiber coupled laser source emitting a fundamental Gaussian laser beam with a NA given by the fiber. The diverging beam is collimated using a doublet and refocused by a single lens. In the sketch, four different regions are indicated by (1)-(4) to distinguish between different simulation mod-

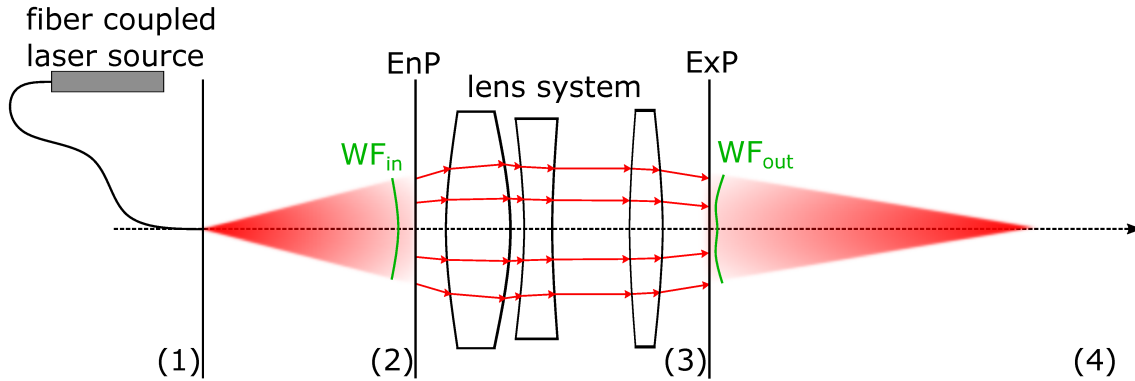


Figure 3.1.: Sketch of the hybrid approach for the description and simulation of NA adapting optical setup consisting of a fiber coupled laser source and a collimation of focusing optics consisting of three lenses. Distinct regions are indicated by (1)-(4), where different simulation models are applied.

els as discussed before. In (1) the light emitted by the laser, is guided through a single-mode fiber and a fundamental Gaussian mode is assumed to be outcoupled. This ideal Gaussian mode is propagated in (2) by the Gaussian beam model to the entrance pupil of the system (EnP). Here, the corresponding wavefront (WF_{in}) is of ideal parabolic shape according to Eq. 2.36 and the field is transferred into a ray-based representation [52]. In this way, simple rays can be traced through the lens system in (3). In case of a non-ideal configuration of the lenses, ray aberrations occur. They are identified as ΔL in the outgoing wavefront (WF_{out}) of the system in the exit pupil (ExP). Here, the ray-based representation of the light carrying the information is changed to a wave-optical representation according to Eq. 3.4 and the resulting field can be propagated for example by Eq. 2.14 in region (4). In chapter 4, similar real laser system are investigated. The output field is reconstructed solving the TIE and evaluated by decomposing the wavefront into Zernike-polynomials and calculating the M^2 -value. Both are introduced in the next section.

3.2. Performance metrics

In this section, different concepts describing the performance of beams based on wave optical considerations are introduced. Therefore, the Zernike-polynomials which are classically used in the description of wavefront aberrations [28, 49, 53], are defined. Moreover, the wavefront aberrations are connected to the diffraction effect in the far field by the concept of the classical Strehl-ratio [28, 41–45]. For the characterization

of laser beams, the beam propagation factor M^2 is calculated which offers the possibility to estimate the similarity of a laser beam to the fundamental Gaussian laser mode in terms of the intensity distribution and wavefront aberrations [10, 14, 28, 46]. The comparison to the fundamental Gaussian mode is especially useful, because this beam has the smallest space-bandwidth-product and thus enables a stronger focusing of the beam.

3.2.1. Zernike-polynomials

A common approach to describe the wavefront aberrations of classical rotational symmetric systems is to decompose them into Zernike-polynomials [28, 39, 40]. They are orthogonal functions defined on the unit circle. With the Zernike-polynomials, typically, only a few orders are necessary to approximate the wavefront aberrations satisfactory due to their similarity to classical aberrations reducing the computational effort. Additionally, the decomposition offers the possibility to classify certain types of aberrations allowing for a deeper insight into the properties of the wavefront aberrations and consequently leading to a better understanding of the properties of the optical system. The definition of the decomposition is

$$W(\bar{\rho}, \phi) = \sum_n \sum_{m=-n}^n c_{nm} Z_n^m(\bar{\rho}, \phi). \quad (3.5)$$

Here, $\bar{\rho}$ is the normalized radial coordinate, ϕ is the azimuthal angle. The radial and azimuthal order of the expansion are n and m , respectively. The corresponding radial and azimuthal terms are calculated as [30]

$$Z_n^m(\bar{\rho}, \phi) = R_n^m(\bar{\rho}) \begin{cases} \sin(m\phi) & \text{for } m > 0 \\ \cos(m\phi) & \text{for } m \leq 0 \end{cases}, \quad (3.6)$$

$$R_n^m(\bar{\rho}) = \begin{cases} \sum_{k=0}^{\frac{n-m}{2}} \frac{(-1)^k (n-k)!}{k! (\frac{n+m}{2}-k)! (\frac{n-m}{2}-k)!} \bar{\rho}^{n-2k} & \text{for even } n-m \\ 0 & \text{for odd } n-m \end{cases}. \quad (3.7)$$

In literature, there are different ordering schemes and scalings suggested [40, 54]. In the context of this thesis, the Fringe-convention and the ordering with a single index

j is used. The index conversion from j to n and m is

$$m = \begin{cases} 0 & \text{for } d_2 = 0 \\ \frac{d_1^2 - j}{2} & \text{for even } d_2, \\ \frac{j-1-d_1^2}{2} & \text{else} \end{cases} \quad (3.8)$$

$$n = 2(d_1 - 1) - |m|, \quad (3.9)$$

$$d_1 = \lfloor \sqrt{j-1} \rfloor + 1, \quad (3.10)$$

$$d_2 = d_1^2 - j. \quad (3.11)$$

The labeling of distinct orders to classical Seidel aberrations and the corresponding formulas in Cartesian coordinates can be found in Tab. A.1.

3.2.2. Strehl-ratio

The classical Strehl-ratio (SR) describes the degradation of the on-axis intensity $I(\rho_i = 0)$ of the focal spot including wavefront aberrations compared to the ideal aberration free case [28, 41–45]

$$SR = \frac{I_{\text{perturbed}}(\rho_i = 0)}{I_{\text{ideal}}(\rho_i = 0)}. \quad (3.12)$$

It connects wavefront aberrations in the exit pupil with diffraction effects in the image location. This is particularly useful for systems performing close to the diffraction limit. An analytic expression for the degradation of the SR can be derived by formulating Eq. 3.12 in terms of the Fresnel diffraction integral [28], which reads in polar coordinates as

$$E(\rho_i, \phi_i, z) = \frac{k}{i2\pi z} e^{ikz + \frac{ik\rho_i^2}{2z}} \int_0^R \int_0^{2\pi} E_0(\rho_p, \phi_p) e^{\frac{ik\rho_p^2}{2z} - \frac{ik\rho_p\rho_i}{z} (\cos(\phi_p)\cos(\phi_i) + \sin(\phi_p)\sin(\phi_i))} \rho_p d\phi_p d\rho_p. \quad (3.13)$$

Classically, the field is assumed to have a uniform amplitude and a parabolic phase $e^{-\frac{ik\rho_p^2}{2r}}$, where $r = z$ is the distance from the pupil to the focus [41]. Inserting this

into Eq. 3.12 yields

$$SR = \frac{\left| \int_0^R \int_0^{2\pi} e^{i2\pi W(\rho_p, \phi_p)} \rho_p d\rho_p d\phi_p \right|^2}{\left| \int_0^R \int_0^{2\pi} \rho_p d\rho_p d\phi_p \right|^2}, \quad (3.14)$$

where the integral over the phase term including wavefront aberrations W has to be computed. This can be done by expanding W into a Taylor series up to second order, resulting in

$$SR \approx \frac{\left| \int_0^R \int_0^{2\pi} (1 + i2\pi W(\rho_p, \phi_p) - 2\pi^2 W^2(\rho_p, \phi_p)) \rho_p d\rho_p d\phi_p \right|^2}{\pi^2 R^4}. \quad (3.15)$$

Additionally, the n^{th} order moment of W is defined as

$$\langle W^n \rangle = \frac{1}{\pi R^2} \int_0^R \int_0^{2\pi} W^n(\rho_p, \phi_p) \rho_p d\rho_p d\phi_p. \quad (3.16)$$

With this definition, Eq. 3.15 can be reformulated as

$$SR \approx |1 + i2\pi \langle W^1 \rangle - 2\pi^2 \langle W^2 \rangle|^2. \quad (3.17)$$

Keeping only terms up to second order yields

$$SR \approx 1 - (2\pi)^2 (\langle W^2 \rangle - \langle W^1 \rangle^2) = 1 - (2\pi)^2 W_{RMS}^2. \quad (3.18)$$

Here, W_{RMS} is the root-mean square value of the wavefront aberrations. This equation is often used in literature to estimate the performance of optical systems in terms of the Strehl degradation for a constant illumination of the pupil and small wavefront aberrations. The classical Maréchal criterion, which is based on defining the diffraction limit as $SR = 0.8$ can be deduced by Eq. 3.18, resulting in $W_{RMS} \approx \frac{\lambda}{14}$. There are many extensions of this concept in literature, dealing with non-homogeneous illuminations of the pupil, the evaluation for certain types of aberrations or for different colors [41–44, 55]. A brief overview of the connection between distinct Zernike coefficients and the diffraction limit is given in Table 3.1. The concept of evaluating the systems performance in terms of the SR is revisited in section 5.3, where it is applied for the characterization of the line focus along z , generated by perturbed Bessel-Gauss beams.

classification	Zernike coefficient	diffraction limit
defocus	c_4	0.12λ
astigmatism	$c_{5,6}$	0.17λ
coma	$c_{7,8}$	0.20λ
spherical aberration	c_9	0.16λ

Table 3.1.: Diffraction limit of selected low order Zernike coefficients in the Maréchal approximation.

3.2.3. The beam propagation factor M^2

According to the ISO 11146 titled with "*Lasers and laser-related equipment – Test methods for laser beam widths, divergence angles and beam propagation ratios*", every laser beam can be characterized by ten independent parameters within the method of second order moments. However, most laser beams of practical use need fewer parameters due to symmetry. Therefore, to keep the formulations compact, the properties of simple astigmatic beams are discussed in the following based on the explanations given in [10].

First order moments

The first order spatial and angular moments, $\langle x \rangle$ and $\langle \theta_x \rangle$, of a laser beam in x -direction are defined as

$$\langle x \rangle = \frac{1}{P_N} \iint_{-\infty}^{+\infty} |E(x, y)|^2 x \, dx dy, \quad (3.19)$$

$$\langle \theta_x \rangle = \frac{1}{P_N} \iint_{-\infty}^{+\infty} |E(k_x, k_y)|^2 k_x \, dk_x dk_y. \quad (3.20)$$

Here, P_N is a normalization factor, which is related to the power of the beam. The same formulations can be done likewise in y -direction. To stay consistent with the literature the angular moment is abbreviated with $\langle \theta_x \rangle$ instead of $\langle k_x \rangle$. $\langle x \rangle$ and $\langle \theta_x \rangle$ are the center of gravity of the intensity in the near and far field, respectively. In the realm of the Fraunhofer approximation the far field corresponds to a Fourier transform of the field (similar to Eq. 2.11). Thus, the first order moments provide the center of gravity of the intensity and its direction of propagation. In spatial

domain, Eq. 3.20 can also be formulated as

$$\langle \theta_x \rangle = \frac{-k}{P_N} \iint E(x, y) \frac{\partial E^*(x, y)}{\partial x} dx dy. \quad (3.21)$$

Second order moments

For a centered ($\langle x \rangle = \langle y \rangle = 0$) simple astigmatic beam the second order moments are defined by

$$\langle w_x^2 \rangle = \frac{4}{P_N} \iint_{-\infty}^{+\infty} |E(x, y)|^2 x^2 dx dy, \quad (3.22)$$

$$\langle \theta_x^2 \rangle = \frac{4\lambda^2}{P_N} \iint_{-\infty}^{+\infty} |E(k_x, k_y)|^2 k_x^2 dk_x dk_y. \quad (3.23)$$

Similarly to the first order moments, Eq. 3.23 can also be written as

$$\langle \theta_x^2 \rangle = \frac{\lambda^2}{\pi^2 P_N} \iint_{-\infty}^{+\infty} \left| \frac{\partial E(x, y)}{\partial x} \right|^2 dx dy. \quad (3.24)$$

Additionally, a mixed second order moment exist, which is

$$\langle w_x \theta_x \rangle = \frac{-i\lambda}{\pi P_N} \iint_{-\infty}^{+\infty} \left(E(x, y) \frac{\partial E^*(x, y)}{\partial x} - E^*(x, y) \frac{\partial E(x, y)}{\partial x} \right) x dx dy. \quad (3.25)$$

In the scenario of an aligned astigmatic Gaussian fundamental mode, the second order moments correspond to the waist, the far field divergence angle and the radius of curvature of the beam along the main axes, which are already described in Eq. 2.34-2.36.

$$\langle w_x^2 \rangle = w_x^2, \quad (3.26)$$

$$\langle \theta_x^2 \rangle = \theta_x^2, \quad (3.27)$$

$$\langle w_x \theta_x \rangle = \frac{w_x^2}{R_x}. \quad (3.28)$$

At the beams waist, the wavefront is a plane surface, corresponding to an infinite radius of curvature. Thus, a possibility to define the waist of an arbitrary field is obtained by $\langle w_x \theta_x \rangle = 0$.

A general beam can be characterized in a similar way. Instead of six independent

parameters, there are four additional parameters. The properties of a general beam can be arranged in a 4×4 matrix [56]

$$P = \begin{pmatrix} \langle w_x^2 \rangle & \langle w_x w_y \rangle & \langle w_x \theta_x \rangle & \langle w_x \theta_y \rangle \\ \langle w_x w_y \rangle & \langle w_y^2 \rangle & \langle w_y \theta_x \rangle & \langle w_y \theta_y \rangle \\ \langle w_x \theta_x \rangle & \langle w_y \theta_x \rangle & \langle \theta_x^2 \rangle & \langle \theta_x \theta_y \rangle \\ \langle w_x \theta_y \rangle & \langle w_y \theta_y \rangle & \langle \theta_x \theta_y \rangle & \langle \theta_y^2 \rangle \end{pmatrix}. \quad (3.29)$$

Within P , the rotations of the near and far field intensity with respect to the reference frame are characterized by $\langle w_x w_y \rangle$ and $\langle \theta_x \theta_y \rangle$, respectively. The mixed moments $\langle w_x \theta_y \rangle$ and $\langle w_y \theta_x \rangle$ describe the orbital angular momentum. For a simple astigmatic beam with six independent parameters P reduces to

$$P_{SA} = \begin{pmatrix} \langle w_x^2 \rangle & 0 & \langle w_x \theta_x \rangle & 0 \\ 0 & \langle w_y^2 \rangle & 0 & \langle w_y \theta_y \rangle \\ \langle w_x \theta_x \rangle & 0 & \langle \theta_x^2 \rangle & 0 \\ 0 & \langle w_y \theta_y \rangle & 0 & \langle \theta_y^2 \rangle \end{pmatrix}. \quad (3.30)$$

The generalized propagation factor of a beam is invariant with propagation through a paraxial optical system. It is computed by

$$M^2 = \frac{\pi}{\lambda} \det(P)^{\frac{1}{4}}. \quad (3.31)$$

Only for a fundamental Gaussian mode $M^2 = 1$, for any other type of beam it is larger. In case of a simple astigmatic beam Eq. 3.31 simplifies to

$$M_{SA}^2 = \sqrt{M_x^2 M_y^2}, \quad (3.32)$$

$$M_x^2 = \frac{k}{2} \sqrt{\langle w_x^2 \rangle \langle \theta_x^2 \rangle - \langle w_x \theta_x \rangle^2} \geq 1, \quad (3.33)$$

$$M_y^2 = \frac{k}{2} \sqrt{\langle w_y^2 \rangle \langle \theta_y^2 \rangle - \langle w_y \theta_y \rangle^2} \geq 1. \quad (3.34)$$

$$(3.35)$$

Thus, a simple aligned astigmatic Gaussian beam can still have an $M^2 = 1$, meaning that astigmatism is not degrading the performance of the laser beam in terms of M^2 . This is in contrast to the previously introduced performance metric of the Strehl-ratio, which is degraded by astigmatic wavefront aberrations. The reason is that the classical Strehl definition is referenced to a rotational-symmetric field. The

influence of spherical aberration and certain intensity profiles on the M^2 -value is investigated in [57]. Here, a strong coupling between phase aberrations and their weighting in terms of the intensity distribution is observed. Hence, the separation between phase or amplitude errors is complicated in real applications.

In chapter 4 the M^2 -value is used for the characterization of real laser beams after the field is reconstructed based on the phase retrieval approach solving the TIE. Within this approach, the phase and amplitude of the inspected field are described simultaneously and can be easily separated. Consequently, this enables a deeper insight into the properties of the beam under test.

3.3. Profiling of quasi Bessel beams

In section 2.1.3, an ideal Bessel beam with its infinite spatial extension was introduced and discussed as an solution of the wave equation according to Eq. 2.21. However, in practical situations the spatial extend of light is always limited and only approximations of Bessel beams can be obtained. Those approximated Bessel beams can be called quasi Bessel beams creating a so-called Bessel zone, where similar properties in terms of lateral and axial amplitude distribution compared to the ideal pendant are observable [16–18, 47, 48]. Such quasi Bessel beams can be described in polar coordinates within the Fresnel regime analytically by using Eq. 3.13 and separating the amplitude and phase of the field in the exit pupil ($z = 0$) by

$$E_0(\rho_p, \phi_p) = E_0(\rho_p) = A(\rho_p)e^{ik\epsilon\rho_p}, \quad (3.36)$$

where the conic wavefront can be defined in terms of the numerical aperture NA of the system with $\epsilon = -\tan(\sin^{-1}(NA))$. This particular wavefront shape can be generated for example by an axicon, which can transform a plane wavefront of an incoming collimated beam into a conical shape [16, 17, 47, 58]. The resulting Fresnel diffraction equation can be solved analytically in special situations. Characteristic for the generated beam are the lateral and axial extend. For an ideal conic shaped wavefront, the relative lateral intensity distribution is invariant along z inside the Bessel-zone. The first ring with no intensity occurs at $\rho_i = 0.38\frac{\lambda}{NA}$, which is smaller compared to the classical Airy disc radius where the first dark ring occurs at $\rho_i = 0.61\frac{\lambda}{NA}$ [28, 32]. In contrast to the ideal Bessel beams, the axial intensity

distribution is dependent on the apodization function $A(\rho_p)$, which is demonstrated in the following.

3.3.1. Bessel-Gauss beam

One possible realization of a quasi Bessel beam can be a Bessel-Gauss beam, where the amplitude is described by a Gaussian envelope function. It plays an important role due to its close relation to real applications where typical laser sources are used for illumination [4, 19, 20, 48]. For a Gaussian apodization function, defined by $A(\rho_p) = A_0 e^{-\rho_p^2/w^2}$, which is truncated at $\rho_p = R$, the on-axis field can be calculated in terms of inverse error functions $\operatorname{erfi}(x)$ [59]

$$\begin{aligned}
E(0, z) = & \frac{A_0 k w^2}{2(kw^2 + 2iz)^{3/2}} \exp\left(ikz \left(1 - \frac{\epsilon^2 k w^2}{2kw^2 + 4iz}\right)\right) \cdot \\
& \left[2\sqrt{kw^2 + 2iz} \left(\exp\left(\frac{i\epsilon^2 k^2 w^2 z}{2kw^2 + 4iz}\right) - \exp\left(\frac{i(kw^2(\epsilon z + R) + 2iRz)^2}{2w^2 z(kw^2 + 2iz)}\right) \right) + \right. \\
& (1+i)\sqrt{\pi z} \epsilon k w \operatorname{erfi}\left(\frac{\sqrt[4]{-1}(kw^2(\epsilon z + R) + 2iRz)}{w\sqrt{z(2kw^2 + 4ikz)}}\right) - \\
& \left. (1+i)\sqrt{\pi z} \epsilon k w \operatorname{erfi}\left(\frac{(1+i)\epsilon k w \sqrt{z}}{2\sqrt{kw^2 + 2iz}}\right) \right].
\end{aligned} \tag{3.37}$$

To illustrate the complex behavior of this Eq. 3.37 and the resulting intensity variation along z dependent on the apodization, the corresponding normalized intensity is plotted in Fig. 3.2 for different truncation ratios w/R . Here, a shift of the peak intensity dependent on this ratio is observed. The larger this ratio, the further the intensity is shifted towards larger z . In addition, the observed intensity is modulated, which is also in contrast to Eq. 2.21. The reason for the fluctuation is that the shown Bessel beams are non-ideal due to their finite truncation at $\rho_p = R$, leading to observable edge diffraction-phenomena, which in case of Bessel beams are projected onto the z -axis. In case of $w/R = 2/3$, there is less intensity compared to the other cases at the boundary, resulting in the least amount modulation height. For $w/R = 100$, the amplitude distribution can be regarded as an approximation of a tophat beam which is characterized by a homogeneous illumination. At the boundary, the intensity is maximal in this set of examples, leading to the strongest

pronounced ripples. In case of the tophat beam, the intensity increases linearly with z [60]. The strong influence of the apodization on the on-axis intensity distri-

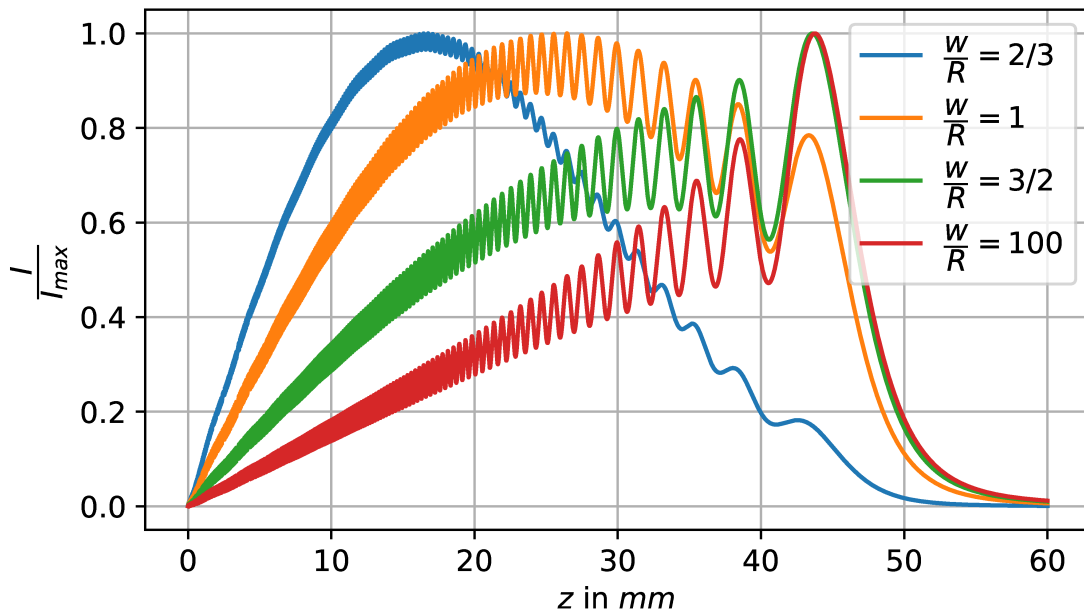


Figure 3.2.: Normalized on-axis intensities of Bessel-Gauss beams with different truncation ratios w/R with $R=1$ mm at $\lambda=500$ nm. The cone angle is defined by $NA = 0.02$.

bution can be understood by investigating the resulting integral within the method of stationary phase. The basic idea behind this method is briefly introduced in the following.

3.3.2. Method of stationary phase

Detailed formulations of the stationary phase approach in the context of optics are found in [31, 33]. Typical expressions for describing the propagation of light as an electro magnetic wave (e.g., Eq. 2.14 and 2.17) are of the form

$$U = \iint_{-\infty}^{+\infty} f(u, v) e^{ikg(u, v)} du dv, \quad (3.38)$$

where k is assumed to be large. Hence, the exponential function is strongly oscillating and goes rapidly through cycles of 2π . If the amplitude function $f(u, v)$ is assumed to be smooth and slowly varying, it is clear that adjacent half-cycles cancel

each other. Only in a small vicinity of a stationary point, the oscillations slow down and no cancellation occurs. This is visualized in Fig. 3.3 by plotting the real part of an oscillating kernel with a quadratic phase and the corresponding integrals for increasing values of k .

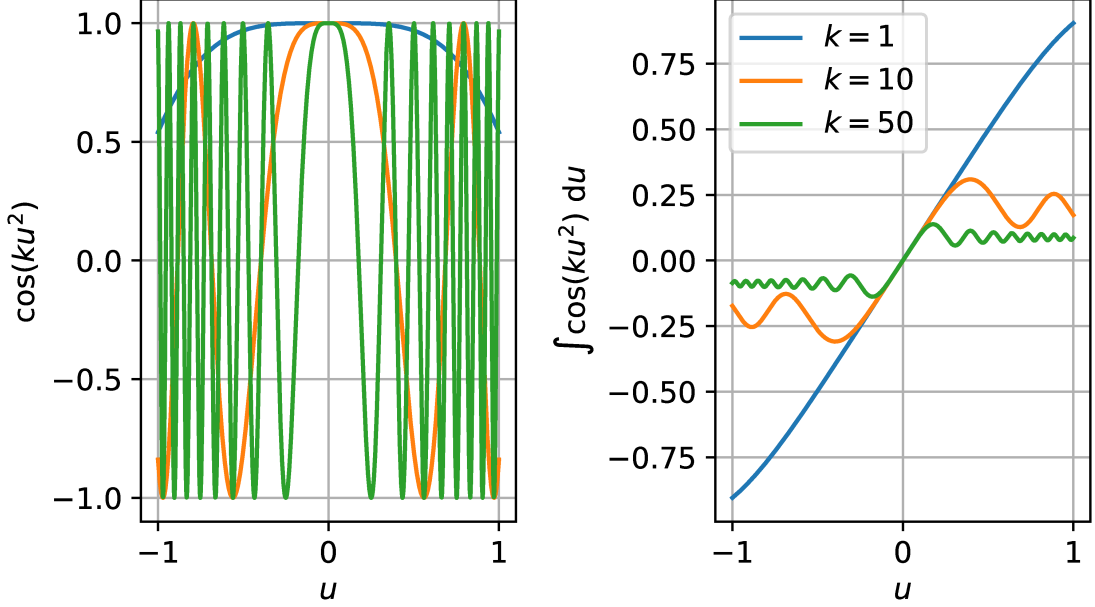


Figure 3.3.: Plot of $\cos(ku^2)$ and the corresponding integrals for different values of k around the stationary point at $u_0 = 0$ to illustrate the idea behind the method of stationary phase.

The value of the integral over the full domain is mainly determined by the integral over a patch around the stationary point (u_0, v_0) . To evaluate this patch, $g(u, v)$ is expressed by its Taylor series up to the second order term

$$g(u, v) \approx g(u_0, v_0) + \frac{1}{2} (g_{uu}s^2 + g_{vv}t^2 + 2g_{uv}st), \quad (3.39)$$

$$s = u - u_0, \quad (3.40)$$

$$t = v - v_0. \quad (3.41)$$

The slowly varying amplitude is treated as constant around the stationary point. Hence, it is taken out of the integration

$$U = f(u_0, v_0) e^{ikg(u_0, v_0)} \iint_{-\infty}^{+\infty} e^{\frac{1}{2}ik(g_{uu}s^2 + g_{vv}t^2 + 2g_{uv}st)} ds dt. \quad (3.42)$$

The mixed terms of the derivatives can be set to zero by rotating the coordinate system and the argument of the exponential function can be written as $\frac{1}{2}ik(\alpha s'^2 + \beta t'^2)$, where α and β are the eigenvalues of the matrix

$$H = \begin{pmatrix} g_{uu} & g_{uv} \\ g_{uv} & g_{vv} \end{pmatrix}. \quad (3.43)$$

Then, U can be expressed by two separated standard integrals

$$U = f(u_0, v_0)e^{ikg(u_0, v_0)} \int_{-\infty}^{+\infty} e^{\frac{1}{2}ik\alpha s'^2} ds' \int_{-\infty}^{+\infty} e^{\frac{1}{2}ik\beta t'^2} dt', \quad (3.44)$$

that can be solved with the identity $\int_{-\infty}^{+\infty} e^{\pm ix^2} dx = e^{\pm \frac{\pi}{4}i}$, yielding

$$U = \frac{2\pi}{k\sqrt{|H|}} e^{\frac{\pi}{4}i(\sigma_u + \sigma_v)} f(u_0, v_0) e^{ikg(u_0, v_0)}. \quad (3.45)$$

Here, the determinant of the Hessian matrix is $|H|$ and the sign of the second derivatives is taken into account by $\sigma_u = \text{sign}(g_{uu})$, $\sigma_v = \text{sign}(g_{vv})$. Consequently, the integral for the value U is solved approximately, becoming more and more accurate for increasing k and stronger curvatures of $g(u_0, v_0)$. In case of a rotational symmetric quasi Bessel beam a stationary point is transformed to a stationary ring. Thus, a small ring element with amplitude $f(\rho_0)$ accounts for a small on-axis line element. The higher the NA , the narrower is the contributing ring width and the better the stationary phase approximation. According to Eq. 3.45, the amplitude of a ring element is directly proportional to the corresponding on-axis amplitude of the field, which shows the strong dependence of the focussed line profile on the apodization function. In chapter. 5 the idea of the stationary phase approximation is used to calculate the impact of spherical aberration up to arbitrary order beside astigmatism and coma on the line focus of Bessel-Gauss beams to evaluate their performance analytically. This is further used to compute an extended z -dependent Strehl-ratio definition in case of the generated line focus.

3.3.3. Profiling of the on-axis intensity

Another explanation for the apodization dependent on-axis intensity is given in [48] for rotational symmetric fields in terms of Hankel and Fourier transforms. This

description is very useful to obtain arbitrary shaped on-axis fields, in particular. The basic ideas are briefly introduced.

The spatial spectrum of a field can be calculated by Eq. 2.11. In case of a rotational symmetric field with $k_\rho = \sqrt{k_x^2 + k_y^2}$, this can be written as a zero-order Hankel-transform

$$S(k_\rho, z = 0) = \int_0^\infty E(\rho, z = 0) J_0(k_\rho \rho) \rho d\rho \quad (3.46)$$

and the corresponding inverse Hankel transform

$$E(\rho, z = 0) = \int_0^\infty S(k_\rho, z = 0) J_0(k_\rho \rho) k_\rho dk_\rho. \quad (3.47)$$

The physical interpretation of this relation is that an rotational symmetric field can be decomposed into a set of ideal zero order Bessel beams. According to Eq. 2.18 and 2.21 each of these individual Bessel beams propagates in free space according to $J_0(k_\rho \rho) e^{ik_z z}$. Each Bessel mode has a specific spatial frequency along the optical axis which contributes to the on-axis field. By combining the propagation properties of the individual Bessel modes and Eq. 3.47, the on-axis field can be computed by

$$E(r = 0, z) = \int_0^k S\left(\sqrt{k^2 - k_z^2}, z = 0\right) e^{ik_z z} k_z dk_z. \quad (3.48)$$

This formula connects the on-axis field with the spatial spectrum of the initial field by a one-dimensional Fourier transform. Thus, arbitrary field distributions along z can be generated with the available frequency range. The simulation and measurement of three different beams are shown in Fig. 3.4 to illustrate the application of Eq. 3.48. These depictions are published in [48]. In the top row the intensity is invariant over the main length of the generated beam. The center and bottom row display the results for a linearly changing intensity along z . Only the boundary regions are influenced by an unwanted variation along z with a smooth transition. This transition is controlled via a Gaussian envelope function that also suppresses the on-axis fluctuations as shown in Fig. 3.2. A narrow envelope damps the oscillation, but at the same time it smooths the transition. Thus, an application dependent trade-off solution between desired on-axis uniformity and uniformity length must be found.

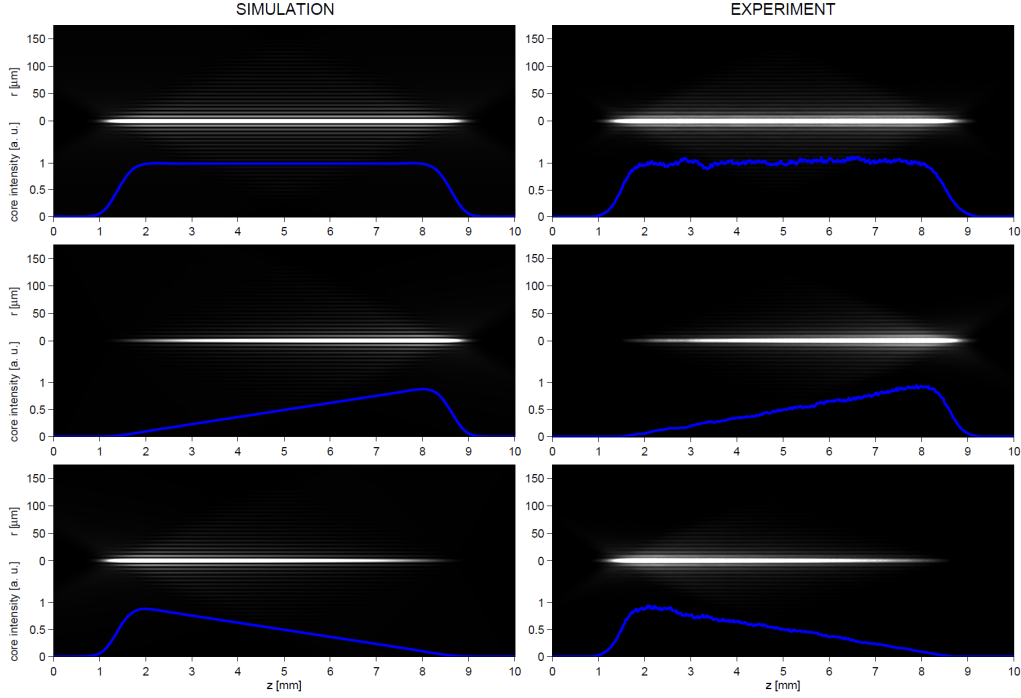


Figure 3.4.: Variety of quasi Bessel beams calculated by Eq. 3.48 and experimentally measured [48]. The top row shows the results of an uniform intensity along z , while the center and bottom row show the results of a linear increasing and decreasing on-axis intensity, respectively.

3.4. Homogeneous thermal load in optical systems

In this section, the state-of-the-art ideas to consider homogeneous temperature variations of refractive optical systems including the mountings are presented [22, 24, 38, 49]. This is especially important for applications in temperature unstable environments such as cameras or lidar (light detection and ranging) systems in the automotive industry for the purpose of autonomous driving [61–63]. The shown considerations are addressing the paraxial properties of the system by paraxial ray trace data, since they typically show the strongest temperature dependence and allow for an analytic treatment. This enables to derivation of a fundamental understanding and physical relations, which are of great benefit to find initial systems and allowing the athermalization of basic properties of optical systems. In general, the homogeneous temperature change of a paraxial optical system leads to defocus. Non-paraxial systems with comparably larger ray angles consequently suffer from

higher order aberrations [22, 39, 64]. Higher sophisticated systems or systems in a later design and simulations phase typically require complex modeling approaches like the connection of ray-tracing with finite-element-methods in order to represent the boundary conditions accurately. This leads to a significant increase of the computational effort [21, 22, 26, 27]. These higher order effects are not adressed within the scope of this thesis.

3.4.1. Heated thin lens singlet

To demonstrate the defocus effect in case of a uniform temperature change inside a paraxial thin lens, the following formula for the focal power F is investigated [29, 38]

$$F = (n - 1) \left(\frac{1}{R_1} - \frac{1}{R_2} \right), \quad (3.49)$$

with the radii of curvature R_1 and R_2 on the front and rear surface of the lens, respectively. For simplicity the refractive index of air is assumed to be constant one. Taking the derivative with respect to the temperature T yields [24]

$$\frac{\partial F}{\partial T} = \frac{\partial n}{\partial T} \left(\frac{1}{R_1} - \frac{1}{R_2} \right) - (n - 1) \left(\frac{1}{R_1^2} \frac{\partial R_1}{\partial T} - \frac{1}{R_2^2} \frac{\partial R_2}{\partial T} \right). \quad (3.50)$$

In case of an isotropic expansion of the glass, the radii of curvature can be described in a linear model as

$$R'_i = R_i(1 + x_g \Delta T) \quad , i = 1, 2. \quad (3.51)$$

Together with the expansion coefficient of the glass $x_g = \frac{1}{R} \frac{\partial R}{\partial T}$, this leads to

$$\frac{\partial F}{\partial T} = F \left(\frac{1}{n - 1} \frac{\partial n}{\partial T} - x_g \right). \quad (3.52)$$

In terms of the focal length $f = 1/F$, this is formulated as

$$x_f = \frac{1}{f} \frac{\partial f}{\partial T} = x_g - \frac{1}{n - 1} \frac{\partial n}{\partial T}, \quad (3.53)$$

where x_f is called the opto-thermal expansion coefficient. It purely depends on the material parameters of the lens and is independent of the shape. The temperature

dependence of the refractive index can be given in various ways. The glass vendor Schott specifies it with the following definition [38]

$$\frac{dn}{dT} = \frac{n^2(\lambda) - 1}{2n(\lambda)} \left(D_0 + 2D_1\Delta T + 3D_2\Delta T^2 + \frac{E_0 + 2E_1\Delta T}{\lambda^2 - \lambda_{TK}^2} \right). \quad (3.54)$$

Here, n is the nominal refractive index at room temperature at a specified wavelength, D_0 , D_1 , D_2 , E_0 , E_1 and λ_{TK} are constants, found in the corresponding data sheets of the glasses. Thus, $\frac{\partial n}{\partial T}$ is not only dependent on the wavelength but also on the temperature itself. This has to be considered in situations where the temperature increases substantially. An overview of glasses from Schott with the corresponding properties can be found in Tab. A.2. Here, it can be seen that the absolute value as well as the sign of $\frac{\partial n}{\partial T}$ differs among the listed glasses but it is positive for the majority of glasses. For x_g only positive values can be found.

Similar to Eq. 3.51, the mounting of the lens is also expanding due to the change of temperature, which can be described by the thermal expansion coefficient of the mounting x_m . An overview of selected mounting materials with the corresponding properties is listed in Tab. A.3. Dependent on the sign of x_f , the focus position is shifted towards or away from the lens. With a combination of x_f and x_m , it is possible to compensate the thermally induced shift of the focus position by the expansion of the mounting material. Therefore, the optical system can be athermalized by an appropriate choice of the materials [24, 38, 49]. In practice, this is often critical due to the limited choice of mounting materials. Especially the compensation for negative x_f is an issue because there is no mounting material with a negative expansion coefficient. This problem is solved by splitting the lens into two lenses, which is discussed next.

3.4.2. Heated thin lens doublet

Optical systems often consist of two lenses in contact. The resulting focal length of such a system with two thin lenses is obtained by

$$\frac{1}{f} = \frac{1}{f_1} + \frac{1}{f_2}, \quad (3.55)$$

where f_1 and f_2 are the individual focal lengths of the lenses. The resulting optothermal expansion coefficient is expressed as [21, 24]

$$x_f = \frac{f}{f_1}x_{f_1} + \frac{f}{f_2}x_{f_2}. \quad (3.56)$$

The thermal and chromatic properties of the doublet can be maintained by

$$x_f = \frac{\nu_1 x_{f_1} - \nu_2 x_{f_2}}{\nu_1 - \nu_2}, \quad (3.57)$$

where ν is the Abbe-number of the respective glasses. The Abbe-number is used to characterize the chromatic dependence of the refractive index (dispersion) in terms of the normalized inverse slope at specified wavelengths. Thus, small values of ν correspond to large changes of the refractive index with the wavelength and large values of ν indicate glasses with low dispersion [38, 49]. The thermal compensation with a doublet is more flexible than the singlet approach, since x_f can be tuned by the combination of two materials. In practice, there are more available glasses than mounting materials. Thus, choosing a mounting material first and then combining two glasses to achieve $x_m = x_f$ is a possible athermalization strategy [24]. Additionally, two lenses offer more degrees of freedom for the correction of other aberrations like axial color, spherical aberration, field curvature and coma [38, 49, 64], which is discussed in literature in the scope of achromates.

In practice, often non-uniform temperature variations occur. Such scenarios might be space applications where the sun is heating the optical system from one side or high power laser systems where the laser light is absorbed inside the lenses due to bulk absorption. Within this thesis, the second case is further investigated in chapter 6 by calculating the temperature inside a thin lens that is illuminated and heated by a high power fundamental Gaussian beam. The resulting temperature distribution is further used to derive an expression of the additional heat induced focal power based on the paraxial raytrace inside a gradient index medium (GRIN). Furthermore, this is applied in the athermalization of basic optical systems for shaping laser beams like doublets and telescopes.

4. Coherent laser beam reconstruction and characterization by non-iterative phase retrieval solving the TIE

The characterization of real laser beams is an important task for a variety of applications where the difference between designed and real beams has to be investigated or different beams are compared to each other. As a standard technique for the analysis of laser beams, the beam performance is quantified by the M^2 parameter, which is described in section 3.2. The M^2 -value exploits the similarity to a fundamental Gaussian beam. The most important reasons for deviations from the ideal value of M^2 being one are phase aberrations, amplitude variations or a certain degree of partial coherence. A separation of these three quantities cannot be performed by calculating the scalar measure of M^2 [14], which is a fundamental disadvantage of this methodology. Within the scope of this chapter, only fully coherent beams are considered. In applications where the laser beams are profiled by beam shaping optics, the M^2 -value is not helpful, since it is only invariant in paraxial optical systems, where occurring aberrations are not included. Thus, the variation of phase and amplitude are not considered sufficiently enough to predict the performance of real laser beams. To extend the quality-metric beyond the M^2 of a coherent beam, the phase and amplitude distributions must be analyzed. While the intensity can be simply measured by a camera, the phase cannot. Measuring the phase usually requires interferometric techniques or wavefront sensors for example Hartmann-Shack sensors.

The challenge of the simultaneous measurement of amplitude and phase can be resolved by the method of phase retrieval. The great interest in the this topic

is unbroken from the past up to recent time for a multitude of applications. In literature, several methods to tackle this inverse problem are described. Many of them are based on the inverse-Fourier-transform-algorithm (IFTA) principle [65,66]. They are often applied in the field of beam shaping with arbitrary phase-functions. For the characterization of optical systems, there are specialized algorithms that are based on the optimization of a parametrized physical model or the extended Nijboer-Zernike theory [67,68]. Another field of algorithms, which tackle the phase-retrieval problem, are based on solving the transport of intensity equation (TIE) [34], which was introduced in the realm of the paraxial wave equation in section 2.2. The TIE is solved for many different applications ranging from the field of surface testing to phase-imaging in microscopy [46,69,70].

The TIE is a partial-differential equation, that connects the variation of the intensity distribution with the phase distribution for a coherent field. Therefore, it allows for a simple experimental setup for quantitative phase measurements consisting of a shiftable camera to acquire the intensity distribution in space. In literature, there are many distinct methods for the solution of the TIE proposed, which are typically problem-specific. In the original work of Teague, the solution via a Green's function and direct numerical integration was proposed [34]. This idea corresponds to a solution of the TIE for each individual pixel of the measured intensity points. The most typical method to solve the TIE is found by transforming it into two subsequent Poisson equations and solving these in the frequency domain [35,46]. Gureyev et al. solved the TIE via certain sets of basis functions like Zernike-polynomials or Fourier-harmonics [36,37].

In this chapter a laser beam specific solution scheme of the TIE is proposed. Therefore, the chapter is structured as follows. In section 4.1, the most common approach to solve the TIE is shown and the issues arising in the special case of laser beams are described. After that, a new laser beam specific methodology based on a phase decomposition is introduced and critical parameters are analyzed. Here, the basic idea is the decomposition of the phase into paraxial terms known from Gaussian beams such as tilt and curvature, and a set of shifted radial-basis-functions (RBFs) which are used to describe higher order phase terms. The RBFs are useful due to their local support making them flexible in describing symmetry-free surfaces [71] and their simple differentiation scheme. This decomposition is directly inserted into the TIE yielding a system of linear equations which has to be solved for the corresponding

coefficients of the RBFs. In section 4.2 the method is tested against synthetic data to derive the accuracy of the retrieved wavefront based on the comparison of measured and reconstructed intensity stacks. After that, a simple experimental setup is described and two laser beams with different divergence angles are evaluated to validate the new TIE approach based on real experimental data.

Parts of this chapter are published in [72].

4.1. Solution of the TIE

4.1.1. Classical solution

In literature, the probably most common method to solve the TIE is based on transforming the TIE into two subsequent Poisson equations [34,35]. Therefore, the TIE (Eq. 2.42) is reformulated as

$$-k \frac{\partial I}{\partial z} = \nabla_{\perp} \cdot (I \nabla_{\perp} \Phi) \quad (4.1)$$

$$= \nabla_{\perp}^2 \Psi, \quad (4.2)$$

with the auxiliary function $\nabla_{\perp} \Psi = I \nabla_{\perp} \Phi$. Thus, the first Poisson equation, Eq. 4.2, can be solved for Ψ by formulating this in the spatial frequency domain with (f_x, f_y) leading to a linear filter operation

$$\Psi(f_x, f_y) = \frac{\mathcal{F}\{-k \frac{\partial I}{\partial z}\}}{-4\pi^2(f_x^2 + f_y^2)}. \quad (4.3)$$

To obtain the phase from the auxiliary function, a second Poisson equation needs to be solved

$$\nabla_{\perp}^2 \Phi = \nabla_{\perp} \frac{\nabla_{\perp} \Psi}{I} \quad (4.4)$$

The solution can be obtained in the same way as for the first Poisson equation by a linear filter operation. This procedure offers a simple and elegant scheme for many applications, especially in the field of phase imaging [35,69,73]. Though, from Eq. 4.4 it can be seen that a division by the intensity itself occurs. This is not an

issue when a phase probe is illuminated nearly homogeneously, but in the scope of the reconstruction of laser beams this certainly is numerically problematic. Here, often patterns with zero intensity occur due to diffraction effects and aberrations, which would require a special regularization scheme for the solution of Eq. 4.4. To avoid these intricacies, a new scheme incorporating the paraxial properties of coherent laser beams is developed and exploited next.

4.1.2. Specific solution for laser beams

To find a solution of the TIE in the context of coherent laser beams, it is proposed to decompose the phase into basic terms describing the paraxial properties of the beam and higher order terms describing the phase perturbations. The paraxial properties of the beam are the tilt Φ_t and the curvature of the phase Φ_c . They are described by lower order polynomials. For the description of the higher order phase terms Φ_{RBF} a set of RBFs is used

$$\Phi = \Phi_t + \Phi_c + \Phi_{RBF}. \quad (4.5)$$

Here, the tilt of the phase is defined as

$$\Phi_t = k(t_x x + t_y y) \quad (4.6)$$

with the corresponding coefficients t_x, t_y . The curvature of the phase is specified by the coefficient c and the corresponding definition

$$\Phi_c = \frac{kc}{2}(x^2 + y^2), \quad (4.7)$$

assuming the dominant contribution is circular symmetric. These two quantities are similar to the basic properties of Gaussian beams whose propagation direction is perpendicular to the linear phase and the shape of the phase is parabolic. The higher order phase-terms are described the following linear combination of M RBFs

$$\Phi_{RBF} = \sum_{m=1}^M c_m e^{-\epsilon^2((x-x_m)^2+(y-y_m)^2)}. \quad (4.8)$$

In this work, the RBFs are chosen to be a set of Gaussian functions with the shape-factor ϵ that represents the inverse width of the individual Gaussian functions. To

improve the readability for the next considerations, the following is defined

$$\nabla I = \begin{pmatrix} I_x \\ I_y \\ I_z \end{pmatrix}, \quad \nabla_{\perp} I = \begin{pmatrix} I_x \\ I_y \end{pmatrix}, \quad \nabla_{\perp} \phi = \begin{pmatrix} \phi_x \\ \phi_y \end{pmatrix}. \quad (4.9)$$

When Eq. 4.5-4.8 are inserted into Eq. 2.42, one can separate the terms of tilt, curvature and higher order for I_z according to the respective parts of Φ

$$-kI_z = -k(I_{z,t} + I_{z,c} + I_{z,RBF}), \quad (4.10)$$

$$-kI_{z,t} = k(I_x t_x + I_y t_y), \quad (4.11)$$

$$-kI_{z,c} = kc(I_x x + I_y y + 2I), \quad (4.12)$$

$$\begin{aligned} -kI_{z,RBF} &= \sum_{m=1}^M c_m e^{-\epsilon^2((x-x_m)^2+(y-y_m)^2)}. \\ &2\epsilon^2 \left[I_x(x_m - x) + I_y(y_m - y) + \right. \\ &\left. I(2\epsilon^2(x_m - x)^2 - 1) + I(2\epsilon^2(y_m - y)^2 - 1) \right]. \end{aligned} \quad (4.13)$$

For fundamental Gaussian-like laser beams, the dominant terms of the phase are the tilt and the curvature. The tilt-coefficients can be simply identified by computing the centroid of the beam along z , which lies on a straight line. The curvature of the phase in the plane of consideration can be determined by minimizing the expression

$$|I_z + c(I_x x + I_y y + 2I)|^2 = \min. \quad (4.14)$$

Hence, the dominating phase terms for tilt and curvature are calculated separately from the higher order terms and Eq. 4.10 can be rearranged with the known parts on the left-hand-side and the unknown part on the right-hand-side

$$-k(I_z + I_{z,t} + I_{z,c}) = -kI_{z,RBF}. \quad (4.15)$$

To calculate the phase, the linear system of equations formed by Eq. 4.13 and 4.15 with the unknown Gaussian coefficients is solved by a least-squares-fit. The resulting coefficients c_m for the higher order phase-terms are then inserted into Eq. 4.8 to gain the final phase function.

The RBFs can be located by a various number of sampling schemes, e.g., Cartesian,

polar or Fibonacci. In this work, a Fibonacci sampling scheme is chosen. It typically provides a significant better performance in comparison to other sampling schemes [71]. The size of the individual RBFs is controlled by their shape-factor ϵ . For sake of simplicity, all RBFs have the same shape. This shape factor is of particular importance for the reconstruction of the phase, since it controls the local gradient of the phase at a given sampling. To account for an optimal choice of ϵ for fixed sampling conditions of the RBFs, an analog procedure as described in [71] is applied.

4.1.3. Critical parameters

The critical parameters for the phase retrieval procedure with the described set of equations are the noise within the intensity measurements, the corresponding calculation of the gradient of the intensity and the region of interest, where the phase is reconstructed.

The noise in the intensity acquisition is presumed to be induced by white noise and quantization-errors due to the limited bit-depth of the available cameras, mainly. Both issues are resolved by recording the images at one position with varying exposure times. The resulting intensity-stack is then merged to a high-dynamic-range (HDR) image [74, 75]. The HDR image provides an overall enhanced signal-to-noise ratio and even provides signal in regions, where conventionally no or only saturated signals can be measured due to under- or over-exposure, respectively.

The gradient of the intensity is computed based on the actual intensity data. Thus, it is also influenced by noise and its accuracy can be improved by reducing the noise with the HDR-technique. An additional point for the calculation of the correct gradient is the sampling in axial and lateral direction. In principle, the distance Δz between subsequent measurement planes can be chosen arbitrarily small being only limited by the step size of the used stage. Therefore, the accuracy can be arbitrary large along z for an ideal noise-free signal. If noise is considered, Δz must be chosen carefully, since small distances lead to a small signal change $I(z_2) - I(z_1)$, which may be perturbed by noise. Thus, the signal-change is dominated by noise. If Δz is too large, the signal change is larger than the noise, but may exceed the range, where a finite difference approximation of the corresponding axial derivative is valid. Hence, the optimal distance is dependent on the signal change and the noise [76, 77]. This was investigated theoretically by Teague in [34] where he gave expressions for

an optical choice of Δz for estimated noise and phase values. Waller et al. showed similar findings by examining errors of noisy signal derivatives dependent on the finite difference order, Δz and varied noise-levels [35]. The lateral derivatives of the intensity are affected in the same manner as the axial derivative computations, but the difference is, that the separation between data points is fixed by the sensors pixel pitch. The only possibility to modify sampling condition is to enlarge the lateral extend of I by magnifying the beam with an appropriate telescope or by moving to different axial position for the reconstruction z_0 . For the calculation of ∇I a Savitzky-Golay-filter is used in this work [78]. This technique was already investigated in relation with the TIE in [77]. Basically, the filter fits a (typically low order) polynomial to the data points for smoothing the data and calculating the corresponding derivatives analytically. It can be controlled by the window-size and the polynomial order. A large window in combination with a small polynomial order correlates with a strong smoothing. Another practical important point is the position z_0 , where the phase is retrieved, because this has a strong impact on I_z . For an ideal fundamental Gaussian beam, the axial intensity is symmetrical around the focus (see section 2.2.1) and I_z is consequently exactly zero at the focus. Reconsidering the influence of the noise on the computation of I_z , it is clear, that the signal-change is strongly affected by noise at the focus. To maximize the signal value along z , an optimal position z_0 is computed. This position is found by the evaluation of the intensity-weighted root-mean-square (rms_w) value of I_z along z and selecting the position where this is maximal.

$$\text{rms}_w(I_z(z)) = \sqrt{\frac{\int I_z(x, y, z)^2 \cdot I(x, y, z) dx dy}{\int I(x, y, z) dx dy}}. \quad (4.16)$$

The region of interest where the phase is retrieved depends on the demands of the application. For example in the case of phase imaging, the phase values might not be of interest in the full illumination area. In the scenario of the characterization of Gaussian like laser beams with considerably large perturbations, the practical limit of detectable intensity defines the size of the region of reconstruction. This is reasonable due to the basic principle, that the phase is undefined if there is no intensity [30]. For further purposes of propagation of the calculated field, the phase must be retrieved for all points of measured intensity. Otherwise, the propagation of the reconstructed field is inaccurate and edge-diffraction effects might occur in the simulation, even if there is no physical edge in the measured data.

4.2. Results and discussion

4.2.1. Estimated accuracy of the retrieved phase

The assessment of the accuracy of the retrieved phase is a fundamental aspect in the quantitative characterization of coherent fields. To substitute wavefront measuring equipment like interferometers or Hartmann-Shack sensors completely, a consistency check of the reconstructed field with the measured stack of intensities is performed. Therefore, the reconstructed field is propagated to the planes of measured intensities and the corresponding intensities of the reconstructed field are compared with the measured ones. If the retrieved phase is identical to the real phase, the difference in intensities must be zero. Thus, in case of a mismatch between the reconstructed phase and the phase of the measured laser beam, this can be observed due to propagation, resulting in intensity differences between the measured and the reconstructed beam.

The basic idea of the following approach is to quantify the intensity differences and correlate this to the corresponding phase mismatch. This is done by simulating different Gaussian-like beams, whose ideal phase terms are disturbed by varied amplitudes of spherical aberration and astigmatism. Furthermore, the far field divergence angle θ (see Eq. 2.35) is varied to account for a broad spectrum of possible beam variations. The synthetic beams are then propagated into the focal region and the phase is retrieved by the proposed decomposition method to solve the TIE in a next step. The accuracy of the retrieved phase can be controlled by the number, shape and distribution of the used RBFs. A more detailed description of the dependencies can be found in [71], where they are used to describe the difference between ideal and manufactured freeform surfaces. The accuracy is quantified in terms of the weighted rms difference between the ideal and the retrieved phase $\text{rms}_w(\Delta\Phi)$. In order to normalize the results and make them independent on the focusing of the beam, the axial length is scaled in Rayleigh-lengths in air

$$z_R = \frac{\lambda}{\pi\theta^2}. \quad (4.17)$$

Its physical interpretation was already given in the scope of fundamental Gaussian beams in section 2.2.1. The intensities are compared within an interval of $\pm 1z_R$ by the calculation of the intensity weighted rms difference $\text{rms}_w(\Delta I)$.

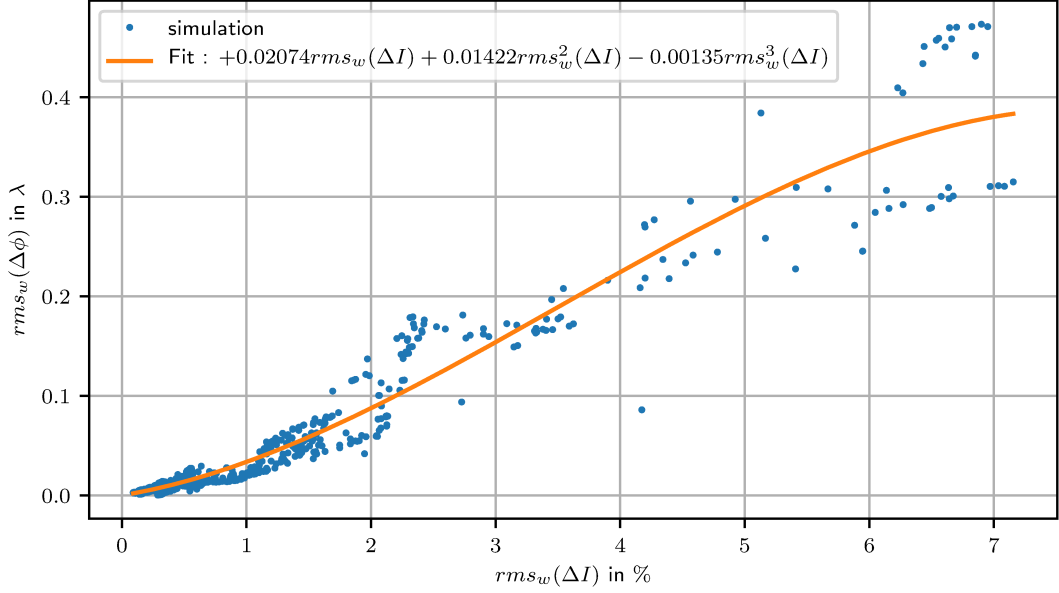


Figure 4.1.: Accuracy of the reconstructed wavefront in relation to the error of the reconstructed intensity stack within $\pm 1z_R$. The data-points contain the results of different amplitudes of spherical aberration and astigmatism, as well as different far field divergence angles.

The results of this investigation are plotted in Fig. 4.1. As expected, the accuracy of the retrieved phase strongly correlates with the observable differences of the intensities. The achieved match of the retrieved and original phase increases with increasing similarity of intensities. Consequently, larger values of $\text{rms}_w(\Delta I)$ correspond to enlarged values of $\text{rms}_w(\Delta\phi)$, but simultaneously its spreading is also increased. Thus, the uncertainty increases with increasing error value. To specify the correlation between the accuracy of the phase and the obtained intensity differences a third order polynomial is fitted to the data points, which is also plotted in Fig. 4.1. The corresponding coefficients are written in the legend. The fit is dominated by the linear and quadratic orders and matches the data points well in particular for low phase differences.

This description allows to quantify the results of real measured laser beams without the need of additional wavefront equipment. Hence, only the pure intensity data that have to be acquired anyways, are used. This assessment forms the basis for interpreting the results of experimental data in the following considerations.

4.2.2. Verification with experimental data

Experimental setup

The experimental setup used to acquire the intensity distribution consists of the light source and a camera mounted onto a linear stage. Within this consideration, the light source itself consists of the actual fiber coupled laser source and subsequent optics to collimate and focus the outcoupled laser beam. This interpretation is especially reasonable because only paraxial data about the collimation and focusing optics are known from the respective data sheets. Hence, the real behavior of the laser beam from the source to the exit pupil of the focus lens cannot be modeled with the given data and only the output of the whole system is accessible. To illustrate this, a systematic sketch of the setup is shown in Fig. 4.2.

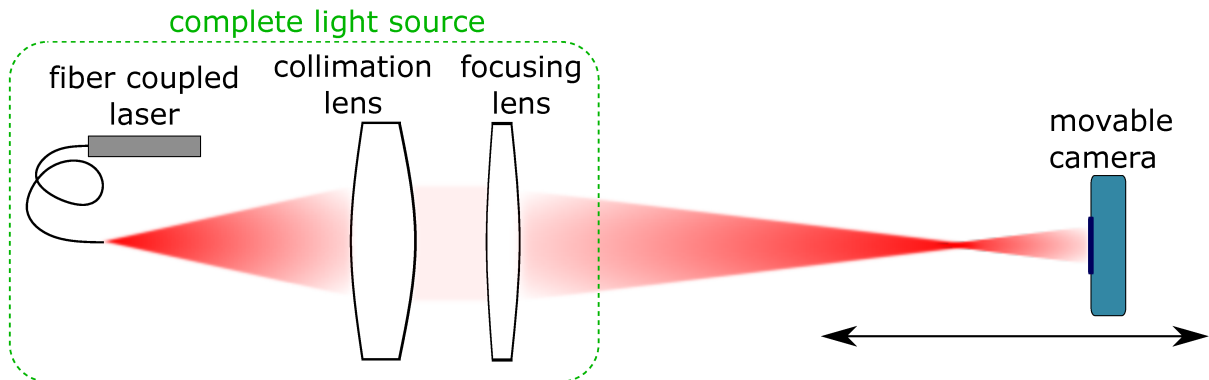


Figure 4.2.: Sketch of the experimental setup. According to the dotted box, the connection of laser, fiber and lenses is considered as an effective light source. Thus, the focusing lens can be considered as the output element of the complete light source.

The laser diode emits laser light with 1 mW of power at a wavelength of $\lambda = 663 \text{ nm}$ (Lambda Mini, RGB-Photonics GmbH, Kehlheim, Germany). The spectral width is specified with 0.7 nm at full width of half maximum, which is on the order of 1% of the emission wavelength. Since this is small, the spectral width is neglected in the further considerations. The emitted light is coupled into a single-mode fiber and afterwards transmitted through a collimator (60FC-4-M12-33). Then, the beam with a diameter of 2.16 mm is focused by an interchangeable focus module, which enables the easy adaptation of the light source to different focal lengths and focus diameters in a quasi plug-and-play manner. The collimation and focusing module are both from Schäfer+Kirchoff GmbH (Hamburg, Germany). In the following consideration

two different focus modules are used. The first focus module (5M-S325-33-S) has a focal length of 325 mm, resulting in a far field divergence of $\theta = 3$ mrad. With the second focus module a focal length of 150 mm (5M-S150-33-S) and a corresponding far field divergence of $\theta = 7$ mrad is achieved. Thus, the focus is expected to be approximately half of the size compared to the first focus module. To scan the intensity distribution along z , a dynamic stage is used (M-ILS300LM-S, Newport Corporation, Irvine, USA) and a beam profiling camera is mounted onto it (SP928, Ophir Spiricon Europe GmbH, Darmstadt, Germany). The camera captures 12 bit images with a resolution of 1928×1448 pixels. The pixel pitch is $3.69 \mu\text{m}$. Therefore, in case of ideal Gaussian beams the waist diameter is sampled in case of the first focus module by roughly 38 pixels and in case of the stronger focusing with the second module it is sampled by 16 pixels.

Laser beam with $\theta = 3$ mrad

For the retrieval of the phase, the intensities inside the region of interest with a radius of 0.49 mm around the centroid of the beam are considered. The phase is described by 3000 RBFs which are distributed within this region. To compute the axial derivative term I_z a sixth-order polynomial which is based on 51 planes along z and a separation of consecutive planes by 0.2 mm is used. The lateral derivative terms I_x, I_y are also computed by a sixth-order polynomial, though based on eleven intensity-values. Therefore, the smoothing effect is much stronger in axial direction, than in lateral direction.

The results of the reconstructed laser beam in the y - z cross-section are shown in Fig. 4.3 to provide an overview of the beams intensity. In the upper row, the measured intensity stack is shown and the corresponding intensities of the reconstructed field are shown in the center row. In the bottom plot, the on-axis intensities of the measurement and the reconstruction are presented. The intensity weighted rms difference of the intensities within $\pm 1z_R$ is $\text{rms}_w(\Delta I) = 1.23\%$. Comparing this with the results of Fig. 4.1, the accuracy of the retrieved wavefront is estimated to $\text{rms}_w(\Delta\phi) \approx 0.045\lambda$. In the plot of the on-axis intensity the asymmetric behavior around the peak intensity can be observed. On the left hand side, the intensity increases smoothly, whereas on the right hand side some small oscillations can be seen. Such asymmetric oscillations around the focus are typically caused by spherical

aberration [28].

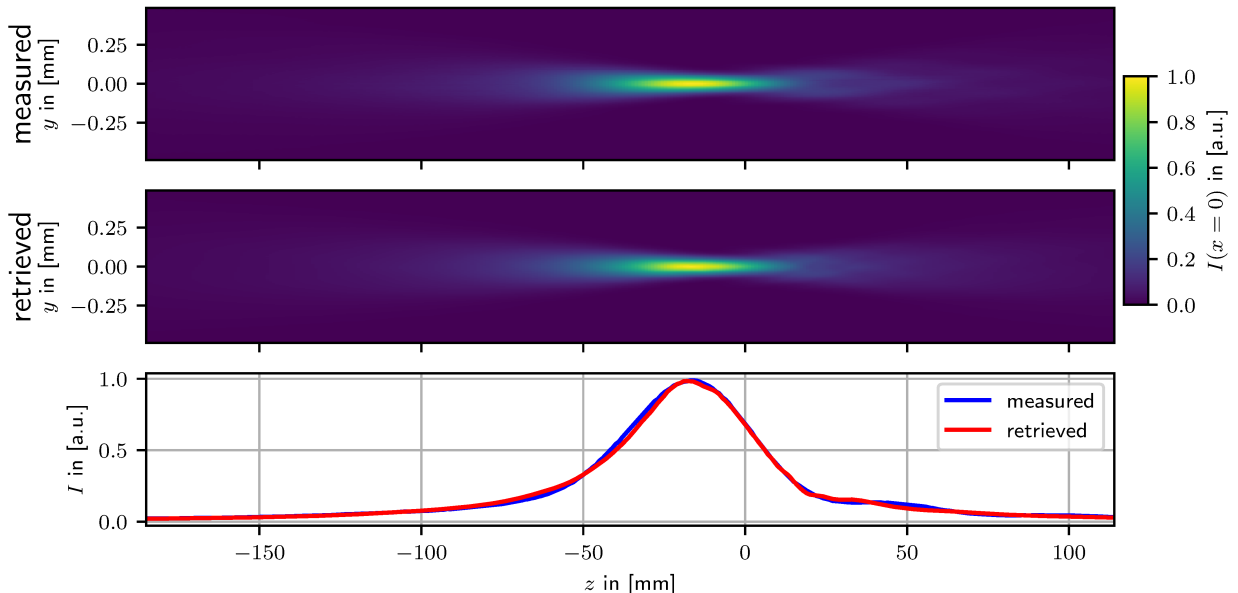


Figure 4.3.: Two-dimensional cross-sections $I(x = 0, y, z)$ of the measured and reconstructed intensities of the beam with $\theta = 3$ mrad. The intensity values are normalized to the global maximum. Below, the corresponding on-axis intensities $I(x = 0, y = 0, z)$ are plotted for comparison.

The intensity distributions in the x - y plane at distinct positions along z are shown in Fig. 4.4 to better illustrate the propagation behavior of the beam. Here, the measured intensities are in the top row and the intensities based on the reconstructed field are in the center row. The corresponding intensity differences are presented in the bottom row. The intensity differences are further quantified by the plotted weighted rms value for each plane. The comparison between the measured and the simulated stack shows a satisfying overall similarity, where the elliptical shape of the beam can be clearly identified especially at $z = -55$ mm and $z = 45$ mm, indicating astigmatism. However, the fine structure which can be seen best at $z = 45$ mm and $z = 95$ mm is not exactly reproduced. As already seen in Fig. 4.3, the fine structure is only observable on the right hand side of the focus.

To analyze the reconstructed field further, it is propagated back to the rear surface of the focusing lens. At this position, a Zernike decomposition of the phase is done to identify the dominant wavefront aberrations of the beam. In the experiment the distance between the reconstruction plane and rear surface of the lens is not exactly

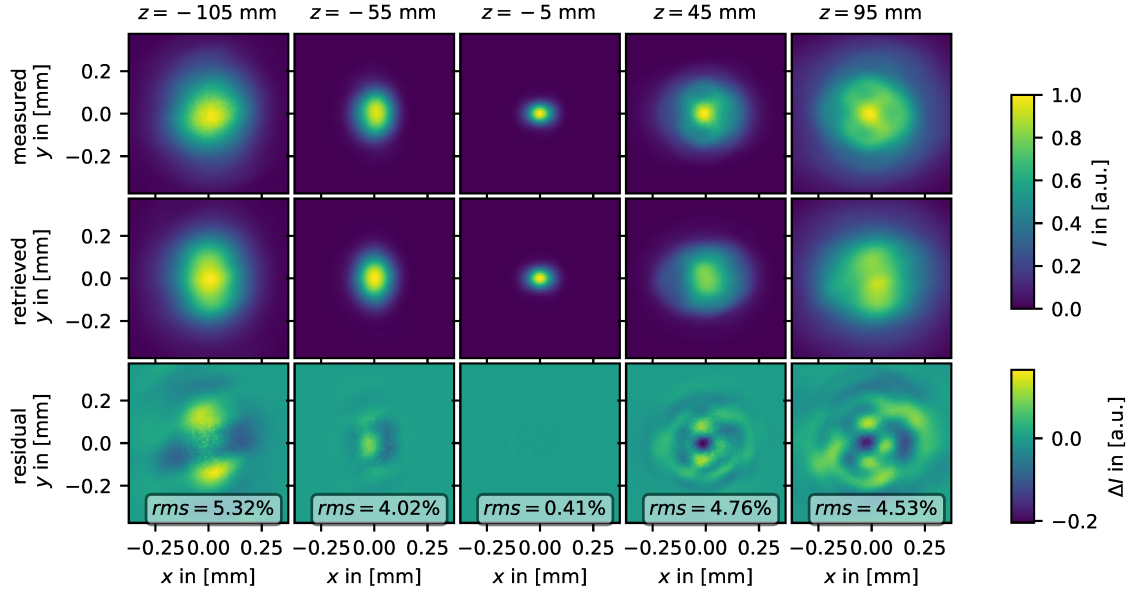


Figure 4.4.: Two-dimensional cross-sections of the measured and reconstructed intensities of the beam with $\theta = 3$ mrad at distinct positions along z . The intensity values are normalized for each plane individually. The intensity differences are shown below with the corresponding intensity-weighted rms errors.

known. However, the distance can be identified by propagating the field roughly by the amount of the focal length backwards and search for the position along z where the beam width matches the original beam diameter of 2.16 mm. The found distance is -361 mm. The normalization radius of the Zernike-polynomials is set to the clear aperture of the lens module which is specified with 2.5 mm. The results of the Zernike decomposition of the reconstructed and propagated field at the rear surface of the focusing lens are plotted in Fig. 4.5. The most dominant aberrations are astigmatism ($c_5 = -0.24\lambda$), followed by fourth order spherical aberration ($c_9 = 0.17\lambda$) and small amounts of coma ($c_7 = -0.10\lambda$). Higher order aberrations play only a minor role.

In the same plane the M^2 -value of the reconstructed field is calculated based on the spatial moments from the measured intensity and the angular moments from the phase as described in section 3.2.3. This calculation yields a value of $M^2 = 1.34$. To separate the impact of the phase and amplitude on the M^2 -value the phase is set to be plane. Thus, the obtained wavefront aberrations can be synthetically ignored. This results in a smaller value of $M^2 = 1.10$ for the purely amplitude perturbed beam.

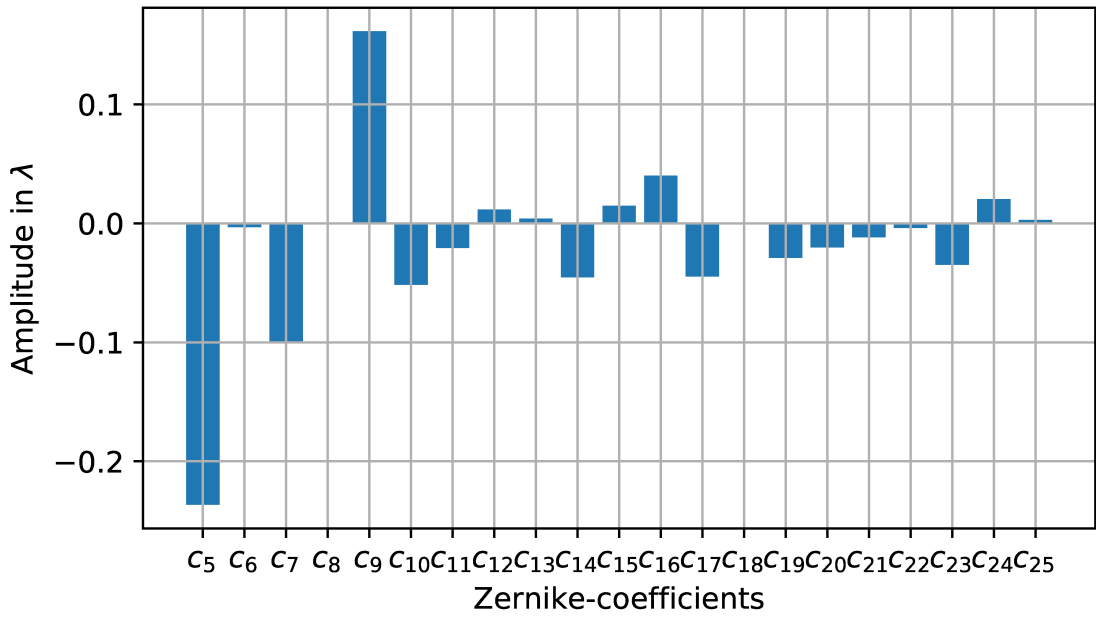


Figure 4.5.: Zernike decomposition of the wavefront of the $\theta = 3$ mrad laser beam at the rear surface of the focusing lens at $z = -361$ mm. The normalization radius is 2.5 mm.

Laser beam with $\theta = 7$ mrad

The parameters of the retrieval process for this laser beam are similar to the $\theta = 3$ mrad case. Only the region of interest, within the phase is retrieved, is adapted to 0.22 mm in order to account for the larger θ and the corresponding stronger focusing.

In Fig. 4.6, the results of the reconstruction are depicted in the y - z cross-section. The top and center row show the measured and computed intensities, respectively. In the bottom row, the comparison of the on-axis intensities is plotted. The accuracy of the retrieved phase is again estimated based on the findings that are given in Fig. 4.1. Within $\pm 1z_R$ the intensity difference is $\text{rms}_w(\Delta I) = 1.01\%$, which corresponds to an accuracy of the wavefront of $\text{rms}_w(\Delta\phi) \approx 0.034\lambda$. The intensity is clearly asymmetric around the peak intensity along z . In particular the right hand side of the focus shows lateral ring structures and axial oscillations, which similar to the previous measurement is an indicator for spherical aberration.

To allow for a better visual comparison of the results, the intensity distributions

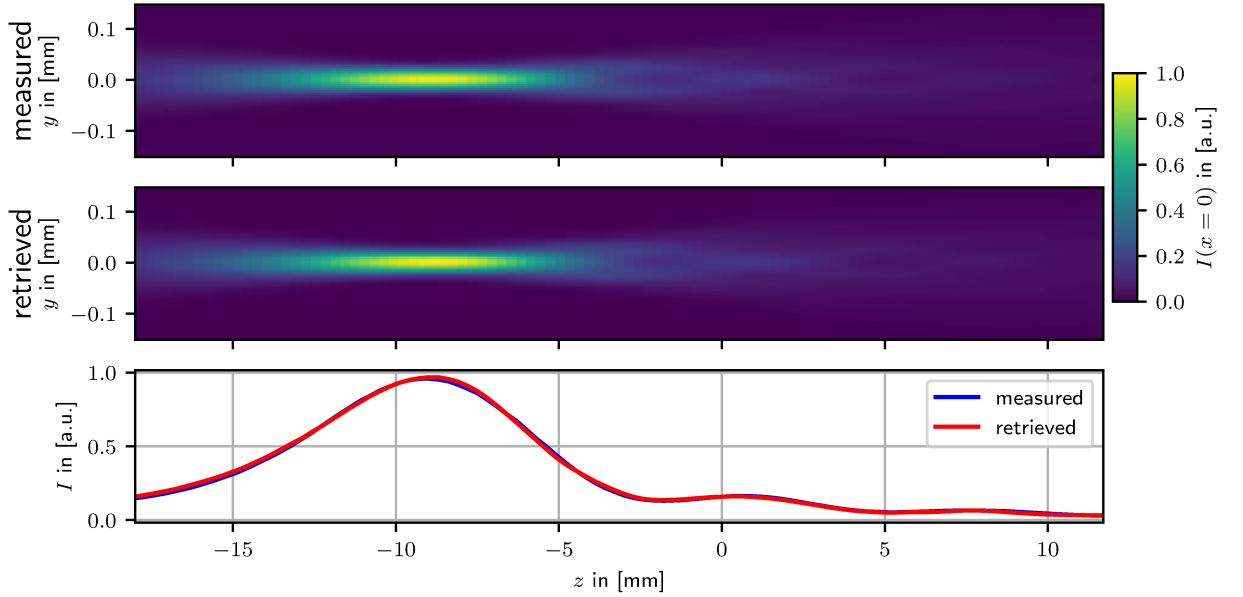


Figure 4.6.: Two-dimensional cross-sections $I(x = 0, y, z)$ of the measured and reconstructed intensities of the beam with $\theta = 7$ mrad. The intensity values are normalized to the global maximum. Below, the corresponding on-axis intensities $I(x = 0, y = 0, z)$ are plotted for comparison.

in the x - y plane at distinct positions along z are shown in Fig. 4.7. The measured and simulated intensities are given in the top and center row, respectively. Their mismatch is shown in the bottom row as an intensity difference. In addition, the intensity weighted rms value of the difference is plotted for each plane. The intensity distributions show a good agreement regarding the rough shape of the pattern as well as the fine structures of the rings on the right hand side of the focus. There are no visible rotational asymmetric contributions. Therefore, mainly spherical aberration is expected.

Similarly to the first measurement, the reconstructed field is further analyzed by propagating it back to the rear surface of the focusing lens and decomposing it into Zernike-polynomials. The exact propagation distance is found in the same way as for the first measurement. The result is -156 mm. Again, the normalization radius of the Zernike-polynomials is set to the clear aperture radius of the focus module, which is also 2.5 mm. The results of the investigation are plotted in Fig. 4.8. Here, the dominant contributions are spherical aberration of fourth order ($c_9 = 0.38\lambda$) and sixth order ($c_{16} = 0.13\lambda$). All other coefficients are smaller than $\pm 0.04\lambda$.

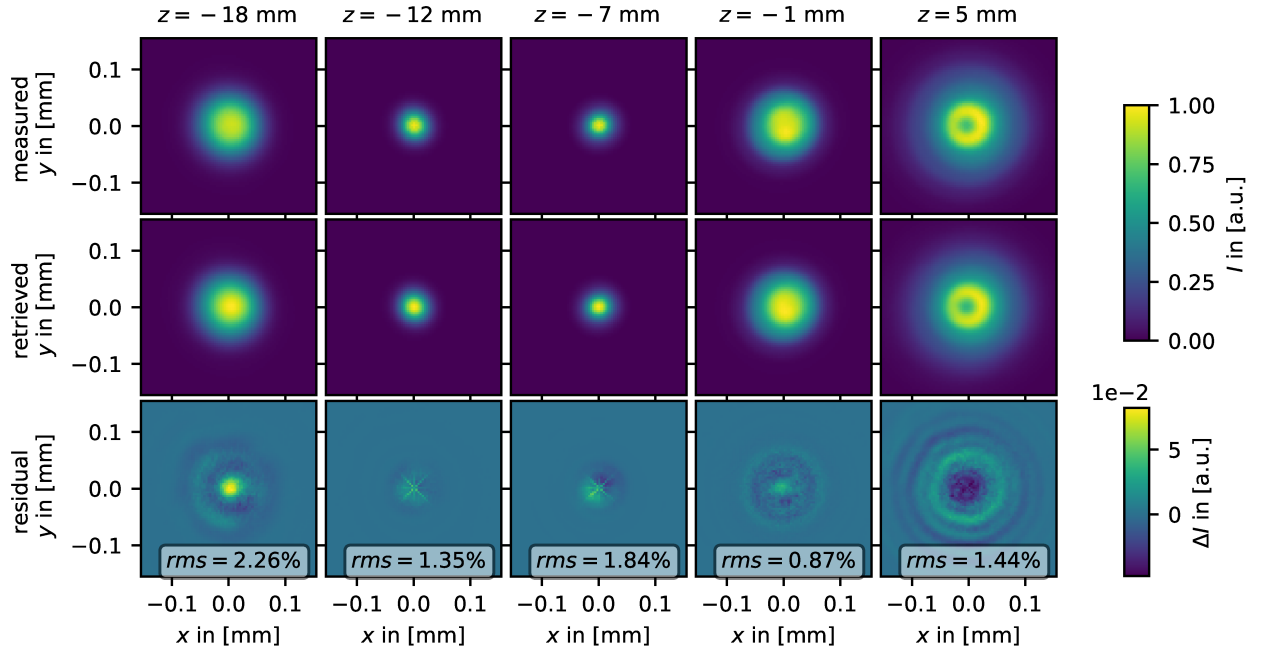


Figure 4.7.: Two-dimensional cross-sections of the measured and reconstructed intensities of the $\theta = 7$ mrad beam at distinct positions along z . The intensity values are normalized for each plane individually. The intensity differences are shown below with the corresponding intensity-weighted rms errors.

The corresponding M^2 -value is also computed in the rear plane of the focusing lens in the same manner as for the first measurement. For the reconstructed field it is $M^2 = 1.71$. To separate the impact of the amplitude from the phase, the phase is again set to a plane. The result of the purely amplitude dependent beam propagation factor is $M^2 = 1.05$.

4.2.3. Discussion

The difference between both experimental setups is the inserted focusing module, which in both cases is a singlet. From the perspective of aberration correction, the focus module with shorter focal length was expected to perform slightly worse, since the stronger focusing provokes larger angles in the ray-bending which is typically leading to an enhancement of spherical aberrations. These expectations are already satisfied by the visual inspection of the caustic. The asymmetric oscillations on the right hand side of the focus seen in the on-axis intensity plot of Fig. 4.3 and 4.6

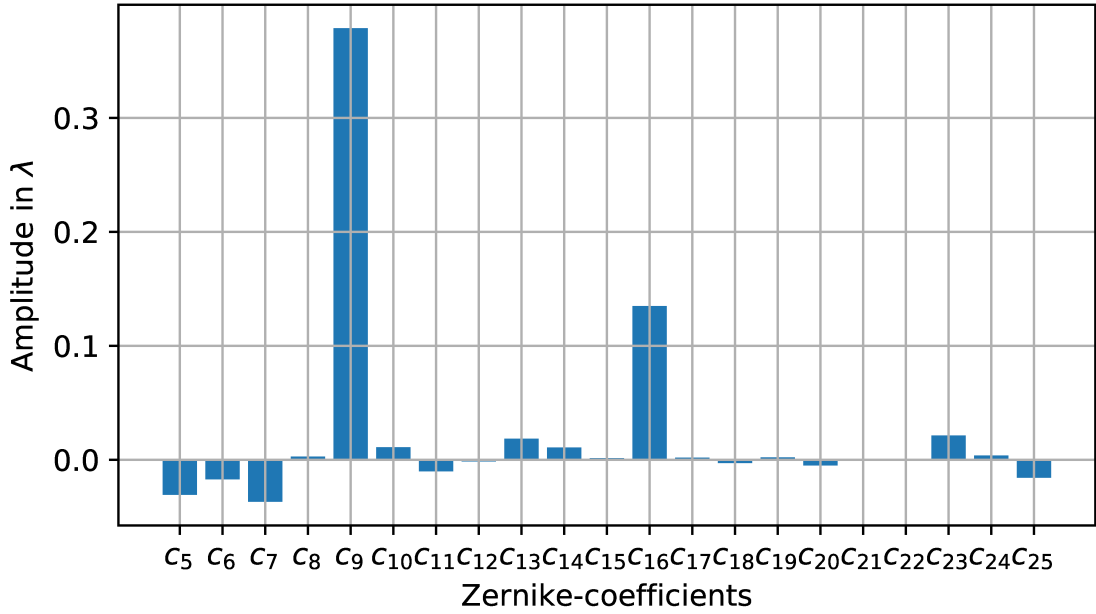


Figure 4.8.: Zernike decomposition of the wavefront of the $\theta = 7$ mrad beam in the rear surface of the focusing lens at $z = -156$ mm. The normalization radius is 2.5 mm.

are more pronounced in case of the shorter focal length. The expected stronger spherical aberration is confirmed by the Zernike decomposition of the corresponding wavefronts at the rear surface of the focus module. Here, the sign of c_9 is the same for both measurement which agrees with the theory, since both modules consist of a single lens only. Furthermore, the amplitude of c_9 is increased by approximately the same amount as the angle is increased $\frac{3}{7} \approx \frac{0.17}{0.38}$ due to the shorter focal length.

In comparison of the non-rotational symmetric aberrations, both measurements differ significantly. The $\theta = 3$ mrad measurement shows a strong elliptical shape. Its change of orientation can be seen in Fig. 4.4 from $z = -55$ mm to $z = -5$ mm, where the major axis is transformed from nearly y -oriented to nearly x -oriented, respectively. In case of $\theta = 7$ mrad, the beam shape is mainly rotational symmetric. The visual differences are also confirmed by the Zernike coefficients. Here, the main contribution is astigmatism in case of the first measurement and spherical aberration in case of the second measurement. During the experiment the $f = 325$ mm lens had to be removed from the mounting for cleaning. The lens was probably re-inserted with a slight tilt with respect to the mounting, which introduced mainly astigmatism.

The rms values as an integrating criterion do not give any insights on particular problems in the reconstruction as edge diffraction due to an imperfect radius of the region of interest or issues with dead pixels of the sensor. Hence, the visual comparison of the reconstructed beam with measurement is very useful. The sensitivity of the visual agreement can also be understood in the comparison of results of the two presented beams. The intensities of the retrieved field in the $\theta = 7$ mrad case match the measurement better. This can be seen especially in the agreement of the oscillations of the on-axis intensities on the right hand side of the caustics. The intensities of the larger θ matches in amplitude and frequency, while for the small θ a mismatch can be seen. These evident performance differences based only on visual inspection of the data are also supported by the particular quantitative results based on the weighted rms differences of the intensities. Here, the retrieved field of the second measurement shows a better performance. To understand this situation, the intensities of both measurements were investigated. A clear difference is the number of dead pixels on the camera. Only for the first measurement, a large amount of dead pixels could be identified. Thus, the acquired intensity values of the $\theta = 3$ mrad beam were filtered by a median-filter to achieve the presented results. This was unnecessary for the other measurement.

The calculation of the separated values for the M^2 -value with and without phase aberrations shows the great benefit of this method. Since the full field is retrieved, it can be propagated and converted arbitrarily. The location of computation of the M^2 -value along z is of no matter, since the propagation of the beam corresponds to a paraxial optical system with an invariant M^2 . To separate the impact of wavefront aberrations from amplitude imperfections, the phase was flattened for the retrieved fields at the rear surface of the focusing lens. By this operation the purely amplitude dependent M^2 -value could be calculated, since the degradations due to amplitude and phase are not mixed by the propagation. In case of the $\theta = 7$ mrad results, the amplitude is nearly ideal with $M^2 = 1.05$. The incorporation of the phase aberrations leads to a value of $M^2 = 1.71$, showing the strong influence of the phase aberrations. In contrast, the measurement of the $\theta = 3$ mrad beam shows different results. Here, the flattened field has $M^2 = 1.10$ and the retrieved field has $M^2 = 1.34$. Thus, the distinction between phase and amplitude influence is not that clear. The reasons are that the amplitude might be influenced by the presumable tilted focusing lens or the retrieval results are not accurate enough. A combination of both reasons is also imaginable.

In general, the quality of the reconstruction and propagation of both measured laser beams agrees well with the measured data, visually. The weighted rms differences of the intensities within $\pm 1z_R$ are smaller than 1.3%. Comparing this to the results of synthetic investigations shown in Fig. 4.1, the estimated residual weighted rms wavefront error of the proposed method to retrieve the phase is less than 0.05λ for the presented experimental data. Thus, the method allows for an accurate reconstruction of the full field, which enables enhanced insights into the full field properties and further enables to increase simulation complexities by incorporating the retrieved field as a real light source in the simulation of optical systems.

5. Effective performance evaluation of perturbed Bessel-Gauss beams based on the analytical expression of the line focus

The demand of applications with quasi Bessel beams is growing continuously. Such beams possess special properties like the generation of a long but narrow line focus and the ability of so-called self-healing. The generation of an axial line focus is in particular attractive for applications which require a small lateral extend but at the same time a large depth of focus. For classical beams with a spherical or parabolic carrier wave both demands can typically not be achieved, because the lateral and axial resolution are coupled by the numerical aperture, respectively the far field convergence angle. A small lateral width of the beam can only be generated by a large convergence angle, which simultaneously limits the axial length according to Eq. 2.33. Quasi Bessel beams are used in applications that require a signal over a long axial length while enabling a large lateral resolution, e.g., optical coherence tomography, materials processing or optical tweezers [4,20,79,80]. They can be generated by several methods. Most important is the conical wavefront, which focuses light along a line as introduced in section 2.1.3 and 3.3. This conical wavefront can be generated by, e.g., a phase mask, a ring lens or an axicon. A more comprehensive list of methods to create quasi Bessel beams is given in [19].

Simulations of optical systems involving quasi Bessel beams typically do not incorporate wavefront aberrations, which are introduced due to misalignment of the optical elements or imperfections of the setup itself induced, for example by the light source as it was investigated in the previous chapter. Often, the diffraction evaluation of the quasi Bessel beam is numerically costly. If non-rotational symmetric

aberrations, for example astigmatism and coma have to be considered, the complete two-dimensional field must be sampled sufficiently dense, which is extremely complex or not even possible with standard algorithms for an increasing numerical aperture and system complexity. To understand the arising sampling issues better, the strong oscillations of the integrand shown in Fig. 3.3 can be considered. Here, the signal frequency to be sampled is more and more increasing. For systems with a spherical carrier wave, certain approximations, such as the Maréchal-criteria, which was introduced in section 3.2.2, can be used under special conditions to evaluate the diffraction pattern of a nearly ideal system [30, 49]. Unfortunately, there are currently no such criteria for the fast evaluation of the diffraction patterns for systems with a conical reference wave, which would allow to compute the performance repeatedly and fast. Thus, the diffraction based direct optimization or tolerancing of such systems remains an open challenge.

The considerations in this chapter aim the analytic and therefore fast evaluation of the on-axis intensity of a perturbed Bessel-Gauss beam (*BGB*) in order to overcome the introduced challenges. The *BGB* is generated by a Gaussian apodization function, a conical reference wave and wavefront aberrations as perturbative terms. Within this investigation, the Strehl-ratio of a *BGB* is computed not only at a single point, as conventionally done in literature [42, 43, 55], but for the complete focused line along z . To this end, the on-axis field is computed for spherical aberration, astigmatism and coma by a diffraction calculation based on the Fresnel-diffraction integral allowing for an efficient analytical treatment in the paraxial limit. The limits of the Fresnel regime are extensively discussed in [81, 82]. For the computation several approximations are introduced and discussed. They enable the derivation of an analytical formula in order to accelerate the computation and further, to integrate this into the optimization and tolerancing of optical systems with a corresponding conical reference wave.

This chapter is divided into the following sections. In section 5.1 the impact of typical wavefront aberrations on the intensity distribution of a *BGB* is inspected by full numerical diffraction calculations. An analytic calculus for the on-axis field of a *BGB* perturbed by spherical aberration, astigmatism and coma is derived and discussed in section 5.2. The introduced approximations are assessed and validated. In section 5.3 the analytic result is applied in the calculation of an extended Strehl-ratio definition along the line focus. Furthermore, this definition is applied for investi-

gating the sensitivity of an example system, which consists of catalog components to collimate light emitted by a fiber and generate a *BGB* by using an axicon. The extended Strehl-ratio is evaluated for a tilted collimator, which induces astigmatism.

Parts of this chapter are already published by the author et al. in [83].

5.1. Full diffraction calculation of perturbed Bessel-Gauss beams

In this section, the effect of classical wavefront aberrations on a *BGB* is given visually. This helps understanding the impact of classical wavefront aberrations on the line focus of *BGBs*, since their properties differ significantly from classical beams like Gaussian beams or beams with a spherical wavefront.

As in section 3.3, a *BGB* with a fixed truncation ratio of $w/R = 2/3$ and the boundary radius $R = 1$ mm is considered. This produces a minor amount of oscillation along the optical axis due to edge diffraction at the boundary as already seen in Fig. 3.2. The wavefront aberrations may be induced by previous beam shaping optics, e.g., collimator and telescope. They are described by certain amounts of spherical aberration, astigmatism and coma. Spherical aberration is described by the Zernike-term Z_9 shown in Tab. A.1, where the boundary of the beam is set as normalization radius. Astigmatism is also defined in terms of a Zernike-term by Z_6 . To stay consistent with the calculations made in the next section, coma is defined without the balancing tilt. In Zernike-notation this can be written as a combination of Z_7 and Z_2 by $W_{\text{coma}} = C(Z_7 + 2Z_2)$, where C is the coma coefficient. The magnitude of each aberrations coefficient is equally set to $c_6 = C = c_9 = 0.1\lambda$. The corresponding wavelength of the beam is $\lambda = 632.8$ nm, which is typical for a HeNe-laser. The cone angle is defined by the numerical aperture as introduced in section 3.3 as $NA = 0.01$. To perform the diffraction calculation, the rigorous angular-spectrum-of-plane-waves propagator based on Eq. 2.14 is used and the field is sampled by 1001×1001 points.

The results of the propagated *BGB* are shown in Fig. 5.1. The axial cross-sections of the generated line focus are depicted for different wavefront errors. At the bottom, the corresponding on-axis intensities are compared against each other. The ideal

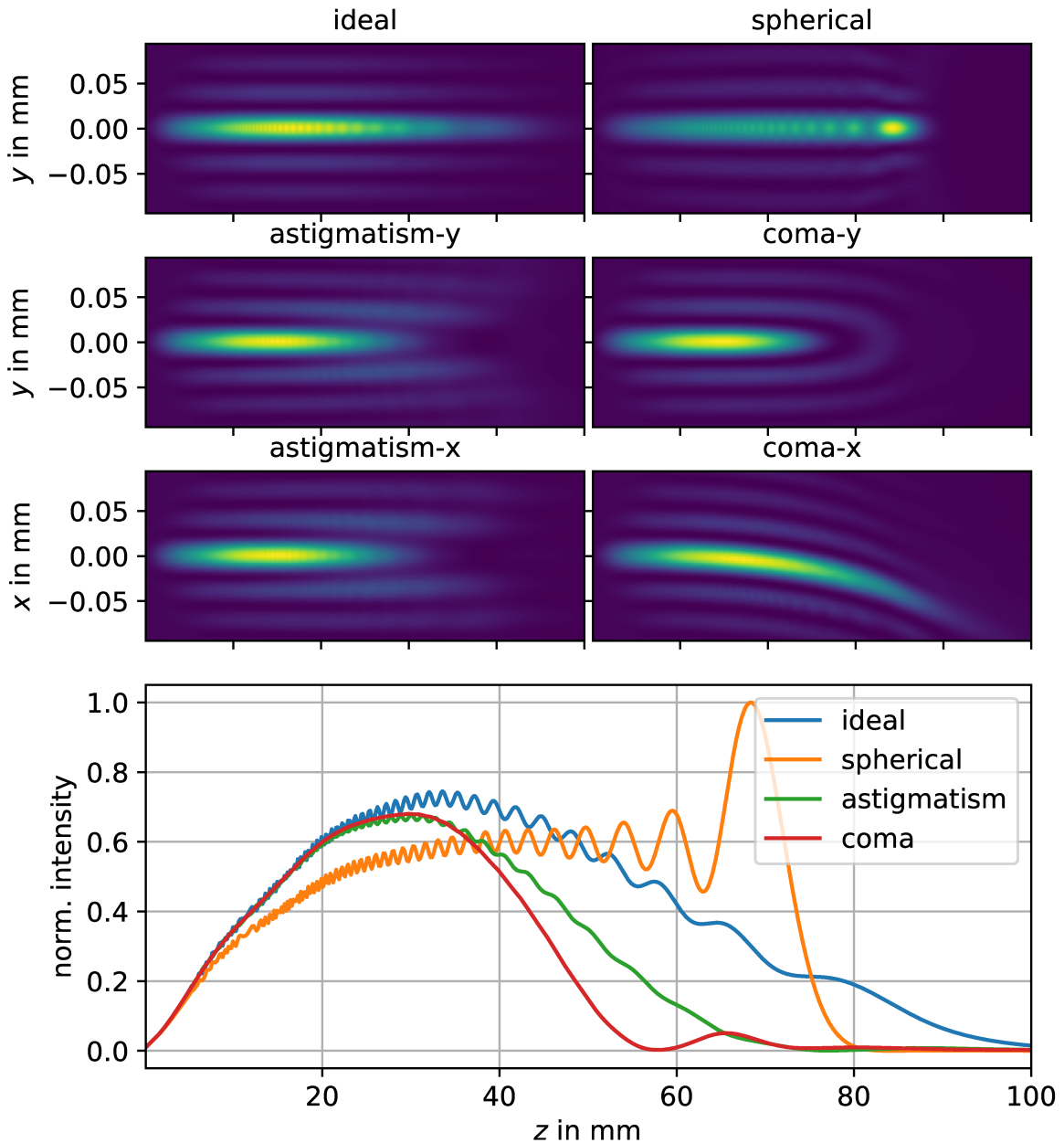


Figure 5.1.: Overview of a truncated Bessel-Gauss beam perturbed by typical wavefront aberrations. Shown are the corresponding cross-sections of the line focus and a comparison of the on-axis intensities. The ideal beam is defined by the truncation ratio of the apodization function $w/R = 2/3$ with $R = 1$ mm, $\lambda = 632.8$ nm and $NA = 0.01$.

BGB shows a similar behavior as already seen in Fig. 3.2, where the on-axis intensity is slightly modulated due to the truncation of the beam. In the cross-section of the ideal beam, the fundamental property of a constant beam width can be observed. According to section 3.3 its lateral diameter in terms of the first minimum ring is

$d = 0.76 \frac{\lambda}{NA} = 0.048$ mm, while the length of the axial focus above 50% peak intensity is about 50 mm. Thus, the resulting aspect ratio computed as the beam length divided by beam diameter is roughly 1000. This situation changes when wavefront aberrations are included. In case of spherical aberration the beam diameter varies along z , the on-axis ripples are more pronounced and a distinct peak at $z = 68$ mm, rather than a smooth focused line is observed. In comparison to the ideal beam, the peak intensity is enhanced by spherical aberration. The ripples along z are strongly damped for the beam suffering from astigmatism and the peak intensity is slightly less than for the ideal *BGB*. At the same time the length of the line focus is shorter. In the y - z and x - z cross-sections of the astigmatic beam it can be seen that the beam diameter is decreasing along z and the width of the side lobes is increased. In contrast to classical beams, only a minor difference between both cross-sections can be observed. Furthermore, the intensity is not completely dropping to zero in between the axial focus and the side lobes. These effects are more pronounced in the y - z cross-section. Here, the beam is focused stronger while the pattern itself is more blurry in comparison to the x - z cross-section. In case of the *BGB* perturbed by coma, the on-axis intensity is not modulated by regular ripples. Its peak intensity is very similar to the astigmatic beam, but the length of the line is the shortest in comparison to all other examples. In the x - z cross-section an increasing tilt of the beam along z can be observed yielding a curved line focus. In contrast to spherical aberration and astigmatism, the beam diameter is approximately invariant along z .

The calculation of these results with the given lateral sampling conditions and 601 axial sampling points required more than 1 h. For repetitive computations this is not acceptable. This problem is tackled in the next section with an approach based on analytic mathematical formulations of the Fresnel-diffraction integral in polar coordinates.

5.2. Analytical expression for the on-axis field of perturbed Bessel-Gauss beams

5.2.1. Derivation

The field of a *BGB* suffering from wavefront aberrations in the pupil can be expressed as

$$E_p(\rho_p, \phi_p) = e^{-\mu(\rho_p - \rho_s)^2} e^{ik\epsilon\rho_p} e^{i2\pi W_p(\rho_p, \phi_p)}, \quad (5.1)$$

where the first term defines the apodization with the shape-factor μ and a shift-term ρ_s , enabling a ring-shaped illumination. The second term defines the reference conical wavefront specified by the parameter $\epsilon = -\tan(\sin^{-1} NA)$ and the numerical aperture NA of the system. The last term includes the wavefront errors. It is further decomposed at the stationary point σ by using normalized pupil-coordinates $\rho = \rho_p/R$ and $\phi = \phi_p$ as

$$W_p(\rho, \phi) \approx W_0 + P|_\sigma + P'|_\sigma(\rho - \sigma) + \frac{1}{2}P''|_\sigma(\rho - \sigma)^2 + A\rho^2 \cos 2\phi + C\rho^3 \cos \phi. \quad (5.2)$$

W_0 is a constant term of the wavefront, P corresponds to the rotational-symmetric part and the last two terms are representing astigmatism and coma with the corresponding coefficients A and C . The stationary point of the conic reference wavefront overlaid with the parabolic Huygens wavelets in normalized pupil coordinates is given by

$$\sigma = \frac{z \tan(\pi/2 - \arcsin NA)}{R(1 + \tan^2(\pi/2 - \arcsin NA))}. \quad (5.3)$$

The rotational-symmetric term P and its derivatives can be expressed as a polynomial series

$$P(\rho) = \sum_{n=1}^N c_n \rho^n, \quad (5.4)$$

$$P'(\rho) = \sum_{n=1}^N c_n n \rho^{n-1}, \quad (5.5)$$

$$P''(\rho) = \sum_{n=1}^N c_n n(n-1) \rho^{n-2}. \quad (5.6)$$

The expansion of the wavefront errors in Eq. 5.2 consists of two parts. The rotational-symmetric aberrations are expanded up to an arbitrary order N . Their contributions are considered in terms of the slope and curvature at the stationary point σ . This corresponds to the general stationary-phase approach discussed in the context of ideal quasi Bessel beams in section 3.3. In addition to the rotational-symmetric wavefront errors, primary astigmatism and coma are included in the expansion to model the basic azimuthal variation of the aberrations.

In the Fresnel regime, the following integral expression describes the axial field of a perturbed *BGB*

$$E(z) = \frac{k}{i2\pi z} e^{ikz} \int_0^R \int_0^{2\pi} e^{-\mu(\rho_p - \rho_s)^2 + \frac{ik}{2z}\rho_p^2 + ik\epsilon\rho_p + i2\pi W_p(\rho_p, \phi_p)} d\phi_p d\rho_p. \quad (5.7)$$

The pupil coordinates are normalized now and rearranged into radial and azimuthal contributions. Considering the azimuthal dependence first, the following integral needs to be solved

$$\int_0^{2\pi} e^{i2\pi[A\rho^2 \cos 2\phi + C\rho^3 \cos \phi]} d\phi. \quad (5.8)$$

A solution can be obtained by expanding the exponential term into a Taylor series and applying the binomial theorem.

$$\begin{aligned} & \int_0^{2\pi} e^{i2\pi[A\rho^2 \cos 2\phi + C\rho^3 \cos \phi]} d\phi \\ &= \sum_{m=0}^M \frac{(i2\pi)^m}{m!} \sum_{j=0}^m \binom{m}{j} A^{m-j} C^j \rho^{2m+j} \int_0^{2\pi} \cos^{m-j} 2\phi \cos^j \phi d\phi. \end{aligned} \quad (5.9)$$

The remaining integral is then expressed in terms of the hypergeometric function ${}_2F_1$ [59] as

$$\begin{aligned} & \int_0^{2\pi} \cos^{m-j} 2\phi \cos^j \phi d\phi = \frac{(-1)^m}{2} \left(1 + (-1)^j\right) \sqrt{\pi} \frac{\Gamma(1/2 + j/2)}{\Gamma(1 + j/2)}. \\ & \left[(-1)^m {}_2F_1(1/2, j - m, 1 + j/2, 2) + (-1)^j {}_2F_1(1/2 + j/2, j - m, 1 + j/2, 2) \right]. \end{aligned} \quad (5.10)$$

With this formulation, a solution for the azimuthal integral is found and the radial integral is solved in the following steps. For this purpose, the derived expression so

far is rearranged to separate the radial dependence

$$\begin{aligned}
E(z) &= \frac{k}{i2\sqrt{\pi}z} e^{ikz} e^{iW_0} R^2 \sum_{m=0}^M \frac{(i2\pi)^m}{m!} \sum_{j=0}^m \binom{m}{j} A^{m-j} C^j \frac{(-1)^m}{2} \left(1 + (-1)^j\right) \\
&\quad \frac{\Gamma(1/2 + j/2)}{\Gamma(1 + j/2)} \\
&\quad \left[(-1)^m {}_2F_1(1/2, j - m, 1 + j/2, 2) + (-1)^j {}_2F_1(1/2 + j/2, j - m, 1 + j/2, 2) \right] \cdot \\
&\quad \int_0^1 e^{a\rho^2 + b\rho + c} \rho^{2m+j+1} d\rho.
\end{aligned} \tag{5.11}$$

Here, the argument of radial exponential is written in terms of the parameters a, b, c , which are given as

$$a = -\mu R^2 + \frac{ikR^2}{2z} + i\pi P''(\sigma), \tag{5.12}$$

$$b = 2\mu R\rho_s + ik\epsilon R + i2\pi(P'(\sigma) - P''(\sigma)), \tag{5.13}$$

$$c = -\mu\rho_s^2 + i2\pi\left(P(\sigma) - P'(\sigma)\sigma + \frac{1}{2}P''(\sigma)\sigma^2\right). \tag{5.14}$$

This enables a further treatment of the integral by completing the square, leading to

$$\int_0^1 e^{a\rho^2 + b\rho + c} \rho^{2m+j+1} d\rho = e^{c - \frac{b^2}{4a}} \int_0^1 e^{a(\rho + \frac{b}{2a})^2} \rho^{2m+j+1} d\rho. \tag{5.15}$$

By substituting $\rho' = \rho + \frac{b}{2a}$ and applying the binomial theorem again, this integral expression is reformulated as a standard integral by

$$\begin{aligned}
e^{c - \frac{b^2}{4a}} \int_0^1 e^{a(\rho + \frac{b}{2a})^2} \rho^{2m+j+1} d\rho &= e^{c - \frac{b^2}{4a}} \int_{\frac{b}{2a}}^{1 + \frac{b}{2a}} e^{a\rho'^2} \left(\rho' - \frac{b}{2a}\right)^{2m+j+1} d\rho' \\
&= e^{c - \frac{b^2}{4a}} \sum_{l=0}^{2m+j+1} \binom{2m+j+1}{l} \left(-\frac{b}{2a}\right)^{2m+j+1-l} \int_{\frac{b}{2a}}^{1 + \frac{b}{2a}} e^{a\rho'^2} \rho'^l d\rho'.
\end{aligned} \tag{5.16}$$

Here, the definition of the generalized Gamma-function $\Gamma(z, x_1, x_2)$ [59] is incorporated:

$$\Gamma(z, x_1, x_2) = \int_{x_1}^{x_2} e^{-x} x^{z-1} dx. \tag{5.17}$$

This allows to write the integral of Eq. 5.16 as

$$\int_{\frac{b}{2a}}^{1+\frac{b}{2a}} e^{a\rho'^2} \rho'^l d\rho' = \frac{1}{2} (-a)^{-l/2-1/2} \Gamma \left(l/2 + 1/2, -a \left(\frac{b}{2a} \right)^2, -a \left(1 + \frac{b}{2a} \right)^2 \right). \quad (5.18)$$

With these formulations, the on-axis field of a perturbed *BGB* can be expressed analytically by summations over Gamma-functions and hypergeometric functions. The final equation, including all the previous derivation steps, is given by Eq. 5.19

$$\begin{aligned} E(z) = & \frac{-bkR^2}{16\sqrt{\pi a a z}} e^{ikz+iW_0+c-b^2/4a} \sum_{m=0}^M \frac{(i2\pi)^m}{m!} \sum_{j=0}^m \binom{m}{j} A^{m-j} C^j. \\ & \left[(-1)^m + (-1)^{m+j} \right] \frac{\Gamma \left(\frac{1+j}{2} \right)}{\Gamma \left(1 + \frac{j}{2} \right)} \left[(-1)^m {}_2F_1 \left(\frac{1}{2}, j-m, 1 + \frac{j}{2}, 2 \right) + \right. \\ & \left. (-1)^j {}_2F_1 \left(\frac{1+j}{2}, j-m, 1 + \frac{j}{2}, 2 \right) \right] \sum_{l=0}^{2m+j+1} \binom{2m+j+1}{l} \left(-\frac{b}{2a} \right)^{2m+j-l}. \\ & (-a)^{-\frac{l}{2}} \Gamma \left(\frac{l+1}{2}, -a \left(\frac{b}{2a} \right)^2, -a \left(1 + \frac{b}{2a} \right)^2 \right). \end{aligned} \quad (5.19)$$

5.2.2. Results and discussion

The derived analytic expression for the on-axis field of a *BGB* suffering from aberrations is based on two main approximations. To investigate the validity of these approximations, their impact on the axial intensity is tested against numerical rigorous simulations based on Eq. 2.14. The first approximation is the rotational-symmetric expansion of the wavefront error and the corresponding incorporation in the calculation by the stationary-phase idea, which was introduced in section 3.3. The Taylor expansion of the exponential function that includes the azimuthal dependence in Eq. 5.9 and limiting the resulting series representation to finite orders in practical scenarios is the second approximation.

The rotational-symmetric aberrations considered in Eq. 5.4 can be in principle of arbitrary order. Up to second order, the contributions are treated exactly. Higher orders are considered by approximation using the local slope and curvature of *P* in

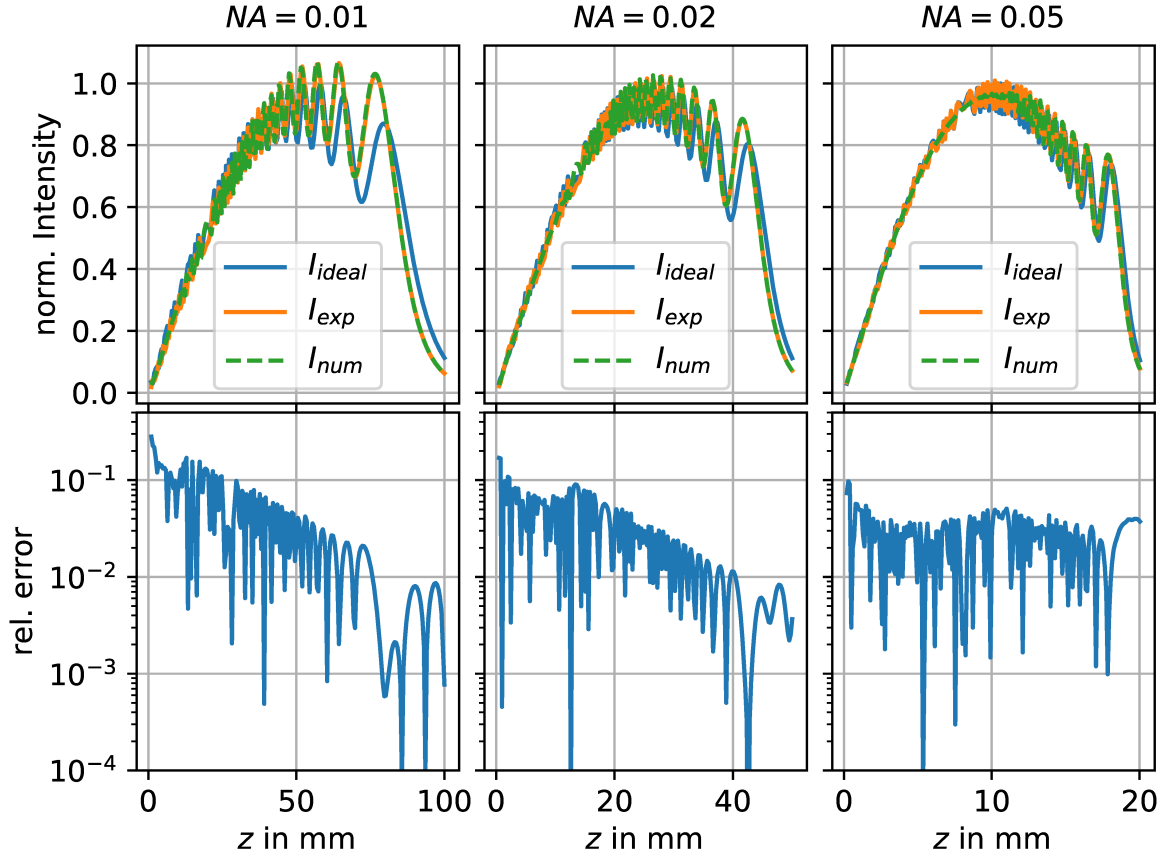


Figure 5.2.: Comparison of the on-axis intensity of the ideal Bessel-Gauss-line (I_{ideal}) with $W_p = 0$ and the perturbed Bessel-Gauss-line calculated by the expansion according to Eq. 5.19 (I_{exp}) and a rigorous propagation method (I_{num}) described in [84] for different NA . The wavefront error in the perturbed cases is rotational-symmetric with $W_p = 0.5\lambda(\rho^4 - \rho^2)$. Notice, that the z -scale is changed according to the NA . In the bottom row, the relative error between the (I_{exp}) and (I_{num}) is plotted. The results, shown in this figure, are already published by the author et al. in [83].

terms of the stationary-phase-approach as introduced in section 3.3. For the local expression of spherical aberrations at individual stationary points of the parabolic wavelet and the conic wave, it is assumed that the slope of the cone is dominant compared to the occurring aberrations, i.e., the exponential function including the cone is strongly oscillating. Hence, only a narrow ring-element in the pupil around the stationary point contributes to a short field element on-axis. The increase of the NA can be interpreted as the increase of k in the stationary-phase-approach. That means the oscillations are becoming more rapid with a larger NA leading to an improved accuracy of the stationary-phase approach. In addition, the influence

of spherical aberration onto the line focus decreases with increasing NA , which is in contrast to classical beams. In Fig. 5.2 this is demonstrated by the comparison of the intensities of the ideal Bessel-Gauss line focus with the perturbed line focus. The perturbed intensities are calculated by the derived analytic expression according to Eq. 5.19 and a rigorous numerical method based on Eq. 2.14. The differences between ideal and perturbed Bessel-Gauss lines decrease with increasing NA , which can be explained by the narrower corresponding ring-element in the pupil that contributes to the corresponding on-axis field element. In contrast to classical beams, the intensity of a *BGB* perturbed by pure spherical aberration can exceed the intensity of the ideal beam. This can be understood within the stationary-phase approximation, since different curvatures can be locally interpreted as a local change of the NA . Therefore, depending on the sign of the corresponding curvature, the light is focused stronger than in the ideal situation. At the same time this means that energy is redistributed along the axial line focus, which results in an overall shorter or longer line focus. This can also be observed in Fig. 5.2. The axial length of the perturbed *BGB* is smaller for all three NA -cases than the ideal line length. For the smallest NA , the impact of the spherical aberration is the largest, even though the coefficients are equal for all three scenarios. This is apparent in the enhanced peak intensity and the shortened length of the line focus.

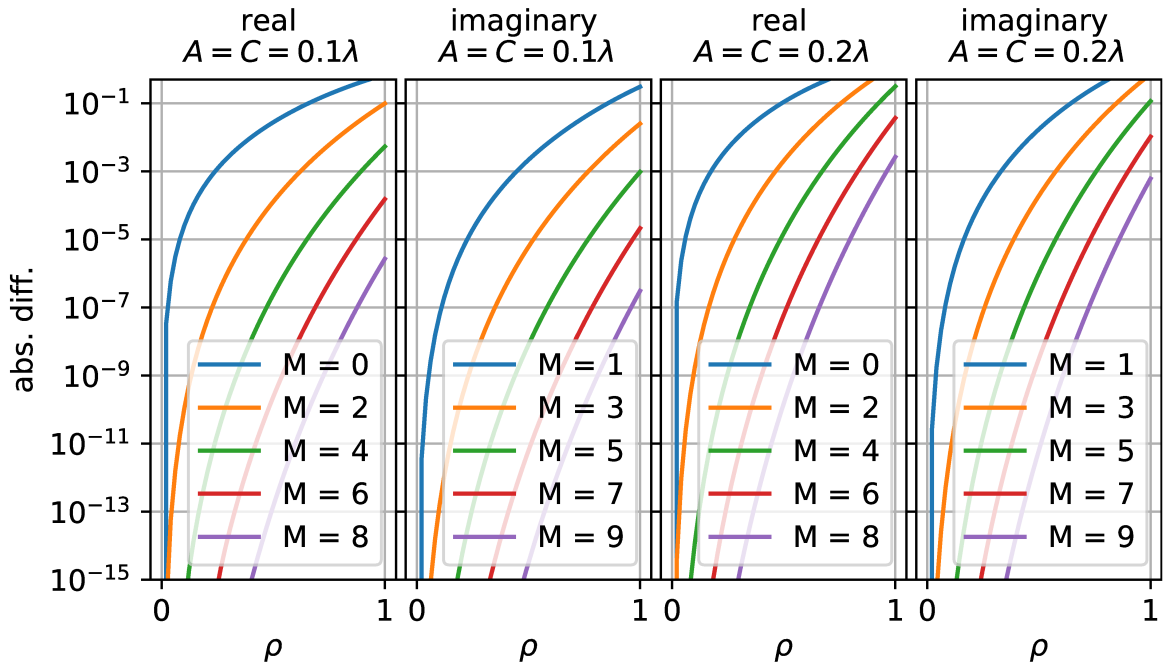


Figure 5.3.: Accuracy of the azimuthal expansion in Eq. 5.9 for finite orders of M and different coefficient amplitudes for astigmatism A and coma C .

The second approximation in the calculation of the on-axis field is the series expansion of the azimuthal function in Eq. 5.9 and the corresponding limitation of this series to finite valued orders of M for a practical applicability. The maximum induced errors of this truncation are estimated in the following way: Since $|\cos(x)| \leq 1$ and ρ is the normalized radius, the maximum error occurs at the boundary of the aperture ($\rho = 1$), i.e., $\text{MAX}[|A\rho^2 \cos 2\phi + C\rho^3 \cos \phi|] \leq |A| + |C|$. Thus, dependent on the coefficients of A and C , larger values for M must be taken into account to assure a particular accuracy of the series expansion. In Fig. 5.3 the absolute difference of the real and imaginary parts between the exponential function and its expansion are plotted for different coefficient amplitudes and expansion orders M . To ensure an error smaller than, e.g., $1/100$ for the real and the imaginary part at the boundary and $A = C = 0.1\lambda$, at least five orders must be considered. If the aberration-coefficients are doubled to $A = C = 0.2\lambda$, the same accuracy can only be achieved with at least nine orders. If the Gaussian apodization function is dropping fast enough towards the edge of the aperture ($R > 1/\sqrt{\mu}$), the increasing error of the expansion is less weighted at the boundary by the Gaussian apodization, which can strongly relax the situation. Consequently, less azimuthal expansion orders are necessary for a specified accuracy.

The azimuthal wavefront error contributions that can be considered according to Eq. 5.19 are limited to primary astigmatism and coma. Though other terms can be included in the derivation, for typical setups, like a fiber-collimator and a subsequent axicon that generates a quasi Bessel beam, the dominant aberrations are primary astigmatism and coma due to misalignment and spherical aberrations due to the typically spherical surfaces of the collimation optics. Therefore, the most significant contributions in the degradation of the line focus are described with the proposed decomposition of the wavefront according to Eq. 5.2.

In case of coma, the lateral position of the peak intensity is variant along the evolution in z -direction and follows a curved trajectory. This effect can be observed for both classical and quasi Bessel beams. The cross-section of the coma plot in the x - z plane in Fig. 5.1 illustrates this behavior. In the application of Eq. 5.19, only the on-axis field is considered and the bent line is not included. For applications where a straight line focus is absolutely necessary, coma must be kept minimal and the proposed method can be fully applied to compute the beam intensity. If the line focus is allowed or even intended to be strongly curved, the investigation of the

on-axis field is of limited meaningfulness. Consequently, Eq. 5.19 is eventually not applicable, depending on the characteristics of the line and the desired application.

A feasible method for profiling arbitrary on-axis intensity distributions according to [48] was already given in section 3.3.3. It allows to identify an initial amplitude which generates the intended axial profile in case of rotational symmetry. This idea can be synthesized with the presented analytic approach which allows the description of arbitrary shaped focus lines and additionally includes the azimuthal variations of the wavefront. Consequently, the impact of astigmatism and coma on arbitrarily shaped line focuses can be investigated. For this purpose, the initial amplitude function can be described by a coherent superposition of Gaussian rings, which are defined by their corresponding shape factor and radial position. The corresponding wavefront aberrations are equal for all Gaussian rings and Eq. 5.19 must be evaluated for every ring. This superposition is similar to the decomposition of higher order wavefront errors in the previous chapter with *RBFs*. The difference is that in the previous chapter the phase was described by a set of laterally shifted Gaussian functions, but within this scheme, the amplitude would be laterally decomposed into Gaussian ring functions.

5.3. Sensitivity analysis of an example system by an extended Strehl-ratio definition

To evaluate the performance of a *BGB*, the concept of the classical Strehl-ratio, as described in section 3.2.2, is extended by defining the *SR* not only at a single focus point, but along z to account for the line focus behavior of a *BGB*. Thus, the classical definition of Eq. 3.12 is modified to

$$SR(z) = \frac{I_{real}(r_i = 0, z)}{I_{ideal}(r_i = 0, z)} = \left| \frac{E_{real}(r_i = 0, z)}{E_{ideal}(r_i = 0, z)} \right|^2. \quad (5.20)$$

The ideal on-axis field is obtained by Eq. 3.37 or by Eq. 5.19 with $c_n = A = C = 0$ and the perturbed field is obtained by Eq. 5.19 with inserted corresponding coefficients.

Eq. 5.20 is applied to compute the extended Strehl-ratio of the line focus generated

by a setup consisting of a fiber collimator and subsequent axicon. The performance of the line is investigated for several misaligned configurations of the collimator lens.

The example system is composed of two catalog elements. To collimate light emitted by a fiber with $NA = 0.1$, an achromate with a focal length $f = 100$ mm is used (LAO-100.0-26.5 from CVI Laser Optics). The conic wavefront is generated by an axicon (AX2520 from Thorlabs) where the generated conic wavefront is defined by $NA = 0.17$. In Fig. 5.4 the layout of the example system is shown. A Gaussian apodization is assumed for the calculation. It is specified by $1/\sqrt{\mu} = R = 10$ mm that corresponds to $1/e^2$ of the maximum intensity at the boundary of the aperture. The simulation is performed at a wavelength of $\lambda = 550$ nm.

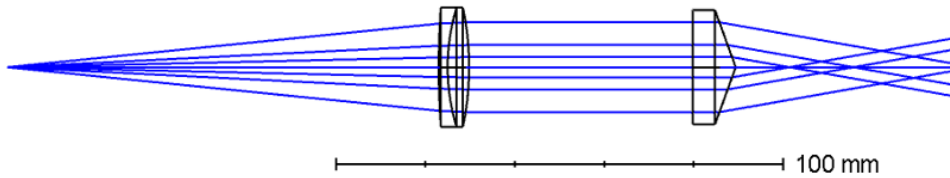


Figure 5.4.: Layout of the example system. It consists of two catalog components to collimate light, emitted by a fiber and generate a line-focus with an axicon.

The sensitivity is exemplary investigated regarding a tilt of the collimator lens which mainly induces astigmatism. The results of the misaligned achromate are depicted in Fig. 5.5 by plotting the dependence of the Zernike astigmatism coefficient on the tilt and the corresponding Strehl-ratios along the line focus according to Eq. 5.20. The amplitude of the astigmatism coefficient increases quadratically with the tilt. With increasing tilt, the performance of the system drops significantly towards the end of the generated line focus. The typical value for a diffraction limited performance in terms of a Strehl-ratio better than 0.8 is only achieved for 88% of the length of the line if the collimator is tilted by 1° . Generally, it is observed that the performance drops for larger values of z . This fully agrees with the understanding of the stationary phase: The radius of the mainly contributing stationary ring element in the pupil σ is directly proportional to the propagation distance z according to Eq. 5.3. Simultaneously, the wavefront error rises towards the boundary of the pupil. Therefore, the localized performance drop of the line focus is a direct consequence of the properties of the conic reference wavefront and the usual grow of wavefront errors towards the edge of the pupil.

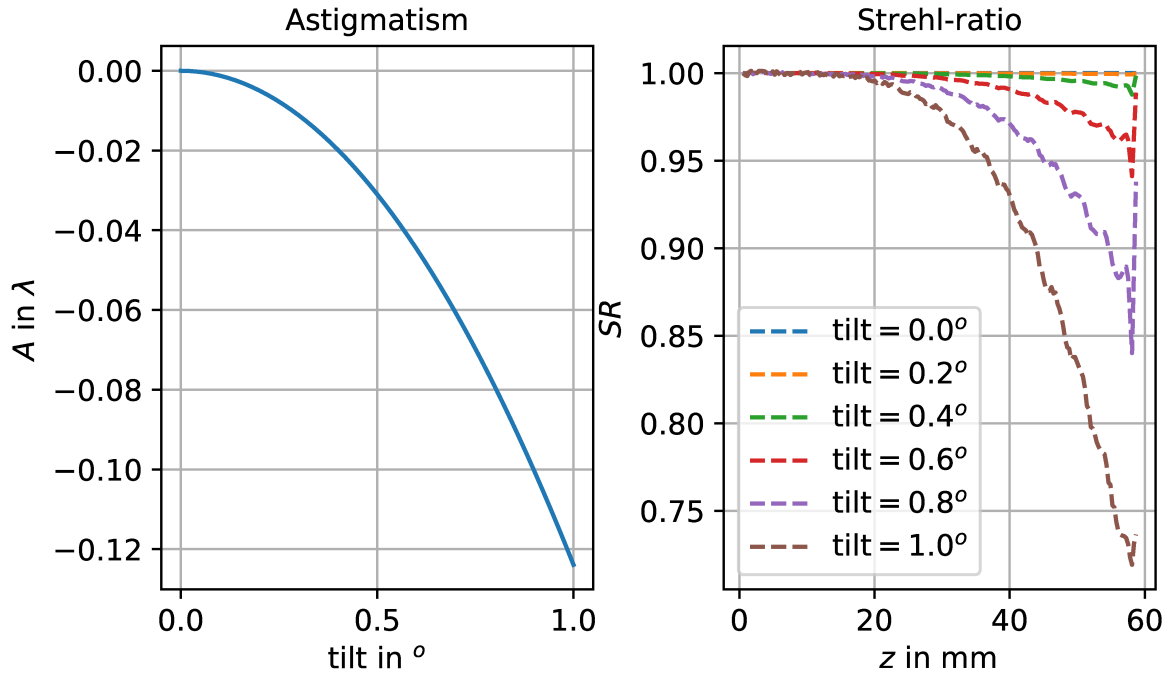


Figure 5.5.: Resulting astigmatism coefficients (left) and corresponding Strehl-ratios (right). The astigmatism is provoked by a tilt of the collimator lens that is shown in Fig. 5.4. The results, shown in this figure, are already published by the author et al. in [83].

The information that are obtained by the extended SR can be condensed to two single numbers. This offers an easier understanding and implementation as a criterion for optimization or tolerancing purposes. The first value is the mean value of $SR(z)$. It corresponds to the overall performance of the line focus. The second value is the standard-deviation. This can be understood as a measure of uniformity of the line performance. A small standard deviation indicates a small interval of data and therefore a good uniformity and vice versa. Both values are computed exemplary for the corresponding results shown in Fig. 5.5. The mean SR values for the tilts of the collimator and the standard deviations, are in between 1.00 to 0.94 and 0.00 and 0.08, respectively. The overall quality in terms of the mean value decreases with increasing tilt, while the uniformity decreases as well. This agrees with the interpretation of the corresponding values of the Strehl-ratios. Thus, the combined values of mean and standard-deviation of the z -dependent Strehl-ratio can be applied in the quantitative characterization of the line focus generated by a perturbed BGB .

6. Passive athermalization of refractive optical systems for high power laser applications

The design of optical systems for guiding and shaping high power laser beams is becoming more and more challenging as the laser power increases and the performance requirements tighten. The thermal lensing effects induced by the bulk absorption in the lens material are growing with higher laser powers. Consequently, the individual components of the laser guiding systems change their focal power dependent on the employed laser power. This effect is induced by the temperature change, which leads to an overall change of the laser beam in phase and amplitude. This is a critical issue for applications, where the focus position is not actively controlled during operation, in particular. To keep the focal power of the optical system invariant with laser power and temperature, the systems needs to be athermalized within the design. This can be done by the combination of different materials in order to achieve a compensation effect of the induced focal power shifts.

Passive athermalization is common practice for a wide range of applications, where the environmental conditions are homogeneously varying, e.g., in automotive industry. Here, the temperature changes homogeneously for the optical elements as well as for the mounting. To athermalize a paraxial system under such conditions, the well known theory and its extensions described in a variety of textbooks and publications as briefly introduced in section 3.4 can be applied [21, 22, 64, 85, 86]. If the temperature is not homogeneous, higher sophisticated techniques need to be applied that usually require finite-element-methods [26, 27]. Unfortunately, their combination with optical design tools is complex and typically requires a tremendous interdisciplinary knowledge. In the design of laser resonators, the thermal lensing effect plays an important role and must be taken into account as the laser

power increases. In contrast to a temperature change induced by the environment, in a laser resonator the laser beam itself heats up the system. Here, the beam width is typically considerably smaller than the aperture of the optics to avoid edge diffraction effects, leading to an inhomogeneous source term for the temperature distribution. This problem is addressed in many publications, mostly dealing with different geometries in the calculation of laser resonators [25, 87–89].

To passively athermalize the first order properties like the focal power and the magnification of a refractive laser guiding system such as a telescope, the paraxial system properties must be combined with the temperature distribution inside the lenses and its consequences, similarly to the homogeneous scenario. Due to the inhomogeneous temperature, the refractive index is not longer constant and its gradient must be considered in addition.

In this chapter, based on the solution of the modified heat-equation described by Moritz in [90], the focal power shift of a thin lens which is illuminated by a fundamental Gaussian intensity profile is derived. The induced change of the focal power of a single lens is applied in the derivation of a set of formulas to athermalize fundamental optical systems like two lenses in close contact, and two and three separated lenses to minimize the effects of a focal power shift and an undesired beam width change. These athermalization formulas support the optical designer in the process of initial system search for high power laser applications by connecting paraxial layout data with material and laser parameters. Therefore, only certain material combinations and layout geometries are achievable and should be considered.

This chapter is structured into the following sections. In section 6.1, the temperature distribution inside a thin lens is derived. The heat source is modeled by the illumination of the lens with a high power fundamental Gaussian mode and a fixed temperature on the boundary. Afterwards, the additional focal power of a heated lens is formulated by performing a paraxial raytrace through the gradient-index medium in section 6.2. The results of the additional focal power are further analyzed and a purely material dependent parameter is introduced and discussed in section 6.3. In section 6.4, the derived expression for the heat induced additional focal power is used to athermalize basic optical systems. In the course of this, a doublet with two lenses in close contact and two telescopes with two and three separated lenses are athermalized. In addition, the presented methodology is tested with two example systems in Zemax Opticstudio [91] in section 6.5 to investigate

the effects beyond the paraxial properties.

6.1. Temperature inside a thin lens

The modified version of the heat equation alongside the approximations behind are described in [90] and allows to directly include the curvature of the lens. It is expressed as

$$\frac{d^2T}{d\rho^2} + \frac{1}{\rho} \frac{dT}{d\rho} + \frac{1}{H} \frac{dH}{d\rho} \frac{dT}{d\rho} + A(\rho) = 0, \quad (6.1)$$

assuming a circular symmetric system with the temperature $T(\rho)$, the radial coordinate ρ , the thickness of the lens $H(\rho)$ and the heat source term $A(\rho)$. The thickness is described by $H(\rho) = d + c\rho^2 = d - \rho^2(c_1 - c_2)$, with the center thickness d and the curvatures on both sides of the lens c_1, c_2 . The heat source term includes the laser and material parameters

$$A(\rho) = A_0 e^{-\frac{\rho^2}{w^2}} = \frac{\alpha_{abs} I}{2\kappa} e^{-\frac{\rho^2}{w^2}}. \quad (6.2)$$

The laser beam is described by its peak intensity I and its width w at $1/e$ of the peak intensity. The material is characterized by the absorption coefficient α_{abs} and the thermal conductivity κ . Inserting this into Eq. 6.1 results in

$$\frac{d^2T}{d\rho^2} + \frac{1}{\rho} \frac{dT}{d\rho} + \frac{2c\rho}{d + c\rho^2} \frac{dT}{d\rho} + A_0 e^{-\frac{\rho^2}{w^2}} = 0. \quad (6.3)$$

This equation can be solved by assuming rotational symmetry corresponding to $\left. \frac{dT}{d\rho} \right|_{\rho=0} = 0$ and a fixed temperature at the boundary $T(\rho = R) = T_R$:

$$T(\rho) = T_R - \frac{A_0 w^4 c e^{\frac{d}{cw^2}}}{4d} \left(\text{Ei} \left(-\frac{d + c\rho^2}{cw^2} \right) - \text{Ei} \left(-\frac{d + cR^2}{cw^2} \right) \right) + \frac{A_0 w^2 (d + cw^2)}{4d} \cdot \left(\text{Ei} \left(-\frac{\rho^2}{w^2} \right) - \text{Ei} \left(-\frac{R^2}{w^2} \right) + \log \left(\frac{d + c\rho^2}{\rho^2} \right) - \log \left(\frac{d + cR^2}{R^2} \right) \right). \quad (6.4)$$

Here, $\text{Ei}(x)$ is the exponential integral [59]. The temperature distribution inside a lens is plotted for several glasses in Fig. 6.1 to illustrate the behavior of Eq. 6.4.

Therefore, a typical biconvex lens is chosen and the temperature at the boundary is fixed to room temperature. The shape of the curves are similarly, but the absolute values differ significantly. The special glass 'LASF35' shows a strong temperature increase compared to the other glasses up to 147 °C on-axis, which can be explained by its strong absorption at a wavelength of 500 nm. In contrast, the temperature inside 'N-BK7' is just slightly increased by 5 °C on-axis due to its low absorption. The other example glasses lie in between those two.

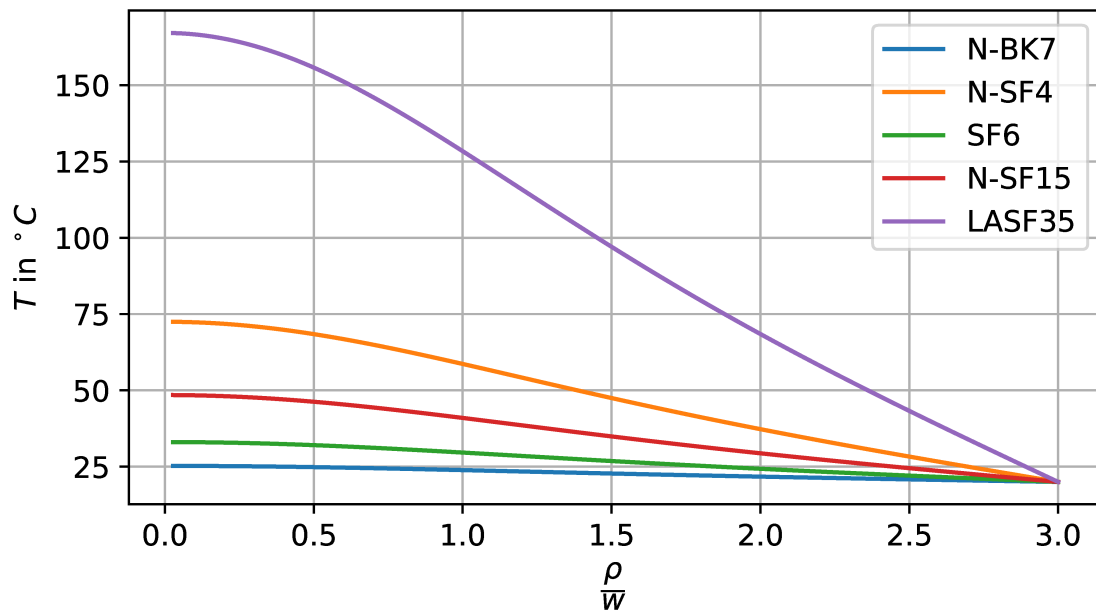


Figure 6.1.: Temperature distribution inside a heated lens with different glasses at a wavelength of 500 nm, a laser power of 100 Watt and a fixed temperature at the boundary $T_R = 20$ °C. The parameters of the simulated lens are $d = 5$ mm, $R = 9$ mm, $c_1 = -c_2 = 0.01$ mm⁻¹ and the width of the laser is defined as $w = 3$ mm. The glass parameters are taken from the Schott data sheets [92].

6.2. Focal power of a heated lens

In this section, the derived expression for the temperature inside the lens is used to perform a paraxial raytrace through a gradient-index medium to calculate the additional focal power of a heated lens. The temperature change described by Eq. 6.4 induces a change of the refractive index. In linear approximation, this

can be described as

$$\Delta n(\rho) = \frac{dn}{dT} \Delta T(\rho) = \beta \Delta T(\rho), \quad (6.5)$$

with temperature change relative to the boundary as $\Delta T = T(\rho) - T_R$ and the material specific constant $\beta = \frac{dn}{dT}$. To incorporate the inhomogeneous refractive index into the model for the additional focal power, a raytrace through a gradient index medium is performed. This is done by starting with the Eikonal equation under paraxial and rotational-symmetric conditions [29]

$$\frac{d^2 \rho}{dz^2} = \frac{1}{n(\rho)} \frac{dn(\rho)}{d\rho}. \quad (6.6)$$

Assuming a weak parabolic refractive index $n(\rho) \approx n_0 + \frac{1}{2}n_2\rho^2$, the following second-order linear ordinary differential equation has to be solved

$$\frac{d^2 \rho}{dz^2} - \frac{n_2}{n_0} \rho(z) = 0. \quad (6.7)$$

The solution of Eq. 6.7 for the ray trajectory $\rho(z)$ and the ray angle $\theta(z) = \frac{\partial \rho}{\partial z}$ are

$$\rho(z) = \frac{1}{2} \left(e^{\sqrt{\frac{n_2}{n_0}}z} + e^{-\sqrt{\frac{n_2}{n_0}}z} \right) \rho_0 + \frac{1}{2} \sqrt{\frac{n_0}{n_2}} \left(e^{\sqrt{\frac{n_2}{n_0}}z} - e^{-\sqrt{\frac{n_2}{n_0}}z} \right) \theta_0, \quad (6.8)$$

$$\theta(z) = \frac{1}{2} \sqrt{\frac{n_2}{n_0}} \left(e^{\sqrt{\frac{n_2}{n_0}}z} - e^{-\sqrt{\frac{n_2}{n_0}}z} \right) \rho_0 + \frac{1}{2} \left(e^{\sqrt{\frac{n_2}{n_0}}z} + e^{-\sqrt{\frac{n_2}{n_0}}z} \right) \theta_0. \quad (6.9)$$

Here, ρ_0 and θ_0 are the initial ray height and the initial ray angle, respectively. For a weak influence of the gradient index material, these expressions can be further reduced to

$$\rho(z) \approx \rho_0 + z\theta_0, \quad (6.10)$$

$$\theta(z) \approx \frac{n_2}{n_0} z \rho_0 + \theta_0. \quad (6.11)$$

In the paraxial *ABCD*-optics [29, 38] the ray trajectory is described by

$$\begin{bmatrix} \rho \\ \theta \end{bmatrix} = \begin{bmatrix} A & B \\ C & D \end{bmatrix} \begin{bmatrix} \rho_0 \\ \theta_0 \end{bmatrix}. \quad (6.12)$$

Thus, the $ABCD$ matrix that describes the GRIN material with a propagation length of $z = d$ reads as

$$\begin{bmatrix} 1 & d \\ \frac{n_2}{n_0}d & 1 \end{bmatrix}. \quad (6.13)$$

In the next step, the total system matrix of a GRIN material in between two curved surfaces is evaluated and compared to its pendant with a constant refractive index from the boundary n_R . Within the $ABCD$ calculus, the C -element is related to the focal power of the system by $C = -F$ [29, 38]. Hence, the additional focal power induced by the heating of the material can be computed by the difference between the heated and the cold lens as

$$\Delta F = -\frac{c_1 c_2 d}{n_R} - n_R(c_1 - c_2 + c_1 c_2 d) + \frac{c_1 c_2 d}{n_0} + n_0(c_1 - c_2 + c_1 c_2 d) - d n_2. \quad (6.14)$$

Here, n_R is the initial refractive index at the boundary and n_0 is the on-axis refractive index due to the heat. They are related by

$$n_0 = n_R + \Delta n(0) = n_R + \beta (T(0) - T_R). \quad (6.15)$$

Thus, the coefficients n_0 and n_2 are connected to the change of the refractive index induced by the temperature change and the refractive index of the heated lens is expressed as

$$n(\rho) \approx n_R + \Delta n(0) + \frac{1}{2} n_2 \rho^2. \quad (6.16)$$

Similarly, the quadratic coefficient n_2 is found as

$$n_2 = \beta \frac{d^2 \Delta T}{d\rho^2} \Big|_{\rho=0} = -\beta \frac{A_0}{2}. \quad (6.17)$$

Furthermore, the peak intensity in A_0 can be substituted by $I = \frac{2P}{\pi w^2}$ for $\frac{R}{w} > 1$, where P is the power of the fundamental Gaussian laser beam. The additional focal power of a heated thin lens ΔF can now be expressed with the presented equations. To keep the expressions simple and appropriate for the purpose of initial system search, it is expanded into a power-series up to second order in terms of the laser

power

$$\Delta F(P) \approx P \left[\frac{\alpha_{abs}\beta d}{2\pi w^2 \kappa} + G \frac{\alpha_{abs}\beta}{4\pi \kappa} \left(c_1 c_2 + \frac{c_1 - c_2}{d} - \frac{c_1 c_2}{n_R^2} \right) \right] + P^2 \left[G^2 \frac{\alpha_{abs}^2 \beta^2 c_1 c_2}{16\pi^2 \kappa^2 d n_R^3} \right], \quad (6.18)$$

where the parameter G is an abbreviation for

$$G = -w^2 c e^{\frac{d}{w^2 c}} \left[\text{Ei} \left(\frac{-d}{w^2 c} \right) - \text{Ei} \left(\frac{-cR^2 + d}{w^2 c} \right) \right] + (w^2 c + d) \left[-\log \left(\frac{R^2 c + d}{R^2} \right) + \log(d) - \text{Ei} \left(\frac{-R^2}{w^2} \right) - 2\log(w) + \gamma \right]. \quad (6.19)$$

Here, γ is Euler's constant ($\gamma \simeq 0.577216$). The final focal power of a heated lens can be expressed as the sum of the initial focal power F_{init} and the additional perturbations due to the heat as

$$F = F_{\text{init}} + \Delta F = F_{\text{init}} + \Delta F_{\text{cylinder}} + \Delta F_{\text{curvature}}, \quad (6.20)$$

$$\Delta F_{\text{cylinder}} = P \frac{\alpha_{abs}\beta d}{2\pi w^2 \kappa}, \quad (6.21)$$

$$\Delta F_{\text{curvature}} = PG \frac{\alpha_{abs}\beta}{4\pi \kappa} \left(c_1 c_2 + \frac{c_1 - c_2}{d} - \frac{c_1 c_2}{n_R^2} \right) + P^2 G^2 \frac{\alpha_{abs}^2 \beta^2 c_1 c_2}{16\pi^2 \kappa^2 d n_R^3}. \quad (6.22)$$

The curvature independent part, Eq. 6.21, equals the results found in literature for the focal power of an axial cylinder heated by a fundamental Gaussian laser beam [93,94]. To investigate the additional influence of the curved surfaces, Eq. 6.20 is further analyzed. For this purpose, the curvature independent and dependent parts are compared to the initial focal power for different lens geometries and glasses at various laser powers.

The results of this investigation are presented in Fig. 6.2. As expected both ratios, $\frac{\Delta F_{\text{cylinder}}}{F_{\text{init}}}$ and $\frac{\Delta F_{\text{curvature}}}{F_{\text{init}}}$, increase with higher laser powers. The ratio of the curvature dependence is more than one order of magnitude smaller compared to the ratio of the pure cylinder dependence for the whole range of the applied laser power. Thus, in the investigations in the section 6.4 only the additional focal power of the GRIN cylinder $\Delta F_{\text{cylinder}}$ is further considered, such that $\Delta F \approx \Delta F_{\text{cylinder}}$. The additional focal power is strongly influenced by the glass choice. E.g., in comparison 'LASF35'

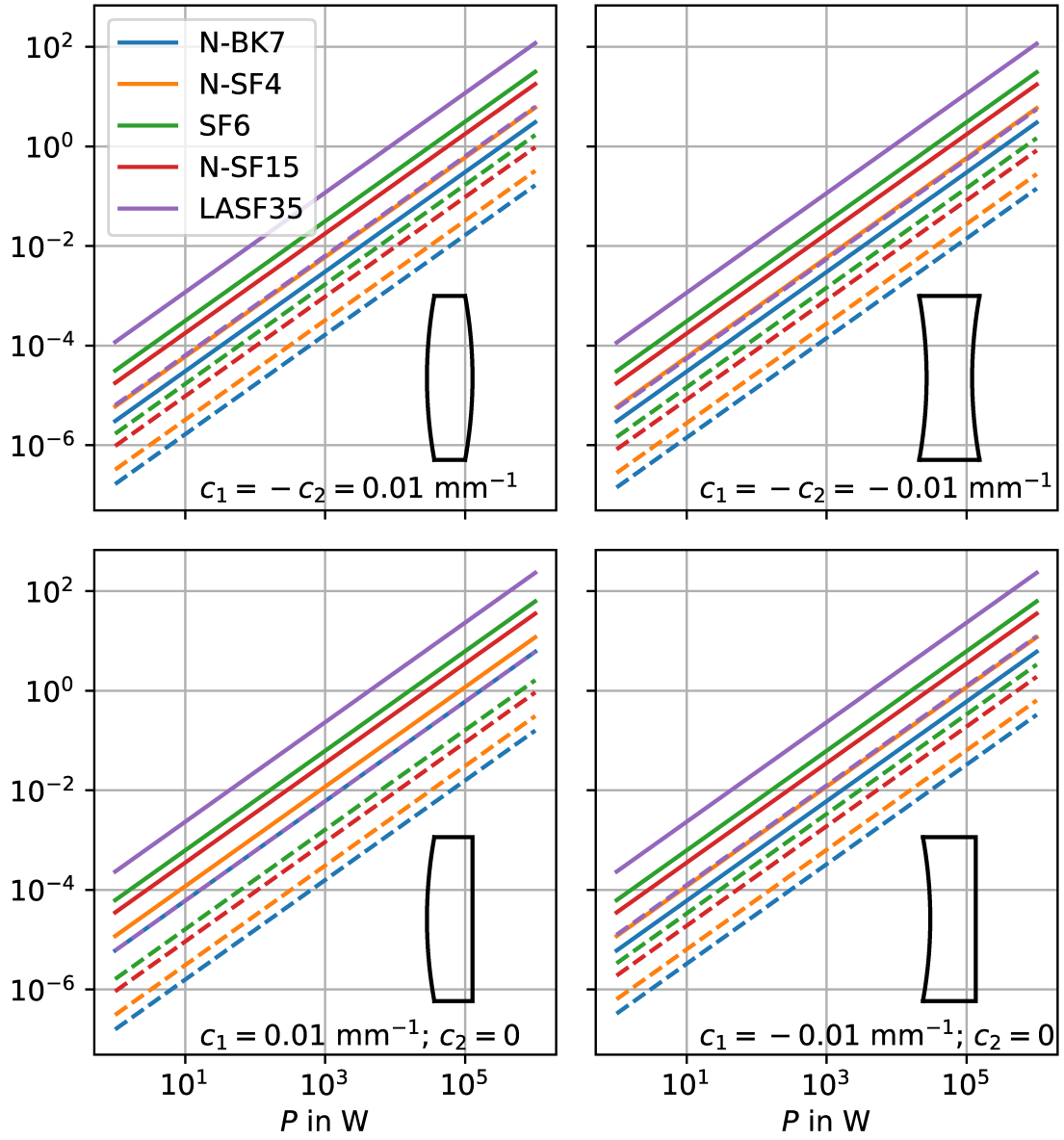


Figure 6.2.: Ratio of the focal power expansion dependent on the laser power for different glasses and lens geometries at room temperature and a wavelength of 500 nm. The solid lines shows the power dependence of $\frac{\Delta F_{\text{cylinder}}}{F_{\text{init}}}$ and the dashed lines show the power dependence of $\frac{\Delta F_{\text{curvature}}}{F_{\text{init}}}$. The parameters of the lenses are $d = 5$ mm, $R = 9$ mm. The curvatures are written in the plots. The laser beam width is $w = 3$ mm.

is by far the worst glass choice. Here, $\frac{\Delta F_{\text{cylinder}}}{F_{\text{init}}}$ exceeds 1% at approximately 85 W for the symmetrical lenses and 43 W for the asymmetrical lenses, whereas this is the case for 'N-BK7' at 3.3 kW and 1.6 kW, respectively. This is also in very good agreement to the observed temperatures in Fig. 6.1, where 'LASF35' showed the highest temperature and 'N-BK7' the lowest. The order of 'SF6' and 'N-SF4' is the other way round from Fig. 6.2 to Fig. 6.1, which is explainable by the combination of the material parameters of the glasses, in particular β .

6.3. Material parameter ξ

The properties of the materials at a certain wavelength can be concluded by the material specific parameter ξ as

$$\xi = \frac{\alpha_{\text{abs}}\beta}{\kappa}. \quad (6.23)$$

This allows an easier categorization of the materials according to their properties that are determining the thermally induced behavior. With this definition Eq. 6.21 is formulated more compact as

$$\Delta F_{\text{cylinder}}(P) = P\xi \frac{d}{2\pi w^2}, \quad (6.24)$$

where ξ is directly proportional to the additional focal power of the heated lens. It is thus possible to distinguish between the individual factors that have an impact on the focal power. According to Eq. 6.24 those are the laser parameters such as laser power and beam width, the lens material and the lens thickness itself. All these parameters are independent to each other, which is beneficial for further compensation purposes as it is discussed in the next section.

To get an overview of the thermal properties, ξ is plotted in Fig. 6.3 ordered from negative to positive valued ξ for the Schott glasses listed in Tab. A.2 at a fixed wavelength of $\lambda = 500 \text{ nm}$ and at room temperature. What is remarkable is the significantly higher proportion of glasses that have a positive ξ . Additionally, the value range of the positive valued glasses for ξ is clearly larger than for the negative valued glasses. This already indicates the complexity of an appropriate glass choice with the limited amount of glasses in order to achieve a certain balancing effect, as

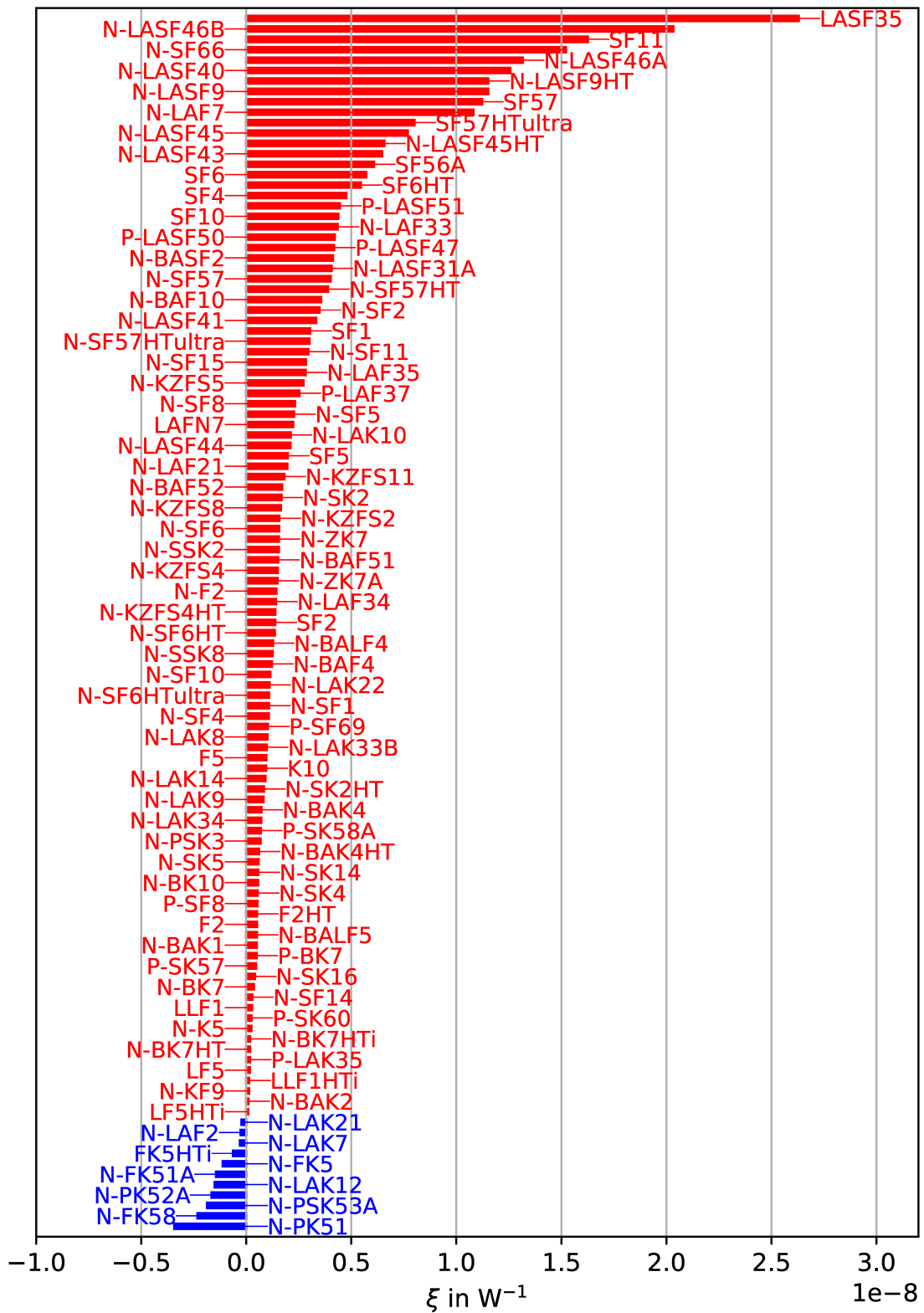


Figure 6.3.: Comparison of the thermal material parameter ξ for various Schott glasses at $\lambda = 500$ nm and at room temperature according to Tab. A.2.

it is introduced and discussed in the next section.

Comparing the results from Fig. 6.2 with the the plot of ξ in Fig. 6.3, the order of the glasses the ratio of the focal power expansion is identical to the order of the glasses according to ξ . The most sensitive glass regarding the heat impact, 'LASF35', has by far the largest ξ and 'N-BK7' has the smallest ξ . Therefore, the selection of glasses, which are suitable for high power applications, can be aided by the analysis of the corresponding thermal material parameter ξ , since this can be easily calculated according to Eq. 6.23.

6.4. Application

In this section, the result of the additional focal power of a heated thin lens evoked by the illumination of a fundamental Gaussian intensity profile is used to exemplary athermalize basic optical systems. At first, Eq. 6.24 is used to derive a condition to fix the focal power of a doublet consisting of two thin lenses in close contact. In the second example, a telescope system consisting of two separated thin lenses is kept afocal with varied laser power but the beam width is not controlled. Whereas in the third example three separated thin lenses are utilized for the simultaneous athermalization regarding the overall focal power and the beam width at the third lens of a telescope. A sketch of the telescopes is given in Fig. 6.4 with the two-lens telescope on the left and the three-lens telescope on the right.

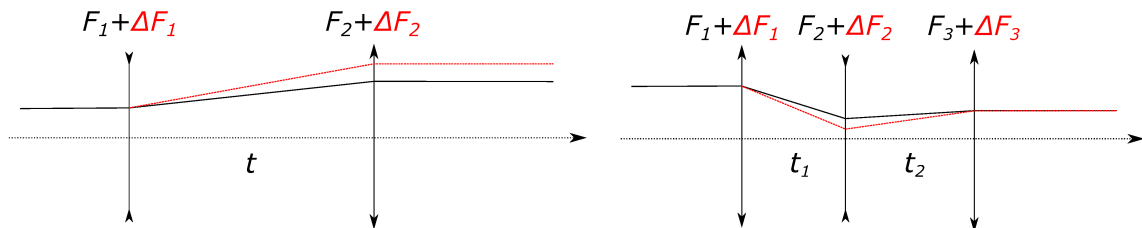


Figure 6.4.: Sketch of the afocal setups with two and three separated lenses. The layout with the black solid raypath shows the situation initially and the red dotted raypath shows the situation for a possible athermalized solution. With two separated lenses, only the focal power can be kept invariant with the laser power. A third lens additionally enables the compensation of the beam width.

6.4.1. Athermalization of a doublet

For two thin lenses close together, the resulting focal power is [38]

$$F = F_1 + F_2. \quad (6.25)$$

Additionally, the focal power of each lenses is split into the initial focal power F_i and the heat induced perturbation ΔF_i . Setting two lenses close together and keeping the focal power in the initial and in the heated state, results in

$$F = F_1 + F_2 = F_1 + \Delta F_1 + F_2 + \Delta F_2 \quad (6.26)$$

$$\Delta F_1 = -\Delta F_2 \quad (6.27)$$

For a small absorption and lenses close together, P and w are approximately equal in both lenses. Inserting Eq. 6.24 for the additional heat induced focal powers, results in the following relation

$$\xi_1 d_1 = -\xi_2 d_2. \quad (6.28)$$

To achieve a compensation, the sign of the parameters must differ, which can only be done with ξ . This is challenging, because there are only a few glasses with negative ξ according to Fig. 6.3. For an exact compensation, the left hand side of Eq. 6.28 must equal the right hand side, which might be an issue, since the material parameters are not continuous functions due to the limited glass choice. Fortunately, the thicknesses of both lenses are continuous functions. Therefore, the exact compensation is possible by a suitable glass choice and a subsequent fine tuning with the individual thicknesses of the lenses.

6.4.2. Athermalization with two separated lenses

With two separated lenses, it is not possible to control the beam width and the focal power simultaneously. The beam width at the second lens is determined by the focal power of the first lens and the distance between the lenses. Since the distance is fixed, but the focal power is changing due to heat, the waist size is variant with the laser power. However, the system can still be athermalized for the total focal power change $\Delta F = 0$. The consequences for a further focusing of the collimated beam are a constant focal position, but a change of the focal spot size due to the altered

numerical aperture.

The focal power of an afocal two lens system can be written as [38]

$$0 = F = F_1 + F_2 - tF_1F_2, \quad (6.29)$$

where t is the distance between both lenses. Similarly to the previous situation, there is an additional focal power for each lens generated by the introduced heat

$$0 = F = F_1 + \Delta F_1 + F_2 + \Delta F_2 - t(F_1 + \Delta F_1)(F_2 + \Delta F_2). \quad (6.30)$$

For an athermalized system, the difference between the focal power in the initial and the heated state must also equal zero, leading to the following condition

$$0 = \Delta F_1 + \Delta F_2 - t\Delta F_1F_2 - t\Delta F_2F_1 - t\Delta F_1\Delta F_2, \quad (6.31)$$

which can also be expressed as

$$\Delta F_1 = -\Delta F_2 \frac{1 - tF_1 - t\Delta F_1}{1 - tF_2}. \quad (6.32)$$

Inserting Eq. 6.24 for ΔF_2 yields

$$\Delta F_1 = -\frac{P\xi_2d_2}{2\pi(w_2 + \Delta w_2)^2} \frac{1 - tF_1 - t\Delta F_1}{1 - tF_2}. \quad (6.33)$$

With a paraxial raytrace, the beam width at the second lens is found

$$(w_2 + \Delta w_2)^2 = w_1^2(1 - t(F_1 + \Delta F_1))^2, \quad (6.34)$$

which leads to

$$\Delta F_1 = -\frac{P\xi_2d_2}{2\pi w_1^2(1 - t(F_1 + \Delta F_1))^2} \frac{1 - tF_1 - t\Delta F_1}{1 - tF_2}. \quad (6.35)$$

Inserting Eq. 6.24 for ΔF_1 and approximating the right hand side as power series dependent on P yields

$$P \frac{\xi_1 d_1}{2\pi w_1^2} \approx -P \frac{\xi_2 d_2}{2\pi w_1^2} - P^2 \frac{\xi_1 \xi_2 d_1 d_2}{4\pi^2 w_1^4} \frac{t(2 - m)}{m^2} + P^3 \frac{\xi_1^2 \xi_2 d_1^2 d_2}{8\pi^3 w_1^6} \frac{t^2(m^2 + 2m - 4)}{m^4}, \quad (6.36)$$

where $t = \frac{1}{F_1} + \frac{1}{F_2}$ is the distance between the lenses and $m = -\frac{F_1}{F_2}$ is the magnification of the telescope. From inspecting Eq. 6.36 it is seen that the athermalization in linear approximation equals the result for a doublet. Thus, Eq. 6.28 is a special case of Eq. 6.36. Additionally, it can be seen that individual expansion orders are vanishing for special values of m , e.g., the quadratic term is zero for $m = 2$. To suppress the higher order terms that are generated due the propagation, a small telescope length and a large magnification are beneficial. Unfortunately, this generates large ray angles at the lenses, leading to an increased system complexity and correspondingly to more lenses. If more than one lens is necessary for a lens group, each lens group can be athermalized individually by Eq. 6.28. Therefore, this leads to the conclusion that the the individual athermalization according to Eq. 6.28 is preferred, since this prevents the higher order terms and allows more relaxed designs, though at the costs of substituting each single lens by an appropriate doublet.

6.4.3. Athermalization with three separated lenses

In contrast to a two lens setup, a three lens system offers the possibility to simultaneously keep the system afocal and preserve the desired beam width at the final lens independent of the laser power. Therefore, the focus position and focus size are invariant with the applied laser power, if the collimated beam is further focused by appropriate system, e.g., an athermalized doublet.

A power invariant beam width and no change of the afocal condition corresponds to two conditions that must be fulfilled. The condition for the beam width can be found by a paraxial raytrace.

$$w_3 = w_1(1 - t_2(F_1 + F_2) + t_1F_1(t_2F_2 - 1)), \quad (6.37)$$

$$w_3 + \Delta w_3 = w_1(1 - t_2(F_1 + \Delta F_1 + F_2 + \Delta F_2) + t_1(F_1 + \Delta F_1)(t_2(F_2 + \Delta F_2) - 1)), \quad (6.38)$$

$$0 = \frac{\Delta w_3}{w_1} = -\Delta F_1 t_2 + \Delta F_2(-1 + F_1 t_1) t_2 + \Delta F_1 t_1(-1 + \Delta F_2 t_2 + F_2 t_2). \quad (6.39)$$

The last expression is, similar to the two-lens telescope, reformulated as

$$\Delta F_1 = \frac{-\Delta F_2(t_2 - F_1 t_1 t_2)}{t_1 + t_2 + \Delta F_2 t_1 t_2 - F_2 t_1 t_2}. \quad (6.40)$$

Inserting Eq. 6.24 for ΔF_1 and ΔF_2 with the perturbed beam width at the second lens according to Eq. 6.34, the right hand side is again written as a power series dependent on the laser power

$$P \frac{\xi_1 d_1}{2\pi w_1^2} \approx -P \frac{\xi_2 d_2}{2\pi w_1^2} \frac{t_2}{(-1 + F_1 t_1)(-t_2 + t_1(-1 + F_2 t_2))} - P^2 \frac{t_1 t_2 \xi_1 \xi_2 d_1 d_2 (2t_1(-1 + F_2 t_2) + t_2(-2\xi_1 d_1 + \xi_2 d_2))}{4\pi^2 w_1^4 (-1 + F_1 t_1)^3 (t_1 + t_2 - F_2 t_1 t_2)^2} \quad (6.41)$$

By satisfying Eq. 6.41, the beam width at the third lens is approximately invariant with the laser power.

In the next step the focal power is independently corrected by the last lens. The afocal power of a three lens system is [38]

$$0 = F = F_1 + F_2 + F_3 - t_1 F_1 (F_2 + F_3) - t_2 F_3 (F_1 + F_2) - t_1 t_2 F_1 F_2 F_3, \quad (6.42)$$

where t_1 and t_2 are the respective distances between the lenses. Including the heat induced perturbations into this, the same can be written for the heated system

$$0 = F = (F_1 + \Delta F_1) + (F_2 + \Delta F_2) + (F_3 + \Delta F_3) - t_1 (F_1 + \Delta F_1) (F_2 + \Delta F_2 + F_3 + \Delta F_3) - t_2 (F_3 + \Delta F_3) (F_1 + \Delta F_1 + F_2 + \Delta F_2) - t_1 t_2 (F_1 + \Delta F_1) (F_2 + \Delta F_2) (F_3 + \Delta F_3). \quad (6.43)$$

The difference between those two expression must also equal zero for a compensated focal power. As with the previous derivations, ΔF_1 is separated on the left hand side, such that

$$\Delta F_1 = - \frac{\Delta F_2 (-1 + F_1 t_1 + (\Delta F_3 + F_3)(1 + F_1 t_1) t_2)}{-1 + (\Delta F_2 + \Delta F_3 + F_2 + F_3) t_1 + (\Delta F_3 + F_3)(1 + (\Delta F_2 + F_2) t_1) t_2} - \frac{\Delta F_3 (-1 + F_2 t_2 + F_1 (t_1 + t_2 + F_2 t_1 t_2))}{-1 + (\Delta F_2 + \Delta F_3 + F_2 + F_3) t_1 + (\Delta F_3 + F_3)(1 + (\Delta F_2 + F_2) t_1) t_2}. \quad (6.44)$$

Now, Eq. 6.24 is inserted for ΔF_1 , ΔF_2 and ΔF_3 with the corresponding perturbed beam width at the second lens ($w_2 + \Delta w_2$). The beam width at the third lens is already considered and compensated by satisfying Eq. 6.41. Therefore, the beam width at the third lens is w_3 , purely. The expression on the right hand side is again

expanded into a power series of the laser power P .

$$P \frac{\xi_1 d_1}{2\pi w_1^2} \approx -P \left[g_2 \frac{\xi_2 d_2}{2\pi w_1^2} + g_3 \frac{\xi_3 d_3}{2\pi w_1^2} \right]. \quad (6.45)$$

The higher orders are omitted, since they are not considered further, similar to the two-lens telescope. The geometrical factors g_2 and g_3 are:

$$g_2 = \frac{(-1 + F_2 t_2 + F_1(t - F_2 t_1 t_2))^2 (1 - F_3 t_2 - F_1(t_1 + F_3 t_1 t_2))}{(1 - F_1 t_1)^2 (1 - F_2 t_2 - F_1(t - F_2 t_1 t_2))^2 (1 - F_3 t - F_2(t_1 + F_3 t_1 t_2))}, \quad (6.46)$$

$$g_3 = \frac{(1 - F_1 t_1)^2 (1 - F_2 t_2 - F_1(t + F_2 t_1 t_2))}{(1 - F_1 t_1)^2 (1 - F_2 t_2 - F_1(t - F_2 t_1 t_2))^2 (1 - F_3 t - F_2(t_1 + F_3 t_1 t_2))}, \quad (6.47)$$

with the total system length $t = t_1 + t_2$. Eq. 6.45 must be fulfilled to keep the three lens system approximately afocal independent from the laser power. Therefore, by simultaneously satisfying Eq. 6.41 and 6.45, the amplitude and phase of a fundamental Gaussian beam can be approximately maintained throughout the applied laser power. The same conclusion as for the two-lens telescope can be drawn here. To suppress the occurring higher order terms due to the propagation between the lenses, the distances must be kept short, while strong focal powers must be used. Again, this increases the system complexity and leads to large ray angles, which consequently require more lenses to control. Hence, the general consequence of section 6.4.1-6.4.3 is that the thermally induced effects should be compensated ideally where they occur. Only in this way, the higher order contributions can be reduced and an effective athermalization is achievable. This consequently means that each lens group should be athermalized individually.

6.5. Simulation of athermalized systems

In this section, the presented results to athermalize high power laser systems are tested via simulations in Zemax OpticStudio [91]. The modeling of the refractive index change with the laser power is done by the definition of 'Gradient 3', which describes the refractive index as $n(r) = n_{r0} + n_{r2}r^2 + n_{r4}r^4 + n_{r6}r^6$. Here, n_{r0} and n_{r2} can be calculated directly from the derived equations, whereas n_{r4} and n_{r6} are found by a least-square fit of the remaining distribution.

Two different setups are compared. The wavelength is in both cases $\lambda = 500$ nm

and the temperature at the boundary of the lenses is fixed at room temperature. At first, the behavior of a single lens is investigated for increasing laser power and compared to an athermalized doublet solution. The second setup consists of a two-lens telescope, which is also investigated for increasing laser power. Here, the athermalization is realized by two different approaches. The first approach utilizes Eq. 6.36 and thus changes the material of the second lens, whereas the second method is to split each lens into a doublet according to Eq. 6.28.

6.5.1. Comparison of a singlet and an athermalized doublet

The single lens is designed to focus a Gaussian beam with $w = 3$ mm at $f = 100$ mm with the glass 'N-BK7' at the initial state of $P = 0$ W. The thickness of the lens is fixed at $d = 5$ mm. The doublet is designed according to Eq. 6.28 and Fig. 6.3, while preserving the total thickness of the doublet. The material of the first lens is kept as 'N-BK7'. To keep the individual lens thicknesses approximately equal, 'N-LAK7' is found in Fig. 6.3 as an appropriate choice, since both material parameters are nearly of the same size, but with the necessary opposite sign for the compensation.

The results of this investigation are presented in Fig. 6.5. The initial spot radius is $4.5 \mu\text{m}$ for the single lens and $3.3 \mu\text{m}$ for the doublet. The slightly better performance is explained due to the additional surface and the larger refractive index of 'N-LAK7'. At 1 kW the spot radius of the single lens shows a minimum, while the spot radius of the doublet remains constant. This could be explained by a higher order effect of the GRIN material, such that spherical aberrations are corrected in this particular situation. At 10 kW the spot radius strongly increases with the laser power in case of the singlet. In contrast, the spot radius of the doublet remains constant until 10 kW and starts to increase slowly, afterwards. Therefore, the evaluation of the spot radius indicates the benefit of the athermal design. The amount of necessary refocus Δz for the smallest spot size shows an even more convincing behavior. Here, the doublet design performs better by a factor of 18. This corresponds to a required refocusing of $100 \mu\text{m}$ at 57 W in case of the singlet and at 1.02 kW for the doublet setup. The right column of Fig. 6.5 shows the layouts at 0 W, 0.1 MW and 1 MW to illustrate the thermally induced behavior. The observations for the spot radius and the defocus can be confirmed by the layouts, where the doublet design shows a significantly better performance. It must be noted that the observed

effects for extremely high laser power must be interpreted with caution, because the temperature variant material properties and technological challenges are not considered. However, if those points are proven to have a only minor impact, the presented theory works well and can help optical designers for the search of initial optical system for high power laser applications.

6.5.2. Comparison of athermalized two-lens telescopes

The telescope is designed to magnify an incoming Gaussian beam with $w_1 = 3$ mm by a factor of $m = 4$ with a Galilean setup, which enables a short total length and prevents an intermediate focus. The paraxial design is further determined by fixing the second focal length as $f_2 = 250$ mm. The material of both lenses for the initial design is again 'N-BK7' and the thicknesses of the lenses are $t_1 = 5$ mm and $t_2 = 12$ mm. The first athermal design based on Eq. 6.36 is made with same material combination as before. The negative lens is made out of 'N-BK7' and the positive lens is made out of 'N-LAK7' to achieve a compensation. Furthermore, t_1 is increased to 7 mm to account for a reasonable thickness of the positive lens. The second athermalized design is based on the individual compensation of each lens group, similar to the previous simulation, according to Eq. 6.28. Thus, each lens is substituted by an appropriate doublet, which again consist of the combination of 'N-BK7' and 'N-LAK7'. To better demonstrate the effects of a laser power dependent spot size and defocus and beam width after the positive lens w_2 , the magnified beam is focused by an ideal lens with $f = 100$ mm.

The results of the different designs are compared in Fig. 6.6. The initial spot radii are $0.35 \mu\text{m}$ for the pure 'N-BK7' design, $0.12 \mu\text{m}$ for mixed 'N-BK7' and 'N-LAK7' design and $0.14 \mu\text{m}$ for the doublet design. Thus, the two latter designs are comparable and perform by factor about two better than the pure 'N-BK7' design. Until 10 kW the spot sizes of the athermalized designs are nearly equal, showing the same minimum at 1 kW, while the the first design performs constantly worse and additionally shows a spot size increase at a lower laser power. Only for $P > 0.1$ MW, the doublet design outperforms the first athermal design. The plot of the necessary defocus Δz for a minimum spot size shows a similar behavior. Both athermalized designs perform better than the initial design. The first athermal design reduces the heat induced defocus by a factor of 5.7, while the doublet design performs slightly

better with a factor 6.7 up until 0.1 MW. At 1 MW the spot size and the defocus increase drastically for the first athermal design, such that it is now comparable to the initial design, while the doublet design shows a continuous performance decrease with increasing laser power. To understand the higher order effects due to the propagation distance between the lens group according to Eq. 6.36, the beam width based on the waist ray at the second lens is also plotted. Here, the strongest difference between both athermalized designs is observed. While the doublet design shows a nearly uniform beam width over the entire laser power range, the singlet design behaves similar to the initial design. This is understandable, since the higher orders are not corrected in both cases. It is even noticeable, that the beam width of the initial design behaves slightly better than the athermalized singlet design, which can be understood by the corresponding lens thicknesses. The first lens thickness of the initial design is shorter than the athermalized doublet design, which leads to less absorption in the material and correspondingly to a reduced heat induced focal power. The beam width at 1 MW shows a negative sign, which indicates an intermediate focus. This effect can also be observed in Fig. 6.7, where the corresponding layouts are shown at 0 W, 0.1 MW and 1 MW. Visually, it can be confirmed that both athermal designs improve the performance regarding spot size and defocus, especially at moderate laser powers. At very high laser powers, the higher order effects due to the distance between the lenses becomes dominant, such that the athermal singlet design performs nearly as the initial design. Therefore, to maximally maintain the beam performance, the higher order terms must be suppressed, which is only possible with the doublet approach as predicted by theory in section 6.4.

The simulation of a three-lens telescope is not shown in this work due to the page limit. However, similar results as for two-lens considerations can be expected, since the theory is based on the same assumptions. Moreover, induced effects of spherical aberration are even more critical in this scenario, which leads to the same conclusion, that each lens group should be individually athermalized to maintain the desired performance.

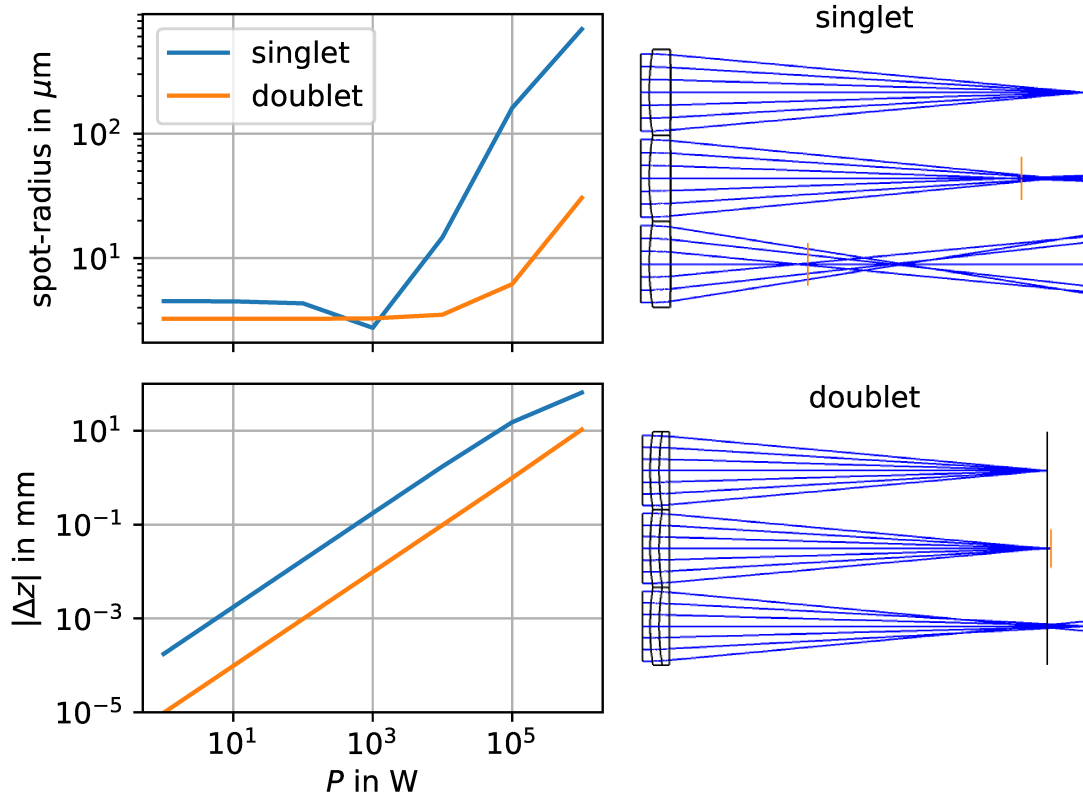


Figure 6.5.: Performance comparison of a singlet made of 'N-BK7' with a focal length of $f = 100$ mm with a compensated doublet according to Eq. 6.28 with 'N-BK7' and 'N-LAK7'. Shown are the spot radius based on ray tracing in the optimal focus position and the absolute value of the focus shift Δz dependent on the laser power in the left column. The right column pictures the focus behavior of the corresponding singlet and the compensated doublet with increasing laser power at 0 W, 0.1 MW and 1 MW. Here, the black vertical line shows the optimal focus position of the cold lens and the orange line indicates the focus position after accounting for the heat impact. Note that a uniform ray sampling is chosen for the layout plot, but the computations are based on Gaussian sampling.

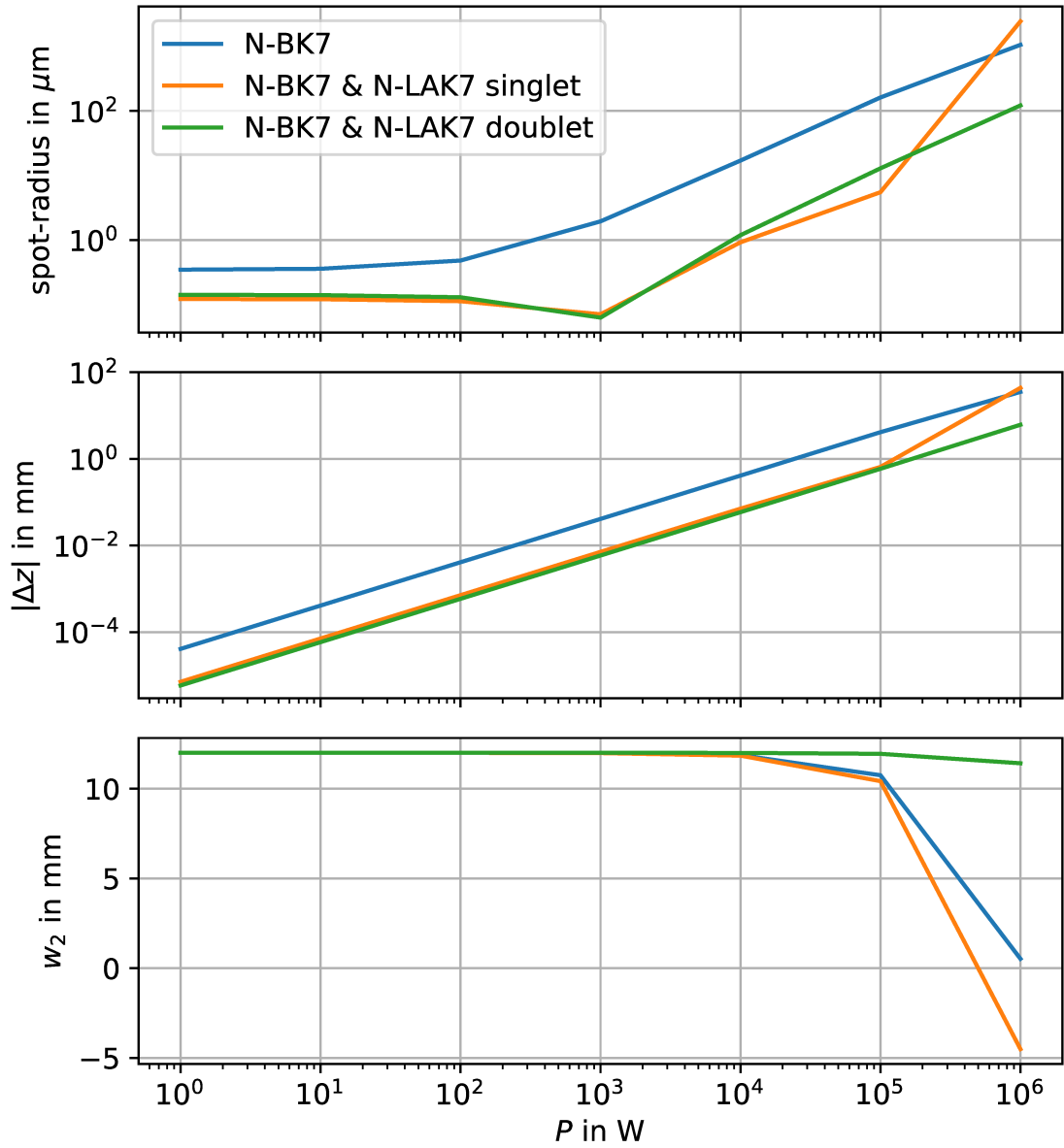


Figure 6.6.: Performance comparison of two-lens telescopes with a magnification of $m = 4$ and a focal length of the second lens of $f_2 = 250$ mm. The magnified beam is focused by an ideal lens with $f = 100$ mm. The initial non-athermalized setup consists of two lenses with the glass 'N-BK7', whereas the second setup is athermalized according to Eq. 6.36 with 'N-BK7' for the negative lens and 'N-LAK7' for the positive lens. The third setup corresponds to a solution, where each lens group is replaced by an appropriate doublet made out of 'N-BK7' and 'N-LAK7'. The corresponding layouts are plotted in Fig. 6.7.

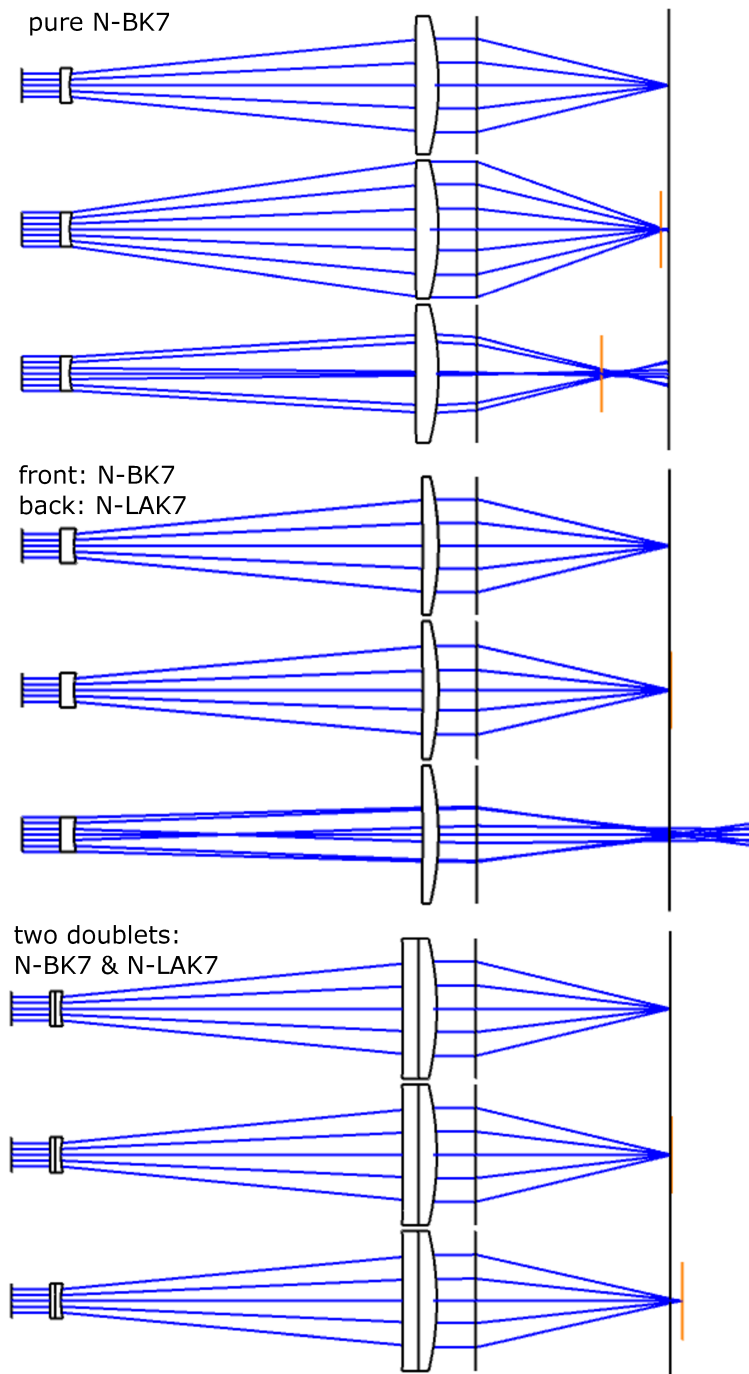


Figure 6.7.: Layout of the simulated two-lens telescopes with a magnification of $m = 4$ and a focal length of the second lens of $f_2 = 250$ mm. The collimated beam is focused by an ideal lens with $f = 100$ mm at 0 W, 0.1 MW and 1 MW. The first group shows the layout for the initial singlet design with 'N-BK7' only. The second group shows the layout for a athermalized combination of 'N-BK7' and 'N-LAK7' according to Eq. 6.36 and the third group is the layout for the design with two athermalized doublets, each consisting of 'N-BK7' and 'N-LAK7', according to Eq. 6.28. Note that a uniform ray sampling is chosen for the layout plot, but the computations are based on Gaussian sampling.

7. Conclusion and outlook

In this thesis, novel methods to simulate the beam shaping of high power laser beams with the special consideration of Bessel beams were introduced and discussed. These methods were successfully evaluated and allow a deeper insight into the performance of such systems, while enabling new possibilities for the design, simulation and analysis. The major results of this work are briefly summarized below. In chapter 4, real laser beams were reconstructed in amplitude and phase by a new laser beam specific approach to solve the transport of intensity equation. This allows to identify the properties of the laser beams in a more comprehensive way than it is possible with the standard M^2 measurement. Additionally, the reconstructed field can be integrated as the real light source in complex simulations of laser systems. Based on artificial data, an error metric was developed which allows to estimate the remaining phase errors in order to make further wavefront measurement obsolete. A novel calculation scheme for the fast evaluation of the on-axis field of perturbed Bessel-Gauss beams is presented in chapter 5. For this purpose, the Fresnel diffraction integral was solved analytically for a Gaussian apodization and a conical wavefront of the initial field. Wavefront errors were considered based on the stationary phase approximations and series expansions. Within this approach, the wavefront errors were described by an arbitrary order of spherical aberration and primary astigmatism and coma, which allows the description of typical wavefront aberrations of beam shaping optics due to misalignment and manufacturing errors. The presented scheme was further used for the sensitivity analysis of an example system. To evaluate the performance of the the generated on-axis line focus effectively, an extended definition of the Strehl-ratio along the optical axis was introduced, which is dependent on z . In chapter 6, the athermalization of refractive high power laser systems was realized by an appropriate combination of materials. This was done in several steps. In the first step, the temperature distribution inside a thin lens was derived based on the heat source that is modelled by the bulk absorption of a high power fundamental Gaussian laser beam. The resulting non-uniform change of the refractive index and the

corresponding GRIN-properties of the heated medium were considered in the second step to formulate the additional heat induced focal power of a single lens. In the third step, an important material property of additional focal power was elaborated to categorize different glasses according to their thermal response. This is done to further support the optical designer in the preselection of possible glasses. In the final step, the found expression was utilized to athermalize basic optical systems like a doublet and two- and three-lens telescopes. The major result of this investigation is, that each lens group of a high power system must be athermalized individually to prevent higher order terms, that enhance during propagation. Therefore, each lens group should at least consist of an athermalized doublet. In summary, several contributions for an improved modelling, simulation and design of high power laser systems were made in this work.

Inspired by the results of this work, there are certain promising points which can be addressed within future research and development. A possible extension of the laser beam specific phase retrieval approach to partial coherent light sources and pulsed light sources would be of great interest for many applications. For the characterization of the line focus of quasi-Bessel beams, the presented scheme could be utilized to estimate the wavefront aberrations based on the measured intensity along the focus, similar to standard inverse techniques. This would greatly enhance the possibilities to characterize and evaluate real quasi-Bessel beams, since this is still challenging today. The derived theory for the athermalization of high power laser systems would profit from a comprehensive market analysis of available glasses and possible glass combinations. This should be done at typical wavelengths of high power laser systems to deliver a practical tool for the simple athermalization estimation of such systems. Furthermore, the results should be tested against full simulations based on finite-element-methods to explore the limitations of the initially paraxial considerations with fixed boundary constraints.

Bibliography

- [1] C. Phipps, G. Albrecht, H. Friedman, D. Gavel, E. George, J. Murray, C. Ho, W. Priedhorsky, M. Michaelis, and J. Reilly, “Orion: Clearing near-earth space debris using a 20-kw, 530-nm, earth-based, repetitively pulsed laser,” *Laser and Particle Beams*, vol. 14, no. 1, pp. 1–44, 1996.
- [2] S. A. Ahmed, M. Mohsin, and S. M. Z. Ali, “Survey and technological analysis of laser and its defense applications,” *Defence Technology*, 2020.
- [3] W. R. Leeb, “Laser space communications systems, technologies, and applications,” *The Review of Laser Engineering*, vol. 28, no. 12, pp. 804–808, 2000.
- [4] M. Jenne, D. Flamm, T. Ouaj, J. Hellstern, J. Kleiner, D. Grossmann, M. Koschig, M. Kaiser, M. Kumkar, and S. Nolte, “High-quality tailored-edge cleaving using aberration-corrected bessel-like beams,” *Optics Letters*, vol. 43, no. 13, pp. 3164–3167, 2018.
- [5] R. Klas, S. Demmler, M. Tschernajew, S. Hädrich, Y. Shamir, A. Tünnermann, J. Rothhardt, and J. Limpert, “Table-top milliwatt-class extreme ultraviolet high harmonic light source,” *Optica*, vol. 3, no. 11, pp. 1167–1170, 2016.
- [6] G. Mourou, B. Brocklesby, T. Tajima, and J. Limpert, “The future is fibre accelerators,” *Nature Photonics*, vol. 7, no. 4, pp. 258–261, 2013.
- [7] E. Hilpert, J. Hartung, S. Risse, R. Eberhardt, and A. Tünnermann, “Precision manufacturing of a lightweight mirror body made by selective laser melting,” *Precision Engineering*, vol. 53, pp. 310–317, 2018.
- [8] E. Hilpert, J. Hartung, H. von Lukowicz, T. Herffurth, and N. Heidler, “Design, additive manufacturing, processing, and characterization of metal mirror made of aluminum silicon alloy for space applications,” *Optical Engineering*, vol. 58,

no. 9, p. 092613, 2019.

- [9] A. Siegman, *Lasers*. University Science Books, 1986.
- [10] N. Hodgson and H. Weber, *Laser Resonators and Beam Propagation: Fundamentals, Advanced Concepts, Applications*. Springer Berlin Heidelberg, 2005.
- [11] R. Kammel, R. Ackermann, J. Thomas, J. Götte, S. Skupin, A. Tünnermann, and S. Nolte, “Enhancing precision in fs-laser material processing by simultaneous spatial and temporal focusing,” *Light: Science & Applications*, vol. 3, no. 5, pp. e169–e169, 2014.
- [12] M. Kumkar, M. Kaiser, J. Kleiner, D. Grossmann, D. Flamm, K. Bergner, and S. Nolte, “Ultrafast laser processing of transparent materials supported by in-situ diagnostics,” in *Laser Applications in Microelectronic and Optoelectronic Manufacturing (LAMOM) XXI*, vol. 9735, p. 97350P, International Society for Optics and Photonics.
- [13] A. Ancona, F. Röser, K. Rademaker, J. Limpert, S. Nolte, and A. Tünnermann, “High speed laser drilling of metals using a high repetition rate, high average power ultrafast fiber cpa system,” *Optics express*, vol. 16, no. 12, pp. 8958–8968, 2008.
- [14] T. S. Ross, *Laser beam quality metrics*. Society of Photo-Optical Instrumentation Engineers, 2013.
- [15] S. Schmidt, S. Thiele, A. Toulouse, C. Bösel, T. Tiess, A. Herkommer, H. Gross, and H. Giessen, “Tailored micro-optical freeform holograms for integrated complex beam shaping,” *Optica*, vol. 7, no. 10, pp. 1279–1286, 2020.
- [16] J. Durnin, “Exact solutions for nondiffracting beams. i. the scalar theory,” *Journal of the Optical Society of America A*, vol. 4, no. 4, pp. 651–654, 1987.
- [17] J. Durnin, J. J. Miceli, and J. H. Eberly, “Diffraction-free beams,” *Physical Review Letters*, vol. 58, no. 15, pp. 1499–1501, 1987.
- [18] P. Milonni and J. Eberly, *Laser Physics*. Wiley, 2010.
- [19] M. Duocastella and C. B. Arnold, “Bessel and annular beams for materials processing,” *Laser & Photonics Reviews*, vol. 6, no. 5, pp. 607–621, 2012.

- [20] Z. Ding, H. Ren, Y. Zhao, J. S. Nelson, and Z. Chen, “High-resolution optical coherence tomography over a large depth range with an axicon lens,” *Optics Letters*, vol. 27, no. 4, pp. 243–245, 2002.
- [21] K. Doyle, V. Genberg, G. Michels, and S. o. P.-o. I. Engineers, *Integrated Optomechanical Analysis*. SPIE Press, 2012.
- [22] P. Yoder, *Opto-Mechanical Systems Design*. CRC Press, 2005.
- [23] E. Wyss, M. Roth, T. Graf, and H. P. Weber, “Thermo-optical compensation methods for high-power lasers,” *IEEE Journal of Quantum Electronics*, vol. 38, no. 12, pp. 1620–1628, 2002.
- [24] T. Jamieson, “Thermal effects in optical systems,” *Optical Engineering*, vol. 20, no. 2, p. 202156, 1981.
- [25] G. Chuan-Bo, C. Chang-Shui, S. Qiu-Ming, and Z. Ling, “Resonator insensitive investigation to thermal lens for end-pumped lasers,” *Chinese Physics*, vol. 13, no. 8, pp. 1263–1268, 2004.
- [26] J. Hartung, H. von Lukowicz, and J. Kinast, “Theoretical compensation of static deformations of freeform multimirror substrates,” *Applied Optics*, vol. 57, no. 15, pp. 4020–4031, 2018.
- [27] J. Hartung, S. Merx, and H. v. Lukowicz, “Compensation for general asymmetric static loads for a complete optical system of freeform mirrors,” *Applied Optics*, vol. 59, no. 6, pp. 1507–1518, 2020.
- [28] W. Singer, M. Totzeck, and H. Gross, *Handbook of Optical Systems, Volume 2: Physical Image Formation*. Wiley, 2006.
- [29] B. Saleh and M. Teich, *Fundamentals of Photonics*. Wiley, 2007.
- [30] M. Born, E. Wolf, and A. Bhatia, *Principles of Optics: Electromagnetic Theory of Propagation, Interference and Diffraction of Light*. Cambridge University Press, 2000.
- [31] J. Stamnes, *Waves in Focal Regions: Propagation, Diffraction and Focusing of Light, Sound and Water Waves*. Taylor & Francis, 1986.

- [32] J. Goodman, *Introduction to Fourier Optics*. W. H. Freeman, 2005.
- [33] A. Walther, C. U. Press, P. Knight, W. A. and A. Miller, *The Ray and Wave Theory of Lenses*. Cambridge University Press, 1995.
- [34] M. R. Teague, “Deterministic phase retrieval: a green’s function solution,” *Journal of the Optical Society of America*, vol. 73, no. 11, pp. 1434–1441, 1983.
- [35] L. Waller, L. Tian, and G. Barbastathis, “Transport of intensity phase-amplitude imaging with higher order intensity derivatives,” *Optics Express*, vol. 18, no. 12, pp. 12552–12561, 2010.
- [36] T. E. Gureyev, A. Roberts, and K. A. Nugent, “Phase retrieval with the transport-of-intensity equation: matrix solution with use of zernike polynomials,” *Journal of the Optical Society of America A*, vol. 12, no. 9, pp. 1932–1941, 1995.
- [37] T. E. Gureyev and K. A. Nugent, “Phase retrieval with the transport-of-intensity equation. ii. orthogonal series solution for nonuniform illumination,” *Journal of the Optical Society of America A*, vol. 13, no. 8, pp. 1670–1682, 1996.
- [38] H. Gross, *Handbook of Optical Systems, Volume 1: Fundamentals of Technical Optics*. Wiley, 2005.
- [39] D. Malacara, *Optical Shop Testing*. Wiley, 2007.
- [40] A. Broemel, U. Lippmann, and H. Gross, “Freeform surface descriptions. part i: Mathematical representations,” *Advanced Optical Technologies*, vol. 6, no. 5, pp. 327–336, 2017.
- [41] D. D. Lowenthal, “Maréchal intensity criteria modified for gaussian beams,” *Applied Optics*, vol. 13, no. 9, pp. 2126–2133, 1974.
- [42] V. N. Mahajan, “Strehl ratio for primary aberrations: some analytical results for circular and annular pupils,” *Journal of the Optical Society of America*, vol. 72, no. 9, pp. 1258–1266, 1982.
- [43] V. N. Mahajan, “Strehl ratio for primary aberrations in terms of their aberration variance,” *Journal of the Optical Society of America*, vol. 73, no. 6, pp. 860–861, 1983.

- [44] V. N. Mahajan, “Strehl ratio of a gaussian beam,” *Journal of the Optical Society of America A*, vol. 22, no. 9, pp. 1824–1833, 2005.
- [45] K. Strehl, *Theorie des Fernrohrs: Auf Grund der Beugung des Lichts*. J.A. Barth (A. Meiner), 1894.
- [46] S. Pan, J. Ma, R. Zhu, T. Ba, C. Zuo, F. Chen, J. Dou, C. Wei, and W. Zhou, “Real-time complex amplitude reconstruction method for beam quality m2 factor measurement,” *Optics Express*, vol. 25, no. 17, pp. 20142–20155, 2017.
- [47] A. T. Friberg, “Stationary-phase analysis of generalized axicons,” *Journal of the Optical Society of America A*, vol. 13, no. 4, pp. 743–750, 1996.
- [48] T. Čižmár and K. Dholakia, “Tunable bessel light modes: engineering the axial propagation,” *Optics Express*, vol. 17, no. 18, pp. 15558–15570, 2009.
- [49] H. Gross, H. Zügge, M. Peschka, and F. Blechinger, *Handbook of Optical Systems, Aberration Theory and Correction of Optical Systems*. Wiley, 2007.
- [50] M. Tessmer and H. Gross, “Generalized propagation of light through optical systems. i. mathematical basics,” *JOSA A*, vol. 32, no. 2, pp. 258–266, 2015.
- [51] M. Tessmer and H. Gross, “Generalized propagation of light through optical systems. ii. numerical implications,” *JOSA A*, vol. 32, no. 12, pp. 2276–2285, 2015.
- [52] A. v. Pfeil, F. Wyrowski, A. Drauschke, and H. Aagedal, “Analysis of optical elements with the local plane-interface approximation,” *Applied Optics*, vol. 39, no. 19, pp. 3304–3313, 2000.
- [53] B. Dörband, H. Gross, and H. Müller, *Handbook of Optical Systems, Volume 5: Metrology of Optical Components and Systems*. Wiley, 2012.
- [54] J. C. Wyant and K. Creath, “Basic wavefront aberration theory for optical metrology,” 1992.
- [55] W. Gao and T. Milster, “Strehl ratio for optical systems with ultrafast illumination,” *Optics Express*, vol. 26, no. 14, pp. 18028–18042, 2018.
- [56] G. Nemes and A. Siegman, “Measurement of all ten second-order moments

- of an astigmatic beam by the use of rotating simple astigmatic (anamorphic) optics,” *JOSA A*, vol. 11, no. 8, pp. 2257–2264, 1994.
- [57] A. E. Siegman, “Analysis of laser beam quality degradation caused by quartic phase aberrations,” *Applied Optics*, vol. 32, no. 30, pp. 5893–5901, 1993.
- [58] J. H. McLeod, “The axicon: A new type of optical element,” *Journal of the Optical Society of America*, vol. 44, no. 8, pp. 592–597, 1954.
- [59] A. Jeffrey and D. Zwillinger, *Table of Integrals, Series, and Products*. Elsevier Science, 2007.
- [60] M. Honkanen and J. Turunen, “Tandem systems for efficient generation of uniform-axial-intensity bessel fields,” *Optics Communications*, vol. 154, no. 5, pp. 368–375, 1998.
- [61] J. Cao, X. Cheng, J. Shang, and Y. He, “Structural design and thermal analysis of the vehicle lidar system,” *Optical Engineering*, vol. 59, no. 8, p. 084105, 2020.
- [62] M. Rubio and J. Regan, “Optimizing eye-safe micro-pulse lidar (laser-radar) performance through optical design and thermal stabilization,” in *1999 IEEE LEOS Annual Meeting Conference Proceedings. LEOS’99. 12th Annual Meeting. IEEE Lasers and Electro-Optics Society 1999 Annual Meeting (Cat. No. 99CH37009)*, vol. 1, pp. 253–254, IEEE.
- [63] C. Niclass, D. Inoue, H. Matsubara, T. Ichikawa, and M. Soga, “Development of automotive lidar,” *Electronics and Communications in Japan*, vol. 98, no. 5, pp. 28–33, 2015.
- [64] W. Smith, *Modern Optical Engineering, 4th Ed.* McGraw-Hill Education, 2007.
- [65] J. R. Fienup, “Phase retrieval algorithms: a comparison,” *Applied Optics*, vol. 21, no. 15, pp. 2758–2769, 1982.
- [66] J. R. Fienup, “Phase retrieval algorithms: a personal tour [invited],” *Applied Optics*, vol. 52, no. 1, pp. 45–56, 2013.
- [67] B. Boehme and H. Gross, “Characterization of complex optical systems based on wavefront retrieval from point spread function,” in *Optical Systems Design 2005*, vol. 5965, SPIE.

- [68] P. Dirksen, J. Braat, A. Janssen, and C. Juffermans, “Aberration retrieval using the extended nijboer-zernike approach,” *Journal of Micro/Nanolithography, MEMS, and MOEMS*, vol. 2, no. 1, 2003.
- [69] Y. Zhu, Z. Zhang, and G. Barbastathis, “Phase imaging for absorptive phase objects using hybrid uniform and structured illumination transport of intensity equation,” *Optics Express*, vol. 22, no. 23, pp. 28966–28976, 2014.
- [70] P. Soltani, A.-R. Moradi, A. Darudi, and R. Shomali, *High resolution optical surface testing using transport of intensity equation*, vol. 8785. 2013.
- [71] J. Stock, A. Broemel, J. Hartung, D. Ochse, and H. Gross, “Description and reimplementaion of real freeform surfaces,” *Applied Optics*, vol. 56, no. 3, pp. 391–396, 2017.
- [72] S. Merx, J. Stock, F. R. Widiyasari, and H. Gross, “Beam characterization by phase retrieval solving the transport-of-intensity-equation,” *Optics Express*, vol. 28, no. 14, pp. 20898–20907, 2020.
- [73] J. Hu and L. Wu, “Hybrid method for accurate phase retrieval based on higher order transport of intensity equation and multiplane iteration,” *Optical Engineering*, vol. 58, no. 6, pp. 1–9, 9, 2019.
- [74] E. Reinhard, G. Ward, S. Pattanaik, and P. Debevec, *High Dynamic Range Imaging: Acquisition, Display, and Image-Based Lighting*. Elsevier Science, 2005.
- [75] P. E. Debevec and J. Malik, *Recovering high dynamic range radiance maps from photographs*. Proceedings of the 24th annual conference on Computer graphics and interactive techniques, ACM Press/Addison-Wesley Publishing Co., 1997.
- [76] D. Paganin, A. Barty, P. J. McMahon, and K. A. Nugent, “Quantitative phase-amplitude microscopy. iii. the effects of noise,” *Journal of Microscopy*, vol. 214, no. 1, pp. 51–61, 2004.
- [77] C. Zuo, Q. Chen, Y. Yu, and A. Asundi, “Transport-of-intensity phase imaging using savitzky-golay differentiation filter - theory and applications,” *Optics Express*, vol. 21, no. 5, pp. 5346–5362, 2013.

- [78] A. Savitzky and M. J. E. Golay, “Smoothing and differentiation of data by simplified least squares procedures,” *Analytical Chemistry*, vol. 36, no. 8, pp. 1627–1639, 1964.
- [79] P. J. Marchand, D. Szlag, J. Extermann, A. Bouwens, D. Nguyen, M. Rudin, and T. Lasser, “Imaging of cortical structures and microvasculature using extended-focus optical coherence tomography at 1.3 μm ,” *Optics Letters*, vol. 43, no. 8, pp. 1782–1785, 2018.
- [80] V. Garcés-Chávez, D. McGloin, H. Melville, W. Sibbett, and K. Dholakia, “Simultaneous micromanipulation in multiple planes using a self-reconstructing light beam,” *Nature*, vol. 419, no. 6903, pp. 145–147, 2002.
- [81] W. G. Rees, “The validity of the fresnel approximation,” *European Journal of Physics*, vol. 8, no. 1, pp. 44–48, 1987.
- [82] W. H. Southwell, “Validity of the fresnel approximation in the near field,” *Journal of the Optical Society of America*, vol. 71, no. 1, pp. 7–14, 1981.
- [83] S. Merx, J. Stock, and H. Gross, “Fast computation and characterization of perturbed bessel–gauss beams,” *Journal of the Optical Society of America A*, vol. 36, no. 11, pp. 1892–1897, 2019.
- [84] J. Stock, N. G. Worku, and H. Gross, “Coherent field propagation between tilted planes,” *Journal of the Optical Society of America A*, vol. 34, no. 10, pp. 1849–1855, 2017.
- [85] B. Zhu, S. Li, Y. Mao, X. Wang, Y. Bu, J. Wang, G. Sun, and L. Duan, “Fast thermal aberration model for lithographic projection lenses,” *Optics Express*, vol. 27, no. 23, pp. 34038–34049, 2019.
- [86] J. Werschnik and K. Uhlendorf, *Method for quick thermal tolerancing of optical systems*, vol. 9951 of *SPIE Optical Engineering + Applications*. SPIE, 2016.
- [87] F. Lakhdari, I. Osmani, and S. Tabet, *Heat generation and thermo-mechanical effect modeling in longitudinally diode-pumped solid state lasers*, vol. 9626 of *SPIE Optical Systems Design*. SPIE, 2015.
- [88] A. Stein, “Thermooptically perturbed resonators,” *IEEE Journal of Quantum*

- Electronics*, vol. 10, no. 4, pp. 427–434, 1974.
- [89] M. Lesniewski, *Simulation of the parameters for an optical system with coaxial radial thermal gradient*, vol. 3745 of *International Conference on Optical Metrology*. SPIE, 1999.
- [90] M. J. Moritz, “Radial distribution of temperature in a thin lens due to absorption of light and heat conduction,” *Optik*, vol. 122, no. 12, pp. 1050–1057, 2011.
- [91] L. Zemax Europe, *OpticStudio 18.7 User Manual*. Zemax LLC, 2018.
- [92] A. Schott, *Optical Glass Collection Datasheets*. Schott AG, 2019.
- [93] J. P. Gordon, R. C. C. Leite, R. S. Moore, S. P. S. Porto, and J. R. Whinnery, “Long-transient effects in lasers with inserted liquid samples,” *Journal of Applied Physics*, vol. 36, no. 1, pp. 3–8, 1965.
- [94] J. Wesfreid, A. Burgos, H. Mancini, and E. Quel, “Calculation of the focal length of a thermal lens inside a laser cavity,” *Optics Communications*, vol. 21, no. 3, pp. 413–418, 1977.

A. Appendix

A.1. Explicit formulation of Zernike-polynomials

j	Z_j in Cartesian formulation	Name
1	1	Piston
2	x	Tilt x
3	y	Tilt y
4	$2(x^2 + y^2) - 1$	Defocus
5	$2xy$	1 st Astigmatism 0°
6	$y^2 - x^2$	1 st Astigmatism 45°
7	$x(3x^2 + 3y^2 - 2)$	1 st Coma x
8	$y(3y^2 + 3x^2 - 2)$	1 st Coma y
9	$6(x^2 + y^2)^2 - 6(x^2 + y^2) + 1$	1 st Spherical
10	$x(3y^2 - x^2)$	Trefoil 0°
11	$y(y^2 - 3x^2)$	Trefoil 30°
12	$2xy(4x^2 + 4y^2 - 3)$	2 nd Astigmatism 0°
13	$(y^2 - x^2)(4x^2 + 4y^2 - 3)$	2 nd Astigmatism 45°
14	$x[10(x^2 + y^2)^2 - 12(x^2 + y^2) + 3]$	2 nd Coma x
15	$y[10(x^2 + y^2)^2 - 12(x^2 + y^2) + 3]$	2 nd Coma y
16	$20(x^2 + y^2)^3 - 30(x^2 + y^2)^2 + 12(x^2 + y^2) - 1$	2 nd Spherical
25	$70(x^2 + y^2)^4 - 140(x^2 + y^2)^3 + 90(x^2 + y^2)^2 - 20(x^2 + y^2) + 1$	3 rd Spherical
36	$256(x^2 + y^2)^5 - 630(x^2 + y^2)^4 + 560(x^2 + y^2)^3 - 210(x^2 + y^2)^2 + 30(x^2 + y^2) - 1$	4 th Spherical

Table A.1.: First orders of the Cartesian representation and classification of Zernike-polynomials in Fringe convention.

A.2. Thermal properties of glasses

glass name	n	$\frac{\partial n}{\partial T}$ $\times 10^6$	κ	α_{abs}	x_g $\times 10^6$	x_f $\times 10^6$	ξ $\times 10^9$
F2	1.6299	3.2989	0.780	0.120	9.200	3.963	0.508
F2HT	1.6299	3.2989	0.780	0.120	9.200	3.963	0.508
F5	1.6126	3.5055	0.880	0.241	8.900	3.178	0.959
FK5HTi	1.4914	-2.4076	0.925	0.241	10.000	14.899	-0.627
K10	1.5065	2.9301	1.120	0.362	7.400	1.615	0.946
K7	1.5160	0.3378	nan	0.281	9.700	9.045	nan
LAFN7	1.7619	7.1550	0.770	0.241	6.400	-2.990	2.237
LASF35	2.0425	4.4908	0.920	5.387	8.500	4.192	26.296
LF5	1.5897	0.9375	0.866	0.160	10.600	9.010	0.174
LF5HTi	1.5897	0.9320	0.866	0.080	10.600	9.020	0.086
LLF1	1.5551	1.6697	0.990	0.160	9.200	6.192	0.270
LLF1HTi	1.5551	1.6648	0.990	0.082	9.200	6.201	0.138
N-BAF10	1.6782	3.6189	0.780	0.767	7.040	1.704	3.560
N-BAF4	1.6137	2.0685	1.020	0.605	8.290	4.919	1.226
N-BAF51	1.6606	1.6859	0.670	0.605	9.490	6.938	1.521
N-BAF52	1.6162	2.0282	0.960	0.808	7.830	4.538	1.707
N-BAK1	1.5782	1.2312	0.795	0.321	8.600	6.471	0.498
N-BAK2	1.5452	0.3874	0.920	0.241	9.000	8.289	0.101
N-BAK4	1.5747	2.6348	0.880	0.241	7.930	3.345	0.721
N-BAK4HT	1.5747	2.6348	0.880	0.201	7.930	3.345	0.600
N-BALF4	1.5858	3.8409	0.850	0.281	7.410	0.853	1.270
N-BALF5	1.5533	1.6482	1.050	0.321	8.430	5.451	0.504
N-BASF2	1.6752	3.2898	0.940	1.177	8.130	3.258	4.120
N-BASF64	1.7144	3.1577	nan	2.475	8.700	4.280	nan
N-BK10	1.5021	2.0625	1.320	0.362	6.600	2.492	0.565
N-BK7	1.5214	1.6517	1.114	0.241	8.300	5.132	0.357
N-BK7HT	1.5214	1.6517	1.114	0.120	8.300	5.132	0.178
N-BK7HTi	1.5214	1.6517	1.114	0.120	8.300	5.132	0.178
N-F2	1.6299	2.3341	1.050	0.645	9.060	5.355	1.434
N-FK5	1.4914	-2.3334	0.925	0.442	10.000	14.748	-1.116
N-FK51A	1.4899	-6.8179	0.760	0.160	14.810	28.728	-1.438

glass name	n	$\frac{\partial n}{\partial T}$ $\times 10^6$	κ	α_{abs}	x_g $\times 10^6$	x_f $\times 10^6$	ξ $\times 10^9$
N-FK58	1.4589	-7.3206	0.760	0.241	15.720	31.673	-2.319
N-K5	1.5275	0.8286	0.950	0.281	9.600	8.029	0.245
N-KF9	1.5293	0.5893	1.040	0.241	10.950	9.837	0.136
N-KZFS11	1.6464	3.3171	0.810	0.442	7.560	2.429	1.812
N-KZFS2	1.5643	3.9706	0.810	0.321	5.400	-1.636	1.575
N-KZFS4	1.6213	2.4064	0.840	0.523	8.200	4.327	1.499
N-KZFS4HT	1.6213	2.4064	0.840	0.483	8.200	4.327	1.383
N-KZFS5	1.6637	4.2692	0.950	0.605	7.390	0.957	2.717
N-KZFS8	1.7325	2.8592	1.050	0.605	9.430	5.527	1.646
N-LAF2	1.7536	-0.2665	0.670	0.686	9.100	9.454	-0.273
N-LAF21	1.7976	3.6646	0.830	0.442	7.080	2.485	1.953
N-LAF33	1.7961	7.2028	0.800	0.483	6.700	-2.347	4.348
N-LAF34	1.7815	4.0244	0.800	0.281	7.000	1.850	1.414
N-LAF35	1.7520	7.0389	0.800	0.321	6.380	-2.981	2.827
N-LAF7	1.7620	3.0906	0.830	2.903	8.390	4.334	10.809
N-LAK10	1.7282	3.7606	0.860	0.483	6.830	1.666	2.112
N-LAK12	1.6850	-1.8139	0.680	0.564	9.300	11.948	-1.504
N-LAK14	1.7040	2.5416	0.890	0.321	6.900	3.290	0.918
N-LAK21	1.6466	-0.4013	0.880	0.483	8.100	8.721	-0.220
N-LAK22	1.6578	1.7087	0.750	0.483	7.400	4.803	1.100
N-LAK33B	1.7633	3.0929	0.890	0.281	7.060	3.008	0.976
N-LAK34	1.7369	2.4100	0.820	0.241	6.910	3.639	0.707
N-LAK7	1.6580	-0.6966	0.740	0.321	8.200	9.259	-0.302
N-LAK8	1.7206	3.5330	0.840	0.241	6.700	1.797	1.012
N-LAK9	1.6983	2.3202	0.908	0.321	7.500	4.177	0.821
N-LASF31A	1.8955	3.6088	0.790	0.890	7.720	3.690	4.065
N-LASF40	1.8470	8.0797	0.810	1.260	6.900	-2.639	12.565
N-LASF41	1.8462	4.0693	0.790	0.645	7.330	2.521	3.323
N-LASF43	1.8176	5.1714	0.810	1.013	6.660	0.335	6.466
N-LASF44	1.8142	3.8962	0.820	0.442	7.390	2.605	2.102
N-LASF45	1.8144	4.5695	1.020	1.716	8.560	2.949	7.689
N-LASF45HT	1.8144	4.5695	1.020	1.467	8.560	2.949	6.570
N-LASF46A	1.9204	5.8379	0.910	2.052	7.150	0.808	13.162

glass name	n	$\frac{\partial n}{\partial T}$ $\times 10^6$	κ	α_{abs}	x_g $\times 10^6$	x_f $\times 10^6$	ξ $\times 10^9$
N-LASF46B	1.9204	7.7607	0.880	2.305	7.110	-1.321	20.329
N-LASF9	1.8656	4.0193	0.790	2.263	8.380	3.737	11.513
N-LASF9HT	1.8656	4.0193	0.790	2.263	8.380	3.737	11.513
N-PK51	1.5325	-7.9230	0.650	0.281	14.120	28.999	-3.425
N-PK52A	1.5005	-7.5343	0.730	0.160	15.000	30.054	-1.655
N-PSK3	1.5573	1.6666	0.990	0.402	7.300	4.310	0.677
N-PSK53A	1.6236	-3.7194	0.640	0.321	10.840	16.804	-1.867
N-SF1	1.7315	0.8344	1.000	1.301	10.540	9.399	1.085
N-SF10	1.7432	0.4867	0.960	2.263	10.800	10.145	1.147
N-SF11	1.8026	1.4598	0.950	1.926	9.850	8.031	2.959
N-SF14	1.7786	0.1922	1.000	1.467	10.870	10.623	0.282
N-SF15	1.7124	2.4203	1.040	1.218	9.280	5.883	2.835
N-SF2	1.6588	3.9252	1.140	1.013	7.810	1.852	3.487
N-SF4	1.7712	0.4780	0.950	2.136	10.870	10.250	1.075
N-SF5	1.6848	2.3431	1.000	0.972	9.210	5.789	2.277
N-SF57	1.8675	1.3689	0.990	2.903	9.880	8.302	4.014
N-SF57HT	1.8675	1.3689	0.990	2.817	9.880	8.302	3.895
N-SF57HTultra	1.8675	1.3689	0.990	2.178	9.880	8.302	3.012
N-SF6	1.8237	0.6385	0.960	2.348	10.340	9.565	1.561
N-SF66	1.9487	1.6329	0.800	7.453	6.830	5.109	15.212
N-SF6HT	1.8237	0.6385	0.960	2.052	10.340	9.565	1.365
N-SF6HTultra	1.8237	0.6385	0.960	1.633	10.340	9.565	1.086
N-SF8	1.7017	1.5856	1.030	1.508	9.920	7.660	2.322
N-SK11	1.5692	1.8429	nan	0.241	7.600	4.362	nan
N-SK14	1.6088	1.7477	0.851	0.281	7.300	4.429	0.577
N-SK16	1.6263	0.9235	0.818	0.362	7.300	5.825	0.408
N-SK2	1.6136	3.2309	0.776	0.402	7.100	1.834	1.674
N-SK2HT	1.6136	3.2309	0.776	0.201	7.100	1.834	0.835
N-SK4	1.6187	1.3995	0.830	0.321	7.380	5.118	0.542
N-SK5	1.5947	2.3823	0.990	0.241	6.500	2.494	0.579
N-SSK2	1.6290	3.9014	0.810	0.321	6.650	0.448	1.547
N-SSK5	1.6659	1.9003	nan	0.727	8.000	5.146	nan
N-SSK8	1.6249	1.6335	0.840	0.645	8.160	5.546	1.255

glass name	n	$\frac{\partial n}{\partial T}$ $\times 10^6$	κ	α_{abs}	x_g $\times 10^6$	x_f $\times 10^6$	ξ $\times 10^9$
N-ZK7	1.5132	5.7460	1.042	0.281	5.200	-5.996	1.549
N-ZK7A	1.5128	5.5236	1.042	0.281	5.230	-5.541	1.490
P-BK7	1.5210	3.4945	1.130	0.160	7.320	0.613	0.496
P-LAF37	1.7651	6.3058	0.900	0.362	7.800	-0.442	2.534
P-LAK35	1.7010	0.3973	0.720	0.321	9.680	9.113	0.177
P-LASF47	1.8175	7.3590	0.850	0.483	7.270	-1.732	4.181
P-LASF50	1.8202	7.6338	0.950	0.523	7.320	-1.988	4.206
P-LASF51	1.8215	7.4102	0.870	0.523	7.400	-1.621	4.458
P-SF68	2.0333	25.0938	0.650	9.938	9.670	-14.616	383.682
P-SF69	1.7369	1.6825	1.120	0.686	11.130	8.847	1.030
P-SF8	1.7018	0.4760	1.020	1.136	11.100	10.422	0.530
P-SK57	1.5927	2.3369	1.010	0.201	8.900	4.957	0.464
P-SK57Q1	1.5917	nan	1.010	0.201	8.900	nan	nan
P-SK58A	1.5947	2.5028	1.020	0.281	8.410	4.201	0.689
P-SK60	1.6164	2.3091	1.130	0.120	8.850	5.104	0.246
SF1	1.7315	7.1457	0.660	0.281	8.800	-0.968	3.042
SF10	1.7432	7.3315	0.741	0.442	8.400	-1.465	4.378
SF11	1.8025	12.3302	0.737	0.972	6.800	-8.565	16.257
SF2	1.6588	3.6139	0.735	0.281	9.200	3.715	1.382
SF4	1.7712	8.5616	0.650	0.362	8.900	-2.202	4.763
SF5	1.6848	4.8647	0.690	0.281	9.000	1.897	1.981
SF56A	1.8023	9.4777	0.690	0.442	8.800	-3.014	6.077
SF57	1.8674	12.3442	0.620	0.564	9.200	-5.031	11.228
SF57HTultra	1.8674	12.3442	0.620	0.402	9.200	-5.031	8.004
SF6	1.8237	10.6196	0.673	0.362	9.000	-3.893	5.706
SF6HT	1.8237	10.6196	0.673	0.345	9.000	-3.893	5.452

Table A.2.: Thermal properties of Schott glasses at 20 °C and $\lambda = 500$ nm according to the data sheets [92]. The units of the parameters are as follows: $[\frac{\partial n}{\partial T}] = \text{°C}^{-1}$, $[\kappa] = \text{W m}^{-1} \text{°C}^{-1}$, $[\alpha_{abs}] = \text{m}^{-1}$, $[x_g] = \text{°C}^{-1}$, $[x_f] = \text{°C}^{-1}$ and $[\xi] = \text{W}^{-1}$.

A.3. Thermal properties of mounting materials

metal	$x_m \times 10^6 \text{ in } ^\circ\text{C}^{-1}$
aluminum	23.6-24
beryllium	12
invar	0.9-1.0
steel	14.7
magnesium	26.0

Table A.3.: Thermal properties of selected metals used as mounting material according to [22, 24, 38].

B. Ehrenwörtliche Erklärung

Ich erkläre hiermit ehrenwörtlich, dass ich die vorliegende Arbeit selbständig, ohne unzulässige Hilfe Dritter und ohne Benutzung anderer als der angegebenen Hilfsmittel und Literatur angefertigt habe. Die aus anderen Quellen direkt oder indirekt übernommenen Daten und Konzepte sind unter Angabe der Quelle gekennzeichnet.

Bei der Auswahl und Auswertung folgenden Materials haben mir die nachstehend aufgeführten Personen in der jeweils beschriebenen Weise unentgeltlich geholfen:

- Prof. Dr. Herbert Gross hat das Promotionsvorhaben betreut. Er war an der Auswahl der Themen dieser Arbeit beteiligt und sowohl die Ergebnisse als auch die vorliegende Dissertation wurden mit ihm diskutiert.
- Der Ansatz und experimentelle Aufbau zur Rekonstruktion der Phase wurden zusammen mit Johannes Stock (IAP, Jena), wie in Kapitel 4 beschrieben, realisiert. Geeignete Parameter wurden gemeinsam mit Fransiska Widiyarsari im Rahmen einer Masterarbeit evaluiert.
- Im Übrigen waren jeweils die Koautoren der aus dieser Arbeit entstandenen Veröffentlichungen, siehe Publikationsliste, an der Interpretation und Diskussion der Ergebnisse beteiligt.

Weitere Personen waren an der inhaltlich-materiellen Erstellung der vorliegenden Arbeit nicht beteiligt. Insbesondere habe ich hierfür nicht die entgeltliche Hilfe von Vermittlungs- bzw. Beratungsdiensten (Promotionsberater oder andere Personen) in Anspruch genommen. Niemand hat von mir unmittelbar oder mittelbar geldwerte Leistungen für die Arbeiten erhalten, die im Zusammenhang mit dem Inhalt der vorgelegten Dissertation stehen.

Die Arbeit wurde bisher weder im In- noch im Ausland in gleicher oder ähnlicher

Form einer anderen Prüfungsbehörde vorgelegt.

Die geltende Promotionsordnung der Physikalisch-Astronomischen Fakultät ist mir bekannt.

Ich versichere ehrenwörtlich, dass ich nach bestem Wissen die reine Wahrheit gesagt und nichts verschwiegen habe.

Jena, den

Sebastian Merx

C. Liste der wissenschaftlichen Veröffentlichungen und Vorträge

Artikel in Fachzeitschriften (peer-reviewed)

1. A. Brahm, M. Tymoshchuk, F. Wichmann, S. Merx, G. Notni, and A. Tünnermann, "Wavelet based identification of substances in terahertz tomography measurements", *Journal of Infrared, Millimeter, and Terahertz Waves* 35, 974-986 (2014)
2. J. Stock, M. Beier, J. Hartung, S. Merx, and H. Gross, "Simulation and analysis of optical imaging systems including real freeform components", *Advanced Optical Technologies* 8, 111 (2019)
3. S. Merx, J. Stock, and H. Gross, "Fast computation and characterization of perturbed Bessel–Gauss beams", *J. Opt. Soc. Am. A* 36, 1892-1897 (2019)
4. J. Hartung, S. Merx, and H. v. Lukowicz, "Compensation for general asymmetric static loads for a complete optical system of freeform mirrors", *Appl. Opt.* 59, 1507-1518 (2020)
5. S. Merx, J. Stock, F. R. Widiyasari, and H. Gross, "Beam characterization by phase retrieval solving the transport-of-intensity-equation", *Opt. Express* 28, 20898-20907 (2020)

Konferenzbeiträge und Vorträge

1. J. Stock, M. Beier, J. Hartung, S. Merx und H. Gross, „Optical simulation of an imaging telescope including manufactured freeform surfaces” in EOSAM Delft 2018: Design, Tolerancing and Fabrication, (European Optical Society, 2018)
2. S. Merx, J. Stock und H. Gross, „Sensitivity analysis of Bessel-beams generated by axicons” in EOSAM Delft 2018: Design, Tolerancing and Fabrication, (European Optical Society, 2018)

D. Danksagung

Im Folgenden möchte ich den Personen danken, die mich stets unterstützt haben und damit einen direkten oder indirekten Beitrag für meine Arbeit geleistet haben.

Als erstes möchte ich mich bei meinem Mentor Prof. Dr. Herbert Gross bedanken. Danke, dass du mich auf diesem Weg begleitet, und an den richtigen Stellen die Wegweiser aufgestellt hast. Ich habe bei dir sehr viel gelernt. Einen Teil des fachlichen Aspekts kann man in den letzten 120 Seiten begutachten, jedoch ist der für mich viel entscheidendere Aspekt der menschliche – und den kann man nirgends lesen. Für dein offenes Ohr und deine Geduld auch in kriselnden Situationen bin ich dir sehr dankbar. Wie du uns gezeigt hast, wie die Dinge so laufen und dass letztendlich alle nur mit Wasser kochen, wenn sie denn überhaupt kochen. Auch dafür danke ich dir sehr.

An zweiter Stelle möchte ich den Kolleginnen und Kollegen aus unserer Gruppe danken. Gerade die Anfangszeit habe ich sehr genossen. Ich würde gerne einmal hochrechnen, wieviel Kuchen wir in dieser Zeit gegessen haben und was das an Hüftgold für jeden ausmacht, oder lieber nicht. Auch an die glorreichen Erfolge bei den Institutsweihnachtsfeiern erinnere ich mich gerne.

Ein großes Dankeschön geht auch an die Mittagsgruppe. Euch vermisse ich schon sehr in letzter Zeit. Gurkenwasser, das Wundermittel für guten Geschmack, aber auch die Frage nach adäquater Kleidung bei der Verteidigung sind neben Modellen zur Hohlerde wirklich Dinge, die mich zutiefst in meiner persönlichen Entwicklung geprägt haben. Danke an Ralf, Sören, Christoph, Tobi, Johannes & Johannes, Enrico, Sebastian und Matze. Die Zeit zum Abschalten war immer sehr schön.

Einen besonderen Dank gilt es meinem ehemaligen Nachbarn im Büro und zuhause auszusprechen. Johannes, wir haben sehr viel zusammen geschafft, erlebt und uns dementsprechend auch weiterentwickelt. Über unseren Austausch von Kulturgütern,

insbesondere der vielfältigen Dialektformen, bin ich noch immer froh. Ich denke, auch du kannst hier mittlerweile ein Brötchen bestellen und ich einen Zwiebelrostbraten in deiner Region. Unsere offenen und ehrlichen Diskussionen habe ich immer genossen. Das letzte Jahr ohne dich im Büro war nicht gerade das schönste, jedoch hat mich der exzessive Kaffeegenuss aus deiner alten Domobar stets wieder mit schönen Erinnerungen erheitert. Danke auch dafür, dass du dir stets Zeit genommen hast, auch wenn du eigentlich keine Zeit hattest.

Meinen Jungs von den Trippers möchte ich auch meinen Dank aussprechen. Unsere gemeinsamen Zeiten mit dem Genuss von Hopfenkaltschale und Brat-/Grill- oder Rostgut sind immer eine schöne Abwechslung gewesen und ich hoffe, dass wir das noch lange beibehalten.

Für den Rückhalt in meiner Familie möchte ich mich sehr bedanken. Besonders mein Vater hat großen Anteil an meinem Weg. Papa, du hast mich großgezogen, deine Werte und Einstellungen haben mich teils bewusst, aber auch teils unterbewusst geprägt und mich zu dem gemacht, der ich jetzt bin. Besonders in schwierigen Zeiten habe ich gemerkt, wie wichtig du für mich bist. Für deine grenzenlose Unterstützung bei all meinem Handeln kann ich dir gar nicht genug danken.

Am Ende dieser Arbeit möchte ich meinem Stepherle danken. Danke einfach für alles, was du für mich tust!